UNIVERSITY OF CALIFORNIA, SAN DIEGO

Ultracold Plasmas and Guiding Center Drift Atoms

A dissertation submitted in partial satisfaction of the

requirements for the degree Doctor of Philosophy

in Physics

by

Stanislav Gennadyevich Kuzmin

Committee in charge:

Professor Thomas O'Neil, Chairman
Professor Daniel Dubin
Professor Julius Kuti
Professor Kevin Quest
Professor Sergei Krasheninnikov

2004

The dissertation of Stanislav Gennadyevich Kuzmin is approved, and it is acceptable in quality and form for publication on microfilm:

Chairman

University of California, San Diego

2004

Table of Contents

List of Figures

Acknowledgements

I would like to thank my advisor Professor Tom O'Neil. He taught me a lot about physics and the ways to do research. I was always impressed by how a complicated physics problem can be explained in a simple way and reduced in complexity, using basic principles and ideas of physics. For me as a foreign graduate student, his judgement and advice about life in the United States and at UCSD was always very valuable, and helped me a lot during my studies at UCSD.

I also thank Professor Fred Driscoll; he helped me a lot with setting up and managing large scale computer simulations, and with his stimulating questions that made me express "theory statements" in a way that experimentalists can understand. I have appreciated discussions with Professor Daniel Dubin and Dr. Francois Anderegg on the results of my research. Jo Ann Christina was very helpful in the preparation of technical manuscripts and arranging trips to conferences. Of course, I am grateful to all members of the non-neutral plasma group at UCSD.

I am very grateful to Professor Julius Kuti, who suggested the Aarseth multiple time-step algorithm that was extensively used in my research. He also taught a very helpful course on computational methods in physics. In addition, I want to thank Professor Sverre Aarseth for discussing with me the implementation of the algorithm.

Much of the work contained in this thesis is an attempt to provide a theoretical understanding of phenomena observed in experiments on ultracold plasmas and the creation of antihydrogen. I wish to thank Professor Thomas Killian, Dr. Lars Jørgensen, Dr. Niels Madsen, and Professor Gerald Gabrielse for helpful discussions and giving me insight into the experiments.

I wish to thank Professor Dmitri Ryutov for recommending me to my advisor Tom O'Neil during the summer of 1999.

My former advisor at the Novosibirsk State University, Professor Igor Kotelnikov, taught me basic plasma physics and supervised my first research projects. He gave me a lot of knowledge about plasma physics theory which helped me tremendously in my research at UCSD. He also recommended me to Professor Dmitri Ryutov which helped me to continue my studies in plasma physics at UCSD.

Vladimir Shelest, my teacher at school No. 130 in Novosibirsk, was the one who stimulated my interest in physics. I am grateful to him for showing what science really is. It was due to him that I chose this path which led me this far. I will never forget those summer and winter schools for scholars and the first research problems that I tried to solve there.

Finally, I would like to express my deepest gratefulness to my family. Without their warm and understanding support my studies in physics would not be possible.

Chapter 2 of this thesis has been published in Physics of Plasmas: "Numerical Simulation of Ultracold Plasmas", S.G. Kuzmin, T.M. O'Neil, **9**, 3743-3751 (2002). Chapter 3 has been published in Physics of Plasmas: "Guiding Center Drift Atoms", S.G. Kuzmin, T.M. O'Neil, M.E. Glinsky, **11**, 2382-2393 (2004). Chapter 4 has been submitted to Physics of Plasmas: "Motion of Guiding Center Drift Atoms in the Electric and Magnetic Field of a Penning Trap", S.G. Kuzmin,

T.M. O'Neil. S.G. Kuzmin was the primary investigator and author of these papers.

This research was supported by the National Science Foundation, (PHY-9876999) and the Office of Naval Research (N00014-96-1-0239).

Vita, Publications and Fields of Study

Vita

1 February 1976	Born, Novosibirsk, Russia
1997	B.S., Novosibirsk State University, Novosibirsk, Russia
1999	M.S., Novosibirsk State University, Novosibirsk, Russia
1999-2004	Research Assistant, University of California, San Diego
2004	Ph.D., University of California, San Diego

Publications

1. Stanislav Kuzmin, “Spinning in a Jet Stream (Bernoulli, Magnus, and a Vacuum Cleaner)”, Quantum **5**, 49-52 Sep/Oct (1994) [Translated from Russian, Kvant No. 3/4, 53-55 (1993)]
2. I.A. Kotelnikov, S.G. Kuzmin, “RF Plugging of Mirror Plasma”, Journal of Fusion Energy **15**, 173-181 (1996)
3. V.I. Volosov, I.A. Kotelnikov, S.G. Kuzmin, “Separation of Heavy-Element Isotopes by Selective ICR Heating Techniques”, Plasma Physics Reports **24**, 474-485 (1998) [Translated from Russian, Fizika Plazmy **24**, 517-529 (1998)]
4. I.A. Kotelnikov, S.G. Kuzmin, “Separation of Heavy-Element Isotopes by ICR Heating at the Second Harmonics” Plasma Physics Reports **25**, 1010-1019 (1999) [Translated from Russian, Fizika Plazmy **25**, 1095-1104 (1999)]
5. S.G. Kuzmin, “Effect of Longitudinal Structure of the Antenna Field on the Production Rate of an ICR Isotope Separator” Plasma Physics Reports **25**, 1020-1025 (1999) [Translated from Russian, Fizika Plazmy **25**, 1105-1111 (1999)]
6. V.I. Volosov, I.A. Kotelnikov, I.N. Churkin, S.G. Kuzmin, S.G. Steshov, A.V. Timofeev, “Device for Plasma Separation Process”, Atomnaya Energia (Atomic Energy) **88**, 370-378 (2000) [in Russian]
7. S.G. Kuzmin, T.M. O’Neil, “Numerical Simulation of Ultracold Plasmas: How Rapid Intrinsic Heating Limits the Development of Correlation”, Phys. Rev. Lett. **88**, 065003 (2002)
8. S.G. Kuzmin, T.M. O’Neil, “Numerical Simulation of Ultracold Plasmas”, Physics of Plasmas **9**, 3743-3751 (2002)
9. S.G. Kuzmin, T.M. O’Neil, M.E. Glinsky, “Guiding Center Drift Atoms”, Physics of Plasmas **11**, 2382-2393 (2004)
10. S.G. Kuzmin, T.M. O’Neil, “Polarization and Trapping of Weakly Bound Atoms in Penning Trap Fields”, Phys. Rev. Lett. **92**, 243401 (2004)
11. S.G. Kuzmin, T.M. O’Neil, “Motion of Guiding Center Drift Atoms in the Electric and Magnetic Field of a Penning Trap”, Physics of Plasmas, in submission, (2004)

Fields of Study

Major Field: Physics

Studies in Plasma Physics.
Professors from Novosibirsk State University:
Andrey Arzhannikov, Alexey Beklemishev, Yurii Belchenko,
Vladimir Davydenko, Alexander Ivanov, Andrey Kabantsev,
Boris Knyazev, Vasilii Koidan, Igor Kotelnikov, Konstantin Lotov

Studies in Electromagnetism.
Professor Aneesh Manohar

Studies in Quantum Mechanics.
Professor Lu Sham

Studies in Statistical Mechanics.
Professors Daniel Arovas,
Viktor Belinicher (Novosibirsk State University)

Studies in Stellar Structures and Evolution.
Professor Arthur Wolfe

Studies in Mathematical Physics.
Professor Aneesh Manohar

Studies in Nonlinear and Nonequilibrium Dynamics of Physical Systems.
Professor Patrick Diamond

Abstract of the Dissertation

Ultracold Plasmas and Guiding Center Drift Atoms

by

Stanislav Gennadyevich Kuzmin
Doctor of Philosophy in Physics
University of California, San Diego, 2004
Professor Thomas O'Neil, Chairman

This thesis discusses theory questions suggested by recent experiments with ultracold plasmas. In one class of experiments, ultracold plasmas are produced by abruptly photoionizing small clouds of laser cooled atoms, adjusting the photon energy to barely exceed the ionization energy of the cooled atoms. The thesis presents molecular dynamics simulation for the early time evolution of such plasmas. Contrary to earlier speculation, no evidence of strong electron-electron correlations is observed in the simulations even if the initial value of the coupling parameter ($\Gamma_e = e^2/akT_e$) is much larger than unity. As electron-electron correlations begin to develop, the correlation energy is released to heat the electrons, raising the electron temperature to the point where $\Gamma_e \sim 1$ and limiting further development of correlation. Further heating of the electrons occurs as a by-product of three-body recombination. When a model of laser cooling is added to the simulation, the formation of strong ion-ion correlation is observed. Contrary to earlier suggestion, the rate of three-body recombination is observed to be in reasonable agreement with the traditional formula, $R = 3.9{\times}10^{-9}\,\mathrm{sec}^{-1}[n\ (\mathrm{cm}^{-3})]^2\ [T_e(^\circ K)]^{-9/2}$, but care must be taken to use the correct temporally evolving temperature, T_e.

Also, the thesis describes the novel dynamics of “guiding center drift atoms”. The weakly bound and strongly magnetized antihydrogen atoms recently produced in ultracold plasmas at CERN are examples of such atoms. The atoms are quasi-classical, and the dynamics of the positron is well described by guiding center drift theory. Because of a frequency ordering, the dynamics is integrable, and the thesis characterizes the possible motions of the weakly bound positron-antiproton pair as a function of constants of the motion. Quantum numbers are assigned using the Bohr-Sommerfeld prescription. The thesis also discusses the center of mass motion of the atoms in an electric and magnetic field. The effective electric field in the moving frame of the atom polarizes the atom, and the gradients in the field give rise to a force on the atom. An approximate equation of motion for the atom center of mass is obtained by averaging over the rapid internal dynamics of the atom. Experimentally relevant applications of the equation of motion are discussed. Finally, the critical field for ionization is determined as an upper bound on the range of applicability of the theory.

Chapter 1

General introduction

1.1 Unmagnetized Ultracold Neutral Plasmas

Shortlived, neutral, ultracold plasmas have been produced in recent experiments, and these novel plasmas suggest interesting theory questions. This thesis addresses some of these questions.

In a first class of experiments, neutral ultracold plasmas were produced by abruptly photoionizing a laser cooled cloud of atoms. The frequency of the ionizing radiation was carefully adjusted so that the photon energy barely exceeded the ionization potential of the atoms [1, 2, 3, 4]. In closely related experiments, the photon energy was just below the ionization potential, so a gas of high-n Rydberg atoms was produced [5], and a plasma resulted from a collisional ionization cascade [6, 7, 8]. My co-authors an I focused on questions suggested by the first set of experiments where the plasma state is produced directly. From the perspective of a plasma physicist, these experiments have the advantage of a well defined initial plasma state.

In an early publication [1], the experimental team suggested that the ultralow initial temperature implies a state of strong interparticle correlation, but we doubted this claim. Our reason is easy to understand physically. For a plasma in thermal equilibrium, the strength of correlation is determined by the coupling parameter $\Gamma = e^2/akT$, where a is the Wigner-Seitz radius (i.e., $4\pi a^3 n/3 = 1$) [9]. For the maximum density and lowest electron and ion temperatures reported in the experiments [i.e., $n \simeq 2 \times 10^9$ cm^{-3}, $T_e \simeq 0.1$ K, and $T_i = 10$ μK], the electron coupling parameter has the value $\Gamma_e \simeq 30$, and the ion coupling parameter is much larger. Thus, one might expect the low temperatures to lead to strong correlation.

However, the plasma is not created in a state of thermal equilibrium. Before photoionization, the neutral atoms are uncorrelated, so immediately after photoionization ion-ion and electron-electron correlations are negligible. There may be some electron-ion correlation that remains as an artifact of the ionization process, but this is not a thermal equilibrium correlation. For example, there is no long range order. The temperatures reported are measures of particle kinetic energy, but do not imply the degree of correlation that would exist for a true thermal equilibrium.

Thermal equilibrium correlations can develop only through the action of Coulomb interactions as the plasma evolves. However, as the correlations begin to develop, the correlation energy is released to the electron plasma as heat, and this limits the strength of correlation reached. To reach a correlation strength corresponding to $\Gamma_e \simeq 1$, each electron picks up thermal energy $kT_e \simeq e^2/a$. At this point the coupling parameter has the value

$$\Gamma_e = e^2/akT_e \simeq (e^2/a)/(e^2/a) = 1,$$

so further development of correlation ceases. Even if the initial electron temperature were zero, corresponding formally to infinite Γ_e, strong correlation would not develop.

Another way to understand the electron heating is to note that electrons are born in a spatially varying potential, and immediately begin to move downhill. A typical electron picks up kinetic energy e^2/a while moving an interparticle spacing, a. The time scale for this initial heating is approximately $a/\sqrt{e^2/am_e} \sim \omega_{pe}^{-1}$, where ω_{pe} is the electron plasma frequency. Similarly, release of ion-ion correlation energy heats the the ions and limits the development of ion-ion correlation. The time scale for the ion heating is ω_{pi}^{-1}, where ω_{pi} is the ion plasma frequency.

The electron heating is the beginning of the collisional process by which the plasma approaches a state of thermal equilibrium. For the low temperatures of these plasmas the thermal equilibrium state is a recombined neutral gas. The collisional cascade of electrons to deeper and deeper binding in the Coulomb wells of ions is called three-body recombination [10]. In this process, the recombination energy is carried off by a second electron (rather than a photon) and enters the plasma as heat. For these plasmas, three-body recombination is very rapid–much faster than radiative recombination.

In a classic paper, Mansbach and Keck [10] argued that three-body recombination proceeds at the rate $R = 3.9 \cdot 10^{-9}\,\mathrm{s}^{-1}[n(\mathrm{cm}^{-3})]^2[T_e(\mathrm{K})]^{-9/2}$, which is very large at low temperatures. However it was suggested that the Mansbach and Keck formula would not apply at the low temperatures of these plasmas [1]. Indeed, the formula does fail for $\Gamma_e = e^2/(akT_e) > 1$, but we argue that rapid electron heating raises T_e to the point where $\Gamma_e \sim 1$, and the formula applies at least approximately.

These ideas were corroborated by molecular dynamics simulations of the plasma early time evolution. The simulations were challenging because it was necessary to follow the recombination into weakly bound (high-n) Rydberg states, and the time-scale for an electron in such a state is much shorter than that for a typical electron. For the three-body process, the initial recombination is into states where the binding energy is of order kT_e. Since kT_e is orders of magnitude less than the Rydberg energy, even after the rapid heating from release of the correlation energy, a simulation based on classical dynamics is adequate.

In plasma simulations of this kind some authors have used two time scales: one for particles with near neighbors and another for the remaining particles [11]. Another variant is to use piecewise analytic solutions for Kepler orbits. We prefer a treatment that doesn't make special assumptions about particles with near neighbors, but seamlessly encompasses the continuum of time scales required.

Fortunately, such a treatment was developed previously in computational studies of binary star formation in globular clusters. The binary stars are the analogue of the high-n Rydberg atoms, and the cluster is the analogue of the plasma cloud. Following a suggestion from Professor Julius Kuti, we have adapted a code developed originally by Aarseth [12] for the study of binary star formation.

The code is a molecular dynamics simulation in the sense that the force on a given particle from each of the other particles is calculated directly. Time integration is effected with a predictor-corrector scheme using a fourth-order polynomial fit to the orbit. The crucial feature is that the time step for each particle is adjusted independently depending on such factors as the rate of change of the acceleration. Thus, a bound electron can have a much shorter time step than a typical electron without slowing down the whole simulation. To keep all of the particles moving in near synchrony, the code advances next the time step for the particle that is furthest behind in absolute time. To evaluate the force on this particle, the other particle positions are extrapolated back in time to exact synchrony using the polynomial fit to the orbits.

As one would expect, there are interesting parallels between the dynamics of these plasmas and the dynamics of globular clusters. Indeed, the heating that occurs as a byproduct of three-body recombination is similar to the heating of clusters that accompanies the “hardening” of binary stars. Through collisional interactions the binary stars become more deeply bound, and the liberated gravitational energy enters the cluster as heat. This heating mechanism is thought to be crucial in the support of clusters against gravothermal contraction and core collapse [13].

Our simulation exhibited the expected rapid heating, with Γ_e dropping to order unity on a time scale of one electron plasma period. We examined the electron-electron correlation function $G(|\vec{r}_1 - \vec{r}_2|, t)$ at various times t in the simulation. Here, $|\vec{r}_1 - \vec{r}_2|$ is the electron-electron separation. Initially, the correlation function was uniformly zero [i.e., $G(|\vec{r}_1 - \vec{r}_2|, t = 0) = 0$] corresponding to randomly distributed electrons. After a few electron plasma periods, the correlation function fell to -1 for small separation but remained zero for larger separation. The -1 value reflects the fact that it is energetically unfavorable for two electrons to be near one another. The observed functional form for the correlation function confirms the the absence of long range order, and is consistent with correlation strength $\Gamma_e \simeq 1$. Long range order is manifested by the appearance of spatial oscillations in $G(|\vec{r}_1 - \vec{r}_2|)$ for larger $|\vec{r}_1 - \vec{r}_2|$, indicating the presence of a local lattice. No such oscillations were observed.

The ion-ion correlation function evolved on the time scale of few ion plasma periods. Again the correlation function started out flat and then relaxed to the same form as the electron-electron correlation function. The absence of oscillations in the correlation function indicates no long-range order and the value of correlation parameter $\Gamma_i \sim 1$.

After the initial rapid heating due to the release of correlation energy, the electrons continued to heat but at much slower rate. This long-term slower heating is associated with three-body recombination. As pairs recombine, they release binding energy and heat free electrons. Contrary to earlier suggestion, we found that the rate of three-body recombination is in reasonable agreement with the traditional formula. Since the initial release of correlation energy reduces the value of Γ_e to unity or less, the traditional formula applies at least approximately. We found that the rate observed in the simulations is two to three times smaller than the rate predicted by traditional formula. Since the rate strongly depends on temperature (proportional to $T_e^{-9/2}$), care must be taken to use the correct temporally evolving temperature T_e.

An unexpected by-product of three-body recombination was the production of suprathermal electrons that were ejected from the plasma. A close collision of a free thermal electron with a tightly bound pair often results in a more deeply bound pair and a free electron with kinetic energy of order the binding energy of the pair. This can be much larger than the thermal energy. Likewise, in globular clusters binaries "harden" by giving kinetic energy to other stars through collisional interactions, sometimes ejecting stars at high velocity from the core of the cluster [14].

Killian noted that both Strontium (Sr) atoms and Sr^+ ions can be laser cooled and suggested that a strongly correlated ion plasma might be achieved by laser cooling the ions shortly after the plasma is produced [15]. We have explored this interesting suggestion using simulations, and found such correlations.

Our results were published in a Physical Review Letter [16] and a longer Physics of Plasmas paper [17]. Chapter 2 of the thesis is largely a reproduction of the longer paper. Other authors using different analysis independently concluded that the development of electron-electron correlations in these plasmas is self-limiting [18, 19]. Heating of ions associated with the liberation of correlation energy also was considered by Murillo [20]. However, he treats the electrons only as a dielectric fluid that Debye shields the interaction between the ions. His analysis focuses on the liberation of correlation energy for a system of Debye shielded ions. Unfortunately, this approach misses the electron heating that dominates the early stages of the evolution, and the electron temperature determines the degree of shielding.

1.2 Guiding Center Atoms in Magnetized Ultracold Plasmas

The ATHENA and ATRAP collaborations at CERN have produced cold antihydrogen atoms by adding cold antiprotons to a cryogenic positron plasma in a Penning trap configuration [21, 22]. The sudden mixing of two cryogenic species is another way of producing an ultracold plasma. The ATHENA and ATRAP experiments have been a rich source of theory questions at the interface between plasma physics and atomic physics. Chapters 3 and 4 of this thesis focus on the dynamics of the weakly bound and strongly magnetized atoms produced in the experiments.

Three-body recombination is thought to be the dominant recombination process in these experiments and to produce very weakly bound atoms. The ATRAP collaboration measured atom binding energies in the range of a few meV [23], and one expects that ATHENA also produced atoms with binding energy in this range, although more deeply bound atoms may have been produced as well. Here, we focus on the weakly bound atoms. The magnetic field strength for the ATHENA and ATRAP experiments were three and five Tesla, respectively.

The weakly bound and strongly magnetized atoms are very different from high-n Rydberg atoms with a Kepler orbit. More properly these weakly bound and strongly magnetized pairs are called guiding center drift atoms [24, 25]. The characteristic cyclotron radius for the positron is much smaller than the separation between the positron and the antiproton. Likewise, the cyclotron frequency for the positron is much larger than the other dynamical frequencies for the atom. Under these circumstances the rapid cyclotron motion may be averaged out, and the dynamics of the positron treated by guiding center drift theory. The dynamics is quasi-classical because the characteristic binding energy is much smaller than the Rydberg energy (typically four orders of magnitude smaller).

Various motions for such a bound pair are possible. In a particular simple motion, the positron executes rapid and localized cyclotron motion, more slowly oscillates back and forth along the magnetic field in the Coulomb well of the antiproton, and more slowly still $\vec{E} \times \vec{B}$ drifts around the antiproton. In another type of motion, the positron $\vec{E} \times \vec{B}$ drifts in the field of the antiproton, and the antiproton $\vec{E} \times \vec{B}$ drifts in the field of the positron, the two traveling across the magnetic field in parallel. In a third type of motion, the antiproton executes a large cyclotron orbit around the positron which is effectively pinned to the magnetic field. In Chapter 3, we characterize and classify these motions as a function of the parameters and constants of the motion for the coupled positron-antiproton system.

Fortunately, a frequency ordering makes the dynamics integrable. The positron-antiproton system has six degrees of freedom so six constants of the motion are required for integrability. Four are exact constants: the Hamiltonian and the three components of total momentum. The remaining two are approximate constants (adiabatic invariants) that result from two frequency separations. Because the positron cyclotron frequency is much larger than other dynamical frequencies the cyclotron action is a good adiabatic invariant. Use of guiding center drift variables automatically takes this constant into account and removes the cyclotron motion from the problem. Because the frequency of field aligned oscillations is much larger than the remaining dynamical frequencies (associated with cross field motion) the action associated with the field aligned motion is a good adiabatic invariant.

There has been much previous work on the coupled electron-ion system in a strong magnetic field. A difficulty is that a true separation of the center of mass motion (transverse to the magnetic field) and the internal motion is not possible. However, Avron, Herbst, and Simon [26] found an effective separation by introducing the transverse pseudomomentum and showing that it is a constant of motion. The influence of the transverse center of mass motion on the internal motion is then accounted for by a pseudopotential that depends on the eigenvalue of the pseudomomentum. More recently this effective separation was applied to the hydrogen atom [27] and positronium [28].

In our classical analysis, the transverse components of pseudomomentum arise as two new momenta in a canonical transformation, and the pseudopotential enters the transformed Hamiltonian. Our analysis differs from the previous work in that the Hamiltonian is simplified by the use of the frequency separation. Introduction of the cyclotron action and the action for the field aligned bounce motion effectively averages the Hamiltonian over the rapid cyclotron and bounce motions, removing two degrees of freedom at the outset.

In the language of atomic physics, a double Born-Oppenheimer approximation is used. The remaining transverse dynamics is always integrable, and a transverse action can be introduced. Since the Hamiltonian is expressed as a function of the cyclotron action, bounce action, and transverse action, a general expression for the quantum energy levels can be obtained using the Bohr-Sommerfeld quantization rules. Of course the assumption of weak binding justifies the quasi-classical approximation – with the possible exception of the cyclotron motion, as will be discussed.

Chapter 4 discusses the motion of these weakly bound atoms in the magnetic and electric field of the trap. Because the binding is so weak, even a modest electric field produces a significant polarization of an atom. A gradient in the field then exerts a force on the atom, causing acceleration. Typically, the atom is moving across the magnetic field, and it is the effective electric field in the moving frame of the atom that causes the polarization and the acceleration. In the laboratory frame, both electric and magnetic forces must be taken into account.

In the experiments, the magnetic field is nearly uniform and the electric field varies by only a small amount over the dimensions of the atom. Also, the time scale for the internal dynamics of the atom is short compared to the time scale for the atom to move a significant distance. Taking advantage of these orderings, we obtain an approximate equation of motion for the atom center of mass. The only remnant of the atom internal dynamics that enters the equation of motion is the polarizability. The approximate equation of motion provides a substantial simplification because it averages over the rapid internal dynamics of the atom.

The analysis divides naturally into two parts: the derivation of the equation of motion and the calculation of the polarizability. We derive an approximate equation of motion for the expectation value of the atom center of mass coordinates, $\langle\vec{R}_{\mathrm{cm}}\rangle(t) \equiv \langle\Psi|\vec{R}_{\mathrm{cm}}|\Psi\rangle$. The derivation of the equation of motion depends on the spatial and temporal orderings mentioned above but otherwise is general. On the other hand, determination of the polarizability requires a more detailed specification of the internal dynamics for the atom. We evaluate the polarizability for the special case of guiding center drift atom [24].

As a simple application we use the approximate equation of motion to discuss the radial trapping of weakly bound atoms in the large space charge field of a long positron column. The geometry and field strengths used are characteristic of the ATHENA experiments. Orbits from the approximate equation of motion are shown to be in good agreement with those from lengthy numerical solutions of the coupled positron-antiproton equations of motion. These latter solutions involve over a million cycles of the internal atom dynamics. The comparison demonstrates the fidelity of the approximate equation of motion and also the substantial simplification it provides in averaging out the rapid internal dynamics.

The solution shows that the weakly bound atom can be trapped radially in the large electric field region near the edge of a long cylindrical positron column. The reason for the trapping is easy to understand physically. For a uniform density unneutralized column of positrons, the radial space charge field increases linearly with radius inside the column and falls off inversely with radius outside the column. Thus, there is a region of large field near the plasma edge, and polarizable material (the atom) is attracted to a region of maximum field.

We will find that the polarization forces create a potential well of approximate depth αE^2, where α is the polarizability of the atom and E is the electric field strength. In Gaussian units, the polarizability has the dimensions length cubed, and the polarizability for an atom of size r_a is of order $\alpha \sim r_a^3$. Since the binding energy for an atom is of order e^2/r_a, the depth of the well scales inversely with the cube of the binding energy. Thus, the effects discussed here are more pronounced for weakly bound atoms. Of course, a weakly bound atom suffers field ionization from a relatively weak field. The critical field for ionization is approximately $E \sim e/r_a^2$. Using this field strength as an upper bound for E shows that the maximum well depth is the binding energy of the atom:

$$\alpha E^2 = (\alpha/r_a^3)r_a^3\left(\frac{E}{e/r_a^2}\right)^2\left(\frac{e}{r_a^2}\right)^2 \lesssim \frac{e^2}{r_a}$$

For the example discussed in the last paragraph, radial trapping is possible only when the atom binding energy is larger than the kinetic energy of the atom center of mass.

The ATRAP collaboration uses field ionization as a diagnostic, and the ionization region is some distance from the plasma. As a second application of the approximate equation of motion, we determine trajectories followed by weakly bound atoms in moving from the recombination region (inside the positron plasma) to the field ionization region. Depending on the parameters, a straight line orbit may or may not be a good approximation. We will see that the polarization forces produce a significant deflection of the atom when the binding energy is larger than the center of mass kinetic energy. Knowledge of the trajectories is an important input to estimates of antihydrogen production rates based on solid angle considerations.

We also calculated the critical electric field for ionization as a function of the actions (or quantum numbers) that define the atomic state. The atom is assumed to start in a low field region and to move into a region of gradually increasing electric field. As the electric field rises, the binding energy of the atom does not stay constant. However since the electric field experienced by the atom changes by only a small amount on the time scale of the atom internal motion, the actions characterizing the internal motion are good adiabatic invariants until just before field ionization. Thus, the critical field for ionization can be predicted as a function of the actions, or equivalently as a function of the atom state in the low field region.

This work is discussed in a published Physics of Plasmas paper [25], a published Physical Review Letter [29], and a submitted Physics of Plasmas paper [30]. Chapter 3 is largely a reproduction of the published Physics of Plasmas paper and Chapter 4 a reproduction of the submitted Physics of Plasmas paper. Another group [31] independently obtained some results on the internal motion and field ionization of guiding center atoms, but their work was numerical and did not explicitly take advantage of the frequency ordering and adiabatic invariants exploited here.

Chapter 2

Numerical Simulation of Ultracold Plasmas

2.1 Abstract

In recent experiments ultracold plasmas were produced by photoionizing small clouds of laser cooled atoms. This paper presents the results of molecular dynamic simulations for the early time evolution of such plasmas. Contrary to earlier speculation, no evidence of strong electron-electron correlations is observed in the simulations even if the initial value of the coupling parameter ($\Gamma_e = e^2/akT_e$) is much larger than unity. As electron-electron correlations begin to develop, the correlation energy is released to heat the electrons, raising the electron temperature to the point where $\Gamma_e \sim 1$ and limiting further development of correlation. Further heating of the electrons occurs as a by-product of three-body recombination. When a model of laser cooling is added to the simulation, the formation of strong ion-ion correlation is observed. Contrary to earlier suggestion, the rate of three-body recombination is observed to be in reasonable agreement with the traditional formula, $R = 3.9{\times}10^{-9}\,\mathrm{sec}^{-1}[n\ (\mathrm{cm}^{-3})]^2\ [T_e(^\circ K)]^{-9/2}$, but care must be taken to use the correct temporally evolving temperature, T_e. The simulations are challenging because it is necessary to follow three-body recombination into weakly

bound (high n quasi-classical) Rydberg states, and the time scale for such states is short compared to that for the plasma dynamics. This kind of problem was faced earlier in computational astrophysics when studying binary star formation in globular clusters and the simulation method used here is adapted from such studies.

2.2 Introduction

In recent experiments [1, 2, 3, 4], ultracold neutral plasmas were produced by abruptly photoionizing small clouds of laser cooled Xenon atoms, carefully adjusting the energy of the ionizing photons to barely exceed the ionization potential. Electron temperatures as low as $T_e \simeq 0.1$ K were reported. The ions inherited the even lower temperature of the laser cooled atoms ($T_i \simeq 10$ mK). In closely related experiments [6, 7, 8], the cooled atoms were photoexcited to high-n Rydberg states, and an ultracold plasma resulted from collisional processes. Here, we focus on the plasmas that were produced directly by photoionization, since the initial conditions for the plasma state are well defined.

These novel plasmas present interesting challenges to theory. For example, it has been suggested that the initial low temperature of the plasmas implies strong correlation [1]. Also, there has been a worry that the traditional theory of three-body recombination is not applicable at the low temperatures of the plasmas [1, 3]. In contrast, we argue here that rapid intrinsic heating of the electrons raises the temperature to the point where strong correlation cannot develop and where the traditional theory of three-body recombination is approximately correct. These arguments are substantiated by molecular dynamics simulations of the early time plasma evolution. We also simulate a proposed experiment [15] in which the ions that result from photoionization are themselves laser cooled, and in this simulation strong ion-ion correlation is observed.

At the low temperatures of these plasmas, three-body recombination is very rapid–much faster than radiative recombination [10]. Three-body recombination proceeds through a sequence of collisions, with the recombination energy carried off by an electron, rather than a photon. One can think of the process as the collisional approach to a state of thermal equilibrium, which is a neutral gas.

The rate of three-body recombination is controlled by a kinetic bottleneck [10] at a binding energy of a few kT_e, where k is the Boltzmann constant and T_e is the electron temperature. For binding energies above the bottleneck, subsequent collisions typically re-ionize an electron-ion pair. However, occasionally a collision leaves a bound pair with energy below the bottleneck. Then subsequent collisions produce a cascade to ever deeper binding. Thus, a pair can be declared recombined when it passes below the bottleneck. The simulations follow many bound pairs as they cascade to energies below the bottleneck. Since the critical range of binding energies scales like kT_e and since kT_e is orders of magnitude smaller than the Rydberg energy, the essential physics can be captured by a classical molecular dynamics simulation.

The necessity of following the recombination into weakly bound (high-n) Rydberg states is the main challenge to the simulation. The difficulty is that the time scale for an electron orbit in such a state is much shorter than the time scale for the orbit of a typical unbound electron. In plasma simulations of this kind some authors have used two time scales: one for particles with near neighbors and another for the remaining particles [11]. Another variant is to use piecewise analytic solutions for Kepler orbits. We prefer a treatment that doesn't make special assumptions about particles with near neighbors, but seamlessly encompasses the continuum of time scales required.

Fortunately, such a treatment was developed previously in computational studies of binary star formation in globular clusters. The binary stars are the analog of the high-n Rydberg atoms and the cluster is the analog of the plasma cloud. We have adapted a code developed by Aarseth [12] for the study of binary star formation.

The code is a molecular dynamics simulation in the sense that the force on a given particle from each of the other particles is calculated directly. Time integration is effected with a predictor corrector scheme using a fourth order polynomial fit to the orbit. The crucial feature is that the time step for each particle is adjusted independently depending on such factors as the rate of change of the acceleration. Thus, a bound electron can have a much shorter time step than a typical electron without slowing down the whole simulation. To keep all of the particles moving in near synchrony, the code advances next the time step for the particle that is furthest behind in absolute time. To evaluate the force on this particle, the other particle positions are extrapolated back in time to exact synchrony using the polynomial fit to the orbits.

As one would expect, there are interesting parallels between three-body recombination in these plasmas and binary star formation in clusters. We will see that a by-product of three-body recombination is heating of the unbound electrons and even production of suprathermal electrons that are ejected from the plasma. Likewise, binaries "harden" by giving kinetic energy to other stars through collisional interactions, sometimes ejecting stars at high velocity from the core of the cluster [14]. This heating mechanism is now thought to be the primary mechanism for supporting globular clusters against gravothermal contraction and core collapse [13].

Two recent papers [18, 19] have provided a good theoretical description of the long term evolution of ultracold plasma clouds. Our work is complementary in that it focuses on the early time microscopic physics: the correlation physics and the cascade process of three-body recombination. The Aarseth simulation method is ideally suited to focus on this physics.

2.3 Correlation and Initial Heating

2.3.1 Theory Background

For a plasma in thermal equilibrium, the strength of correlation is determined by the coupling parameter $\Gamma = e^2/akT$, where a is the Wigner-Seitz radius (i.e., $4\pi a^3 n/3 = 1$) [9]. We use cgs units throughout the paper. For the maximum density and lowest temperatures reported in the experiments [i.e., $n \simeq 2\times10^9$ cm^{-3}, $T_e \simeq 0.1$ K, and $T_i \simeq 10$ μ/K], the electron coupling parameter has the value $\Gamma_e \simeq 30$, and the ion coupling parameter is much larger. Thus, one might expect the low temperatures to be associated with strong correlation.

However, the plasma is not created in a state of thermal equilibrium. Before photoionization, the neutral atoms are uncorrelated, so immediately after photoionization ion-ion and electron-electron correlations are negligible. There may be some electron-ion correlation that remains as an artifact of the ionization process, but this is not a thermal equilibrium correlation. For example, there is no long range order.

Thermal equilibrium correlations can develop only through the action of Coulomb interactions as the plasma evolves. However, as the electron correlations begin to develop, the correlation energy is released to the electron plasma as heat, and this limits the strength of correlation reached. To reach a correlation strength corresponding to $\Gamma_e \simeq 1$, each electron picks up thermal energy $kT_e \simeq e^2/a$. At this point the coupling parameter has the value

$$\Gamma_e = e^2/akT_e \simeq (e^2/a)/(e^2/a) = 1,$$

so further development of correlation ceases. Even if the initial electron temperature were zero, corresponding formally to infinite Γ_e, strong correlation would not develop.

We hasten to add that the initial electron temperature would not be zero even if the energy of the ionizing photons exactly matched the ionization potential (for a single isolated atom). Because of the Coulomb fields from neighboring electrons and ions, the ionization potential for atoms in the plasma varies from atom to atom by an amount of order e^2/a, and this sets a minimum temperature of order $kT_e \sim e^2/a$ [18]. The picture is further complicated by the fact the ionization process takes place over a finite time. Typically, heating due to the release of correlation energy is occuring while the plasma is being created.

In the following we ignore these complications and consider simulations where the initial electron and ion temperatures (or more precisely, kinetic energies) are zero, corresponding formally to infinite initial values for Γ_e and Γ_i. This gives correlations the best opportunity to develop. The observed failure of strong correlations to develop then emerges as an intrinsic consequence of the dynamics. The release of correlation energy as heat limits the development of correlation.

The time scale for this electron dynamics is of order ω_{pe}^{-1}, where $\omega_{pe} = \sqrt{4\pi ne^2/m_e}$ is the electron plasma frequency. On a longer time scale (i.e., $\omega_{pi}^{-1} = \sqrt{m_i/m_e}\,\omega_{pe}^{-1}$), ion-ion correlations begin to develop and the released energy heats the ions limiting the effective ion-ion correlation strength.

Murillo [20] considered ion heating by the release of correlation energy, but he treated the electrons as a dielectric fluid, and focused on the liberation of correlation energy for a system of Debye shielded ions. Unfortunately, this approach misses the electron heating that dominates the early stages of evolution, and the degree of shielding depends through the Debye length on electron temperature [see Section 2.3.3].

2.3.2 Simulation Results

By using properly scaled length and time, the number of parameters that define a simulation was reduced to a minimum. Length was scaled by the Wigner-Seitz radius a and time by the inverse of the electron plasma frequency ω_{pe}^{-1}. With these scalings, the equations of motion were specified by three parameters: the mass ratio m_i/m_e, the number of electrons (which was equal to the number of ions) N, and a rounding parameter ε for the Coulomb potential. To avoid singularities, the Coulomb potential was rounded to the form

$$1/\sqrt{|\vec{r}_1 - \vec{r}_2|^2/a^2 + \varepsilon^2} \tag{2.1}$$

where $\varepsilon \ll 1$. For this simulation, ε was chosen to have the value 1/31. This value is small enough that the rounded potential was a good approximation to the Coulomb potential for the vast majority of particles. For a few deeply bound pairs, the approximation was marginal, but these deeply bound pairs were not the focus of this simulation. A further decrease in the value of ε did not change the temperature evolution or the correlation function. The mass ratio was chosen to have the value $m_i/m_e = 100$. This relatively low value insured that the ions had time to participate in the correlation dynamics during the course of the simulation. The electron-electron correlation function relaxed to a steady-state form in a few scaled time units, and the ion-ion correlation function in a time that was longer by $\sqrt{m_i/m_e} = 10$. The simulation ran for $t_{\max}\omega_{pe} = 70.9$ scaled time units, and energy was conserved to an accuracy of $10^{-5}Ne^2/a$, where Ne^2/a is the scale of the total energy.

One might worry that the rapid heating is not resolved by the simulation since the heating occurs in about one unit of time (i.e., ω_{pe}^{-1}). However, the unit of time is not the time step. The time step is variable, but each particle has many time steps (typically hundreds) in one unit of time, so that the heating dynamics is adequately resolved.

So that the correlation function assumed the simple form $G(\vec{r}_1, \vec{r}_2) = G(|\vec{r}_1 - \vec{r}_2|)$, we arranged the initial and boundary conditions to insure uniform plasma density. Specifically, 4096 electrons and 4096 ions were distributed randomly inside a spherical volume bounded by a reflecting wall. The correlation measurements were made well away from the wall. In scaled units, the radius of the sphere was determined by the number of electrons, $(r_s/a)^3 = N$. As mentioned earlier, the initial temperatures for both electrons and ions were chosen to be zero.

The initial density profiles for the experimentally produced plasma clouds were Gaussian [1, 2, 3]. One should think of the uniform density spherical plasmas as a small central section of a larger Gaussian cloud.

Figure 2.1 shows a plot of the scaled electron temperature [i.e., $kT_e(t)/(e^2/a) = 1/\Gamma_e(t)$] versus the scaled time $t\omega_{pe}$. To obtain this plot, histograms of electron kinetic energy were made (excluding tightly bound electrons) and matched to Maxwellians. Rapid heating to $\Gamma_e \simeq 1$ is clearly visible. The longer-term slower heating is associated with three-body recombination.

Indeed, the heating from three-body recombination is slightly larger than appears from this picture. The rate of increase in the electron temperature is reduced somewhat by collisional cooling on the ions [see Section 2.3.3]. This effect is exacerbated by the artificially low mass ratio $m_i/m_e = 100$. By skipping ahead

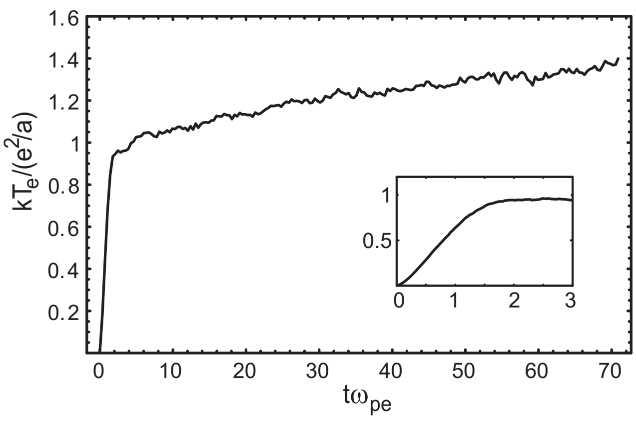

Figure 2.1: Scaled temperature versus scaled time. The insert shows change of temperature during the time $t\omega_{pe} < 3$ when rapid heating occurs.

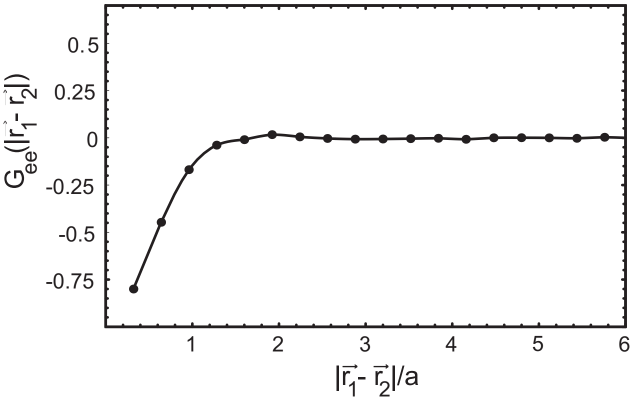

Figure 2.2: Electron-electron correlation function, averaged from $t\omega_{pe} = 3.5$ to $t\omega_{pe} = 7.1$.

to Fig. 2.13, one can see the electron heating for the case of realistic mass ratio (for Xe ions), where the electron-ion collisional energy transfer is negligibly small over the duration of the simulation.

Figure 2.2 shows the electron-electron correlation function averaged over the time interval $t\omega_{pe} = 3.5$ to 7.1. The correlation function started out flat, corresponding to randomly distributed electrons, but quickly relaxed to the form shown in Fig. 2.2 and retained this form. The only change with increasing time was in the width of the region near $|\vec{r}_1 - \vec{r}_2| = 0$ where $G_{\rm ee} \simeq -1$. This value

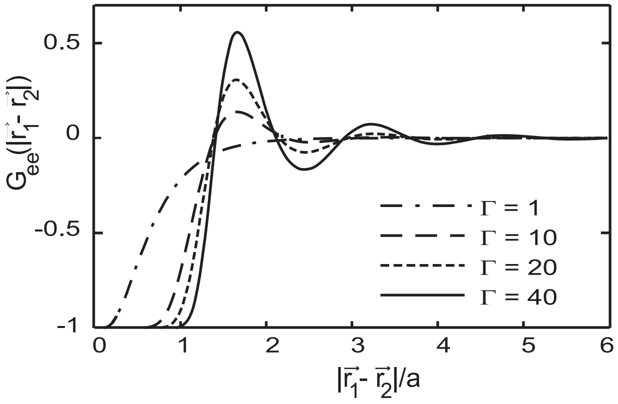

Figure 2.3: Correlation function for one component plasma.

for $G_{\rm ee}$ reflects the fact that it is energetically unfavorable for two electrons to be at the same location, and the width of the region is of order $|\vec{r}_1 - \vec{r}_2| \simeq e^2/kT_e$. In measurements of $G_{\rm ee}$ at later times the width was observed to decrease as the electron temperature slowly increased.

For comparison, Fig. 2.3 shows the correlation function for a one component plasma (OCP) in thermal equilibrium at correlation strengths $\Gamma = 1$, 10, 20, and 40 [9, 32]. As expected, the correlation curve in Fig. 2.2 corresponds in shape to the $\Gamma = 1$ curve in Fig. 2.3. The curves in Fig. 2.3 for $\Gamma = 10$, 20, and 40 exhibit oscillations indicating the presence of local order, that is, of a local lattice. The lack of these oscillations in Fig. 2.2 shows that such order was missing in the electron distribution for the ultracold plasma.

Figure 2.4 shows the ion-ion correlation function averaged over the time interval $t\omega_{pe} = 67.4$ to 70.9. Again the correlation function started out flat and relaxed to the form shown, although the relaxation time was longer than for the electrons. The absence of oscillations shows that local order was missing.

Figure 2.5 shows the electron-ion correlation function averaged over the time interval $t\omega_{pe} = 3.5$ to 7.1. In this case, $G_{\rm ei}$ is positive near $|\vec{r}_1 - \vec{r}_2| = 0$, since it is energetically favorable for an electron to be near an ion. However, this

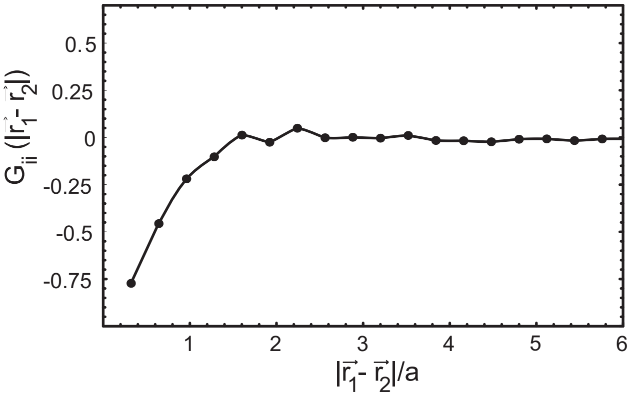

Figure 2.4: Ion-ion correlation function averaged over the time interval $t\omega_{pe} = 67.4$ to $t\omega_{pe} = 70.9$.

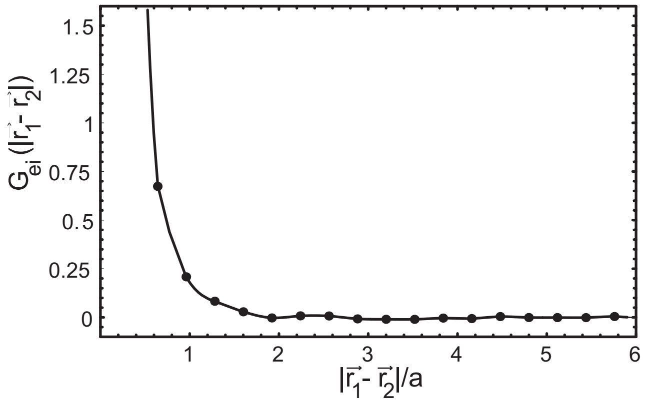

Figure 2.5: Electron-ion correlation function averaged over the time interval $t\omega_{pe} = 3.5$ to 7.1.

positive electron-ion correlation is not an indication of the local order characteristic of strong correlation; rather it reflects Debye shielding and the beginning of recombination. This latter observation also was made in reference [18].

Finally, we note that the experiments themselves provide some evidence against early strong correlation. The plasma expansion is driven by the electron pressure, but the effective pressure becomes negative for a strongly correlated plasma. This effect is well known from the theory of one component plasmas [32], and is easy to understand physically. Because of correlations, the electrostatic forces of interaction bind the plasma together giving rise to an effective pressure that is negative. If there were no intrinsic heating and the cloud were strongly correlated, the pressure would be negative and the cloud would not expand. Alternatively, one can rule out expansion on energetic grounds. The correlation energy is negative [i.e., $U_{\text{corr}} \sim -N(e^2/a)$], so plasma expansion can occur only by supplying positive kinetic energy [i.e., $(3/2)NkT_e$]. However, in the limit of strong correlation, $\Gamma_e = e^2/akT_e \gg 1$, there is not enough kinetic energy to drive the expansion.

2.3.3 Ion-Ion Correlation in Laser Cooled Clouds

Killian noted that both Strontium (Sr) atoms and Sr^+ ions can be laser cooled and suggested that a strongly correlated ion plasma might be achieved by laser cooling the ions shortly after the plasma is produced [15]. We have explored this interesting suggestion using simulations.

The laser cooling was modeled in the simulations by periodically reducing the speed of each ion by a small percent. Two simulations were carried out: one for which the initial electron temperature was relatively high [i.e., $kT_e(0)/(e^2/a) = 1/\Gamma_e(0) = 31$] and another for which the initial temperature of both species was zero. For both simulations, 2048 electrons and 2048 ions were followed for the time $t_{\max}\omega_{pe} = 354$, and total energy (plasma energy plus extracted energy) was conserved to better than $6 \times 10^{-4} Ne^2/a$. The mass ratio and the rounding parameter had the values $m_i/m_e = 100$ and $\varepsilon = 1/62$, and the particles initially were placed randomly inside a spherical volume bounded by a reflecting wall.

For the case of high initial electron temperature, Figs. 2.6(a) and 2.6(b) show the evolution of the ion and electron temperatures as a function of time. The ion temperature increased initially as ion-ion correlations develop and the

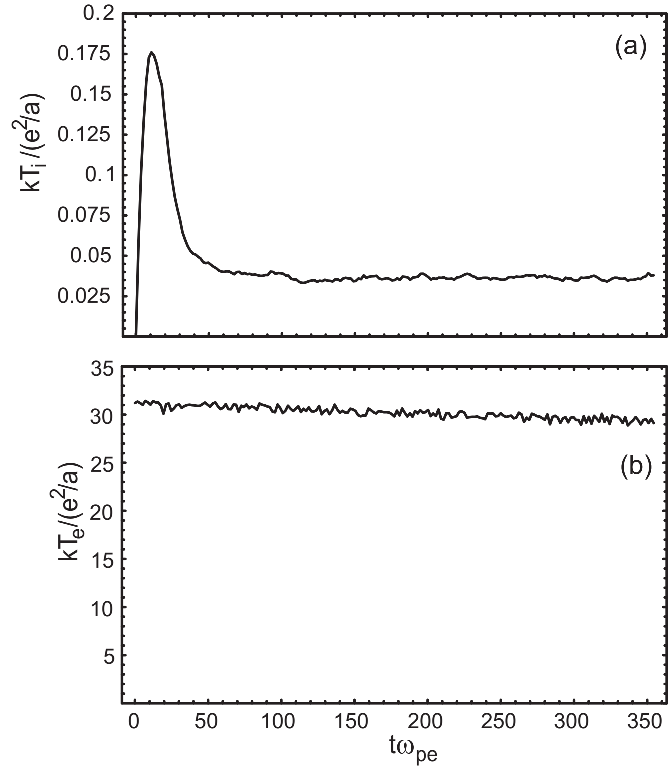

Figure 2.6: Evolution of temperature as a function of time for the case of laser cooled ions and high initial electron temperature. (a) - ion temperature; (b) - electron temperature.

correlation energy was released to heat the ions. The simulated laser cooling then reduced the ion temperature to a steady state value given by the balance between collisional heating from the electrons and ion cooling. Figure 2.6(b) shows that the electron temperature gradually decreased, as the electrons heated the ions. For the relatively high electron temperature in this simulation, three-body recombination and the concomitant heating of electrons was negligible. Very few bound pairs were observed.

Figure 2.7 shows the ion-ion correlation function averaged over the time interval $t\omega_{pe} = 106$ to 354, which is the time interval of steady state ion temperature. The peak and the oscillations show the existence of order. Comparing to Fig. 2.3 for an OCP suggests a correlation strength in the range $\Gamma_i = 20$, which

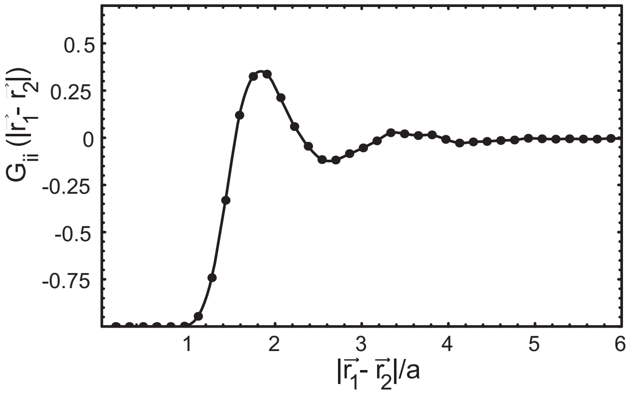

Figure 2.7: Ion-ion correlation function averaged over time interval $t\omega_{pe} = 106$ to 354 for the case of laser-cooled ions and high initial electron temperature.

is in good agreement with the steady state ion tmperature of Fig. 2.6(a) [i.e., $kT_i/(e^2/a) = 0.05$ or $\Gamma_i = 20$].

To see how the steady state ion temperature would scale with the electron to ion mass ratio and with the electron temperature, we note that weakly correlated electrons heat cold ions collisionally at the rate [33]

$$(\text{Heating})_{e,i} = \sqrt{32\pi}\frac{e^4 n}{\sqrt{m_e k T_e}}\frac{m_e}{m_i}\ln\left(\frac{\sqrt{3}}{\Gamma_e^{3/2}}\right). \tag{2.2}$$

Up to a numerical factor this expression is simply $\nu_{ei}(m_e/m_i)kT_e$, where ν_{ei} is the usual electron-ion collision frequency. If the laser cooling rate is given by $\gamma_c T_i$, then the steady state ion temperature is given by power balance

$$\gamma_c T_i = \sqrt{32\pi}\frac{e^4 n}{\sqrt{m_e k T_e}}\frac{m_e}{m_i}\ln\left(\frac{\sqrt{3}}{\Gamma_e^{3/2}}\right). \tag{2.3}$$

The steady state ion temperature in Fig. 2.6(a) is given by this relation to within a factor of 2. To make T_i small, there is advantage in using heavy ions and hot electrons, although this latter advantage doesn't cut in until the scaled electron temperature $kT_e/(e^2/a) = 1/\Gamma_e$ exceeds about 10^3. For scaled temperature between 1 and 10^3, the $1/\sqrt{T_e}$ dependence and the $\ln(\sqrt{3}/\Gamma_e^{3/2})$ dependence compensate one another leaving the heating rate nearly independent of T_e.

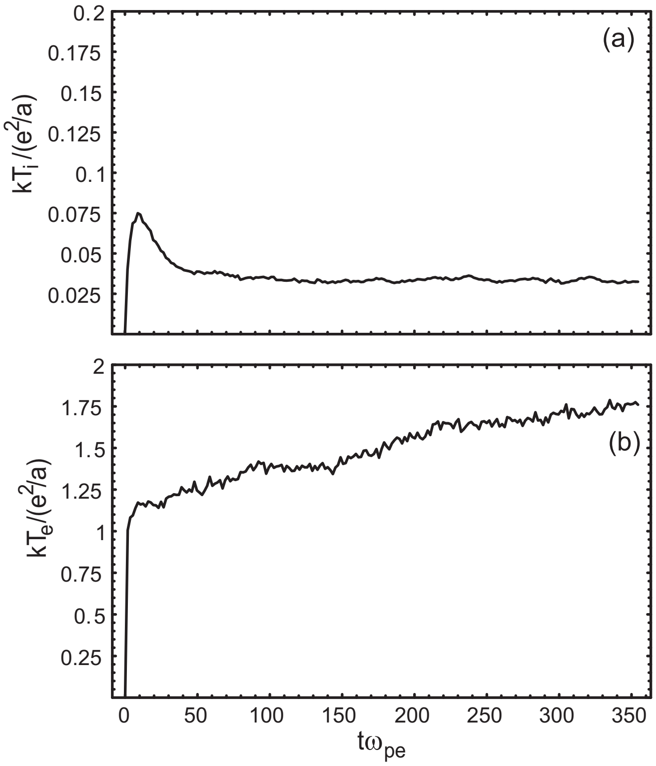

Figure 2.8: Evolution of temperature as a function of time in the case of laser–cooled ions and zero initial electron temperature. (a) - ion temperature; (b) - electron temperature.

More important reasons for using warm electrons are that the rate of three-body recombination is greatly reduced and the ion-ion interactions are not shielded. The reduction of the effective ion-ion coupling strength by electron shielding is illustrated by the simulations where both species were started with zero temperature. Figures 2.8(a) and 2.8(b) show the ion and electron temperature as a function of time. Initially both species are heated as correlation energy is released. Ion cooling then reduces the ion temperature to a steady state value that is in accord with Eq. (2.3). The electron temperature continues to rise gradually because heating due to three-body recombination exceeds collisional cooling on the ions.

Figure 2.9 shows the ion-ion correlation function averaged over the time interval $t\omega_{pe} = 106$ to 354. In this case, the evidence of order is less pronounced

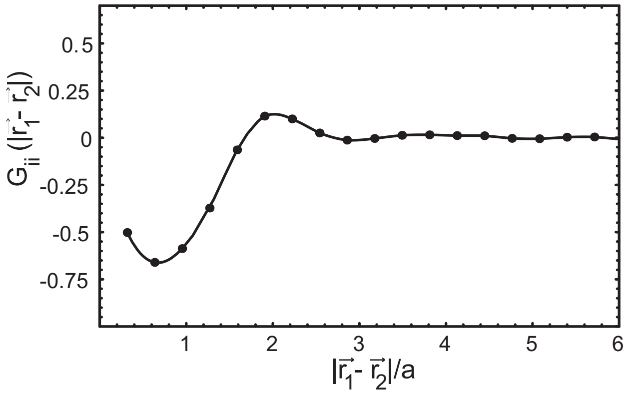

Figure 2.9: Ion-ion correlation function averaged over the time interval $t\omega_{pe} = 106$ to 354 for the case of laser-cooled ions and zero initial electron temperature.

than for the previous simulation [see Fig. 2.7]. Comparison to Fig. 2.3 for an OCP suggests a coupling parameter of $\Gamma_i < 10$, which is lower than that for the previous simulation, even though the two simulations have nearly the same steady state ion temperatures.

Presumably, the reason for the difference is that the electrons shielded the ion-ion interactions somewhat in the second simulation reducing the effective coupling strength. For weakly correlated electrons, the Debye shielded ion-ion interaction,

$$\mathrm{v} = \frac{e^2}{r}\exp(-r/\lambda_D), \tag{2.4}$$

suggests an effective ion coupling strength $\Gamma_i' = \Gamma_i \exp(-a/\lambda_D)$ [20]. Here, $\lambda_D = (kT_e/4\pi ne^2)^{1/2}$ is the electron Debye length. The ratio $a/\lambda_D = \sqrt{3\Gamma_e}$ is small for hot electrons (i.e., $\Gamma_e \ll 1$), but is order unity for $\Gamma_e \sim 1$ implying a significant reduction in the effective correlation strength. For $\Gamma_e > 1$ the shielding is large but is not correctly described by expression (2.4).

Another interesting effect is apparent in Fig. 2.9. Note that $G_{ii}(|\vec{r}_1 - \vec{r}_2|/a)$ increases for $|\vec{r}_1 - \vec{r}_2|/a \lesssim 1$. We believe that weakly bound electron-ion pairs are polarized by and attracted to neighboring ions, and this causes $G_{ii}(|\vec{r}_1 - \vec{r}_2|/a)$ to turn upward at small $|\vec{r}_1 - \vec{r}_2|/a$. We checked this interpretation by removing ions with bound electrons from the sample used to evaluate G_{ii}, and found that G_{ii} goes to zero for $|\vec{r}_1 - \vec{r}_2|/a \lesssim 1$.

Apparently, the upturn occurs only for simulations where both the electrons and the ions are relatively cold. The electrons must be cold to have recombined pairs, and kT_i must be smaller than or comparable to the potential energy of interaction between the ion and the induced dipole. Note that the upturn does not occur in Fig. 2.7 or in Fig. 2.4.

2.4 Three-body Recombination

2.4.1 Theory Background

The traditional theory of three-body recombination, developed in a classic paper by Mansbach and Keck [10], yields the following expression for the recombination rate (per ion)

$$\mathcal{R} = 3.9 \times 10^{-9} \left[\frac{n}{\mathrm{cm}^{-3}}\right]^2 \left[\frac{T_e}{{}^\circ K}\right]^{-9/2} \mathrm{sec}^{-1}. \tag{2.5}$$

The predicted rate is very large at low temperature because of the scaling $T_e^{-9/2}$. However, the traditional theory assumes that $\Gamma_e < 1$, and rate expression (2.5) can be trusted only in this regime. Recently, Hahn [34] extended the theory into the regime where $\Gamma_e > 1$.

For the highest density and lowest initial electron temperature reported in the experiments with ultracold plasma clouds, the initial value of Γ_e is larger than unity [i.e., $\Gamma_e(t = 0) \simeq 30$], so one might worry that the traditional theory would not be applicable. However, as we have seen, rapid initial heating reduces the value of Γ_e to unity or less. Thus, the experiments are on the edge of the range where the traditional theory is valid. The rate can be off by order unity, but not by the factor $(30)^{9/2}$ that one might have expected.

A deeper understanding of rate expression (2.5) requires an understanding of the kinetic bottleneck. To this end, consider a single ion at rest in a sea of electrons (neutralized by a uniform background charge). Suppose further that the Coulomb potential well for the ion is made flat at some relatively deep potential (below the bottleneck). When the system is in a state of thermal equilibrium, electrons are constantly going into and out of the well. The bottleneck can be understood by calculating the one way thermal equilibria flux toward deeper binding. Using the Gibbs distribution and insight gained from a Monte Carlo analysis, Mansbach and Keck [10] argued that the flux through a phase space surface characterized by binding energy E is proportional to

$$(\text{Flux})_{\downarrow} \sim \frac{1}{E^4}\exp[-E/kT_e]. \tag{2.6}$$

The flux is the product of a phase space factor $1/E^4$ and a Boltzmann factor. For small values of $-E/kT_e$ the flux is large because the phase space factor, $1/E^4$, is large. For large $-E/kT_e$, the flux is large because the Boltzmann factor is large. The minimum at $E = -4kT_e$ is the kinetic bottleneck. Electrons come into and out of the well many times before passing through the bottleneck. However, once they have fallen below the bottleneck, they continue to ever deeper binding. With this picture in mind, note that expression (2.5) is an evaluation of the one way flux through the bottleneck.

The reason that a collision almost always removes energy from a deeply bound pair can be understood dynamically. Consider an electron-ion pair with binding energy $|E| \gg kT_e$. On the average, the kinetic energy of the bound electron also is $|E|$. Consider a close collision with an electron that approaches with kinetic energy kT_e. Typically the collisional dynamics divides the kinetic energy more or less evenly between the two electrons, so one of the two leaves with energy $|E|/2 \gg kT_e$. The remaining electron is then bound more deeply. Incidentally, this simple picture shows how suprathermal electrons are produced as a by-product of the cascade to deeper binding.

2.4.2 Simulation Results

Our most extensive simulation was used to study three-body recombination. The evolution of 4096 electrons and 4096 ions was followed for a scaled time $t_{\max}\,\omega_{pe} = 354$, which required a month run on an XP-1000 alpha workstation. Energy was conserved to $2 \times 10^{-4} N e^2/a$.

For this simulation, a realistic mass ratio was used (for Xe^+ ions), and the electrons and ions were distributed initially with a Gaussian density profile in accord with experiment. In scaled units, the mean-square radius of the Gaussian is specified by the number of electrons through $\langle r^2 \rangle / a^2 = (6/\pi)^{1/3} N^{2/3}$. In potential (2.1), the rounding parameter was chosen to have the value $\varepsilon = 1/62$, which is small enough that the recombination dynamics (passage through the bottleneck) was treated accurately. Specifically, the inverse $1/\varepsilon = 62$ is much larger than the scaled binding energy at the bottleneck [i.e., $-E_b/(e^2/a) = 4/\Gamma_e \lesssim 7$]. Since $1/\varepsilon = 62$ is comparable to the scaled binding energy of the most tightly bound pairs at the end of the simulation, the cascade rate to deeper binding for these pairs may have been slightly suppressed. Since the focus of this simulation is three-body recombination, rather than the rapid initial heating, the simulation started with a small but finite initial electron temperature [i.e., $kT_e/(e^2/a) = 1/\Gamma_e = 0.31$].

Figure 2.10 shows a picture of the cloud (red dots are electrons and blue dots are ions) at the end of the run. Many of the electrons in the surrounding halo were ejected from the cloud as suprathermal electrons produced as a by-product

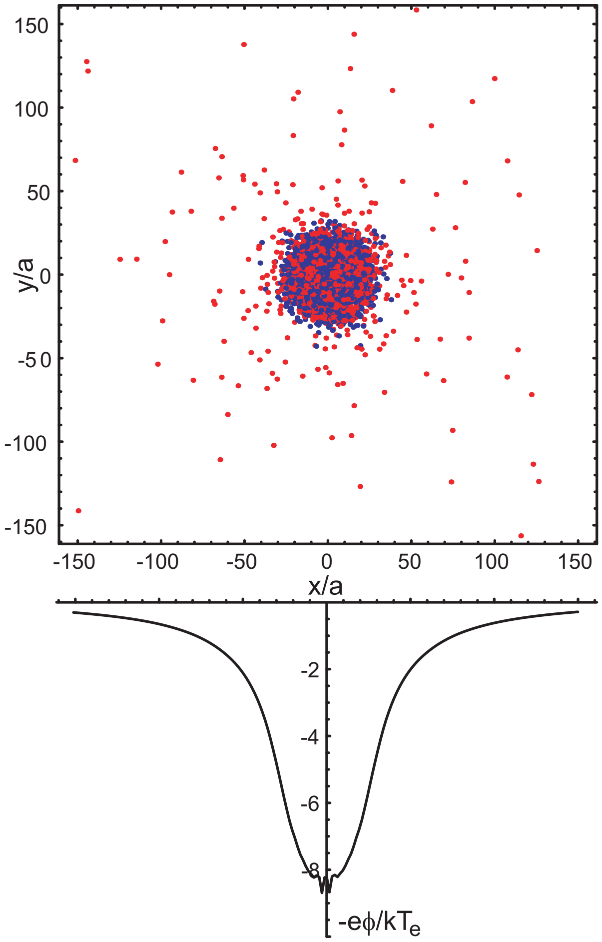

Figure 2.10: Cloud at the end of the run, $t\omega_{pe} = 354$; red dots are electrons and blue dots are ions. Part of the halo consists of suprathermal electrons that were produced as a by-product of three-body recombination. Also shown is a plot of the potential in the cloud at the end of the run.

of three-body recombination.

Figures 2.11(a), (b), (c), and (d) show binding energy histograms for the four times $t\omega_{pe} = 0$, 117, 234, and 354. For a bound electron, the binding energy is the kinetic energy plus the potential energy in the field of the nearest ion. Each figure displays the number of particles in bins of scaled binding energy ranging from $E/(e^2/a) = -1$ to -25. One can see the temporal progression to deeper binding.

Although the bound electrons were far from thermal equilibrium, the un-

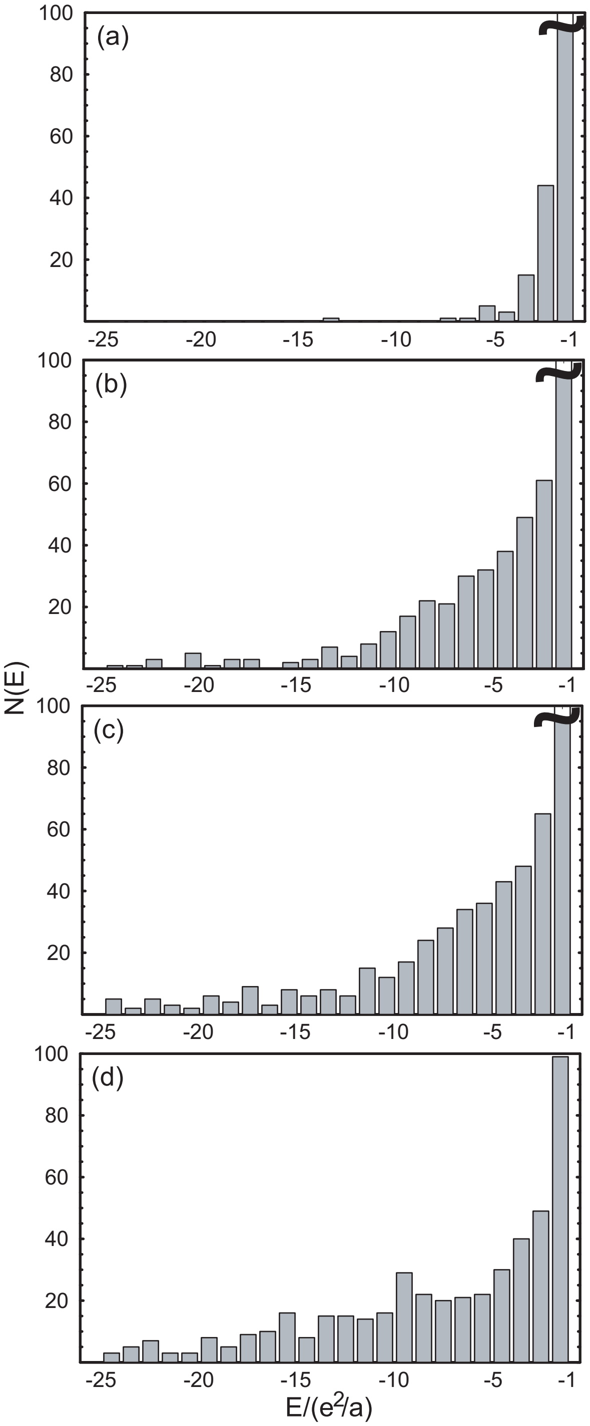

Figure 2.11: Binding energy histograms at (a) $t\omega_{pe} = 0$, (b) $t\omega_{pe} = 117$, (c) $t\omega_{pe} = 234$, (d) $t\omega_{pe} = 354$. Each column shows the number of electrons in that energy bin. The squiggle at the top of the column for the lowest energy bin indicates that the number exceeds the range of the graph.

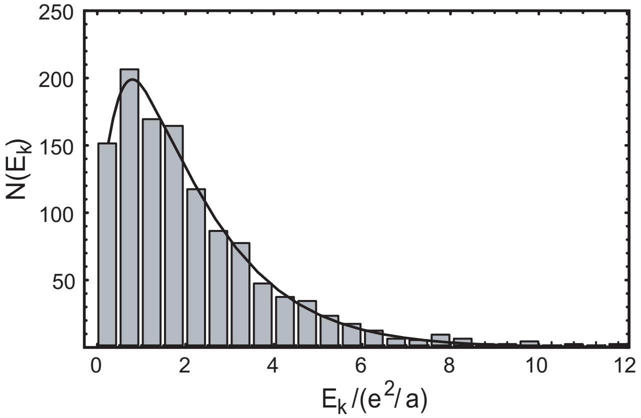

Figure 2.12: Histogram of scaled kinetic energy for unbound electrons and a fit to a Maxwellian.

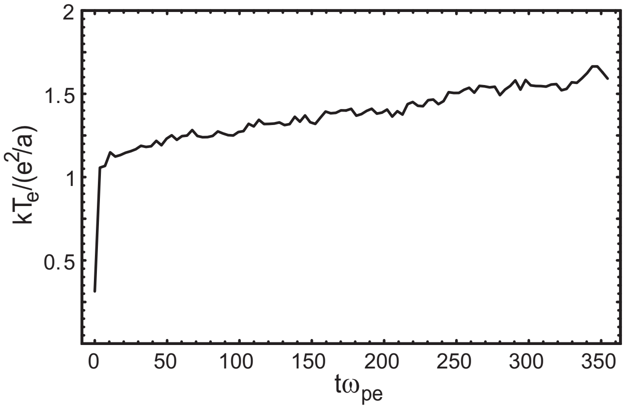

Figure 2.13: Evolution of temperature in the cloud versus time.

bound electrons were nearly in thermal equilibrium. Figure 2.12 shows a histogram of scaled kinetic energy for unbound electrons and a fit to a Maxwellian. The fit determines the temperature of the unbound electrons at a particular time. Figure 2.13 shows the evolution of the temperature versus time. The gradual heating due to three-body recombination is apparent.

Figure 2.14 shows sample energy cascades to deeper binding. Each curve is a plot of scaled binding energy versus scaled time for an ion and bound electron, or sequence of electrons, since collisions can interchange bound and free electrons.

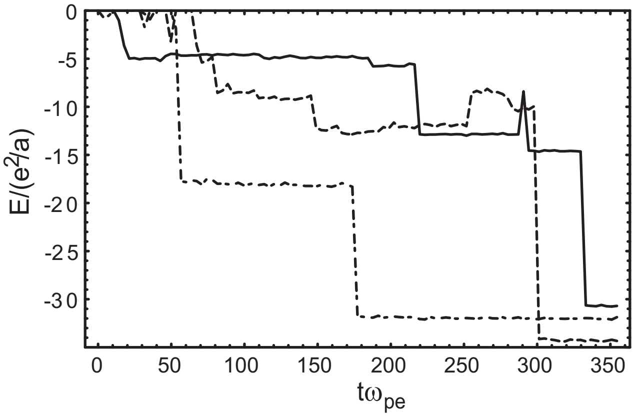

Figure 2.14: Sample energy cascades to deeper binding.

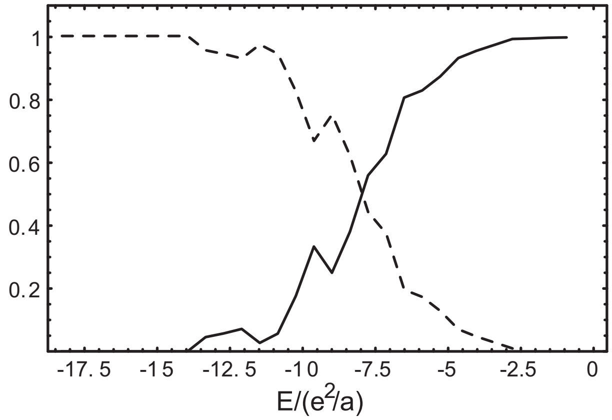

Figure 2.15: The solid curve is the fraction of bound pairs that reached a given binding energy E, and then were reionized. The dashed curve is the fraction that made it from energy E to a sink at $E = -18e^2/a$. These two curves provide evidence for the existence of the bottleneck.

Figure 2.15 provides evidence for the existence of the bottleneck. The solid curve is the fraction of bound pairs that reached a given binding energy, E, and then were reionized. The dashed curve is the fraction that made it from energy E to a sink at $E = -18(e^2/a)$. Each atom that makes it to the sink is declared permanently recombined and is no longer tracked in the cascade dynamics. Taking the crossing point for the curves as the energy of the bottleneck yields $-E_b/(e^2/a) \simeq 8$, which is close to four times the final temperature in Fig. 2.11

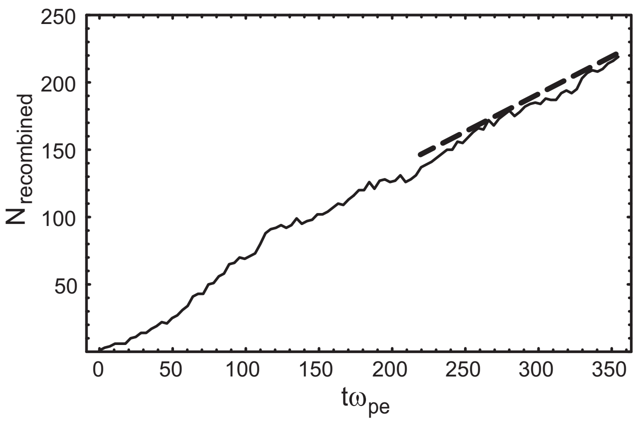

Figure 2.16: Number of recombined pairs in the central region of the cloud.

[i.e., $4T_e/(e^2/a) \simeq 7$].

Figure 2.16 shows the number of recombined pairs in the central region of the cloud (i.e., for $r < r_p$) versus scaled time. Here, $r_p = \sqrt{2/3}\,\langle r^2\rangle^{1/2}$ is the radius where the density has fallen to $1/e$ of its maximum value. Recall that a pair is defined to be recombined when its binding energy drops below the energy level of the bottleneck, which in accord with Fig. 2.15 we take to be $E_b = -8(e^2/a)$.

The dashed line at the top end of Fig. 2.16 provides a smoothed slope for $N_{\rm rec}(t\omega_{pe})$ at the end of the run. From this slope we obtain the recombination rate for the particles in the central region, $dN_{\rm rec}/dt \simeq (0.56)\omega_{pe}$. For comparison the theoretical prediction from Eq. (2.5) for this rate is

$$\int_0^{r_p} 4\pi r^2\, dr\; n\mathcal{R}(r,T) = (1.09)\omega_{pe}, \tag{2.7}$$

where $n(r)$ is the density of unrecombined ions in the central region and the scaled electron temperature $1/\Gamma_e = kT_e/(e^2/a) = 1.7$ has been used. Presumably, the factor of two difference between the predicted and observed rates is due to the fact that Γ_e is only slightly less than unity.

The solid curve in Fig. 2.17(a) shows the average energy of an electron as it cascades to deeper binding versus the time since initial binding. The average

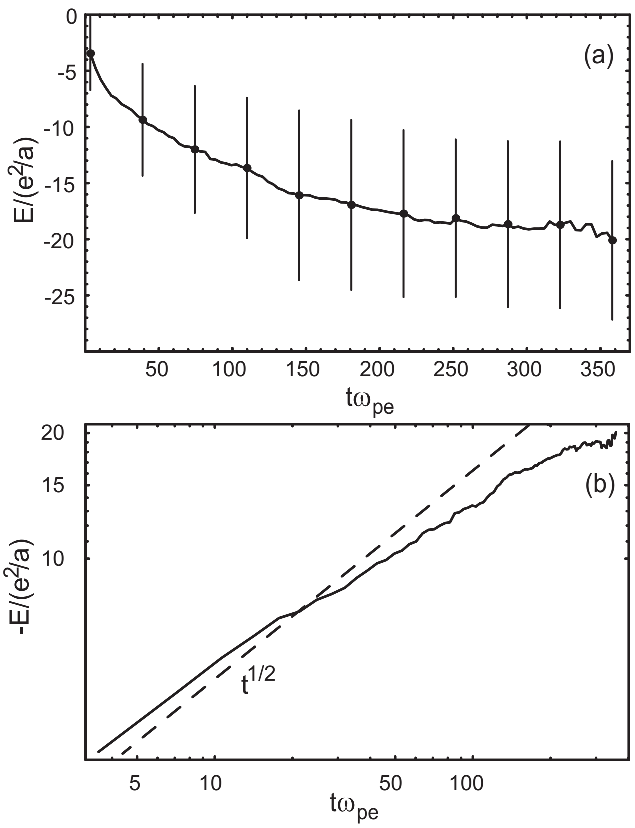

Figure 2.17: (a). Average energy of an electron as it cascades to deeper binding. Error bars show the standard deviation for the distribution. (b) Log-log plot of the average energy.

was constructed using the collection of bound pairs that ultimately reached the sink at $E/(e^2/a) = -12$, and the error bars show the standard deviation for the distribution. Figure 2.17(b) is a log-log plot of the curve, showing that the average binding energy increased like $t^{1/2}$.

This result is easy to understand physically. Consider an electron-ion pair bound with energy $|E| \gg kT_e$. Typically the kinetic energy and the potential energy of the electron are of order $|E|$, and the separation between the electron and ion is of order $d \sim e^2/|E|$. The frequency at which other electrons approach the pair within distance d is of order $\nu \sim n\bar{\mathrm{v}}_e d^2$. In such a collision the two electrons typically share their kinetic energy. One electron leaves the collision with kinetic energy of order $|E| \gg kT_e$, and the binding energy of the remaining electron increases by order $|E|$. Thus, the rate of increase in the binding energy is approximately

$$\frac{d|E|}{dt} \sim \nu|E| = n\bar{\mathrm{v}}_e\pi\frac{e^4}{|E|}. \tag{2.8}$$

To the extent that $n\bar{\mathrm{v}}_e$ is approximately constant, we find that the binding energy increases with time as

$$|E| \sim [C + n\bar{\mathrm{v}}_e\pi e^4 t/2]^{1/2}, \tag{2.9}$$

which agrees with the $t^{1/2}$ scaling in Fig. 2.17(b).

These ideas shed light on a recent experimental observation made with the ultracold plasma clouds [3]. The number of recombined pairs was observed to be a decreasing function of principle quantum number. Equivalently, the distribution over the magnitude of the binding energy, $N(|E|)$, was observed to be increasing in $|E|$ over a certain range below the bottleneck. For the histograms shown in Fig. 2.11 this is not the case. However, we believe that $dN/d|E|$ would become positive over some range if the simulations were run longer.

The reason is easy to understand physically. In steady state, the flux of bound pairs through any energy $|E|$ must be independent of $|E|$, so we obtain the equation

$$N(|E|)\frac{d|E|}{dt}(|E|) = \text{const}. \tag{2.10}$$

Since $d|E|/dt \propto 1/|E|$ decreases with increasing $|E|$, $N(|E|)$ must increase.

This chapter has been published in Physics of Plasmas **9**, 3743-3751 (2002), S.G. Kuzmin, T.M. O'Neil. S.G. Kuzmin was the primary investigator and author of this paper.

Chapter 3

Guiding Center Drift Atoms

3.1 Abstract

Very weakly bound electron-ion pairs in a strong magnetic field are called guiding center drift atoms, since the electron dynamics can be treated by guiding center drift theory. Over a wide range of weak binding, the coupled electron-ion dynamics for these systems is integrable. This paper discusses the dynamics, including the important cross magnetic field motion of an atom as a whole, in terms of the system constants of the motion. Since the dynamics is quasi-classical quantum numbers are assigned using the Bohr-Sommerfeld rules. Antimatter versions of these guiding center drift atoms likely have been produced in recent experiments.

3.2 Introduction

This paper discusses the motion of a quasi-classical, weakly bound electron-ion pair in a strong magnetic field. The field is sufficiently strong that the electron cyclotron frequency is the largest of the dynamical frequencies and the cyclotron radius is the smallest of the length scales. In this limit, the rapid cyclotron motion can be averaged out, and the electron dynamics treated with guiding center drift theory. These weakly bound and strongly magnetized pairs are called guiding

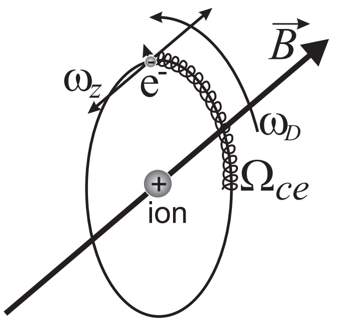

Figure 3.1: Drawing of guiding center atom. In order of descending frequency, electron executes cyclotron motion, oscillates back and forth along a field line in the Coulomb well of the ion, $\vec{E} \times \vec{B}$ drifts around the ion.

center drift atoms [24].

Figure 3.1 shows a picture of the motion in a simple limit. The guiding center electron oscillates back and forth along the magnetic field in the Coulomb well of the ion, and more slowly $\vec{E} \times \vec{B}$ drifts around the ion. Let $z = z_e - z_i$ be the separation of the electron and ion along the direction of the magnetic field and $r = \sqrt{(x_e - x_i)^2 + (y_e - y_i)^2}$ the separation transverse to the field. For the case where the amplitude of the field aligned oscillations is not too large (i.e., $z_{max} \lesssim r$), the frequency of field aligned oscillations is approximately $\omega_z = \sqrt{e^2/(m_e r^3)}$ and the frequency of the $\vec{E} \times \vec{B}$ drift rotation is approximately $\omega_D = v_D/r = ce/(Br^3)$. These two frequencies are related to the electron cyclotron frequency, $\Omega_{ce} = eB/m_e c$ through the equation $\Omega_{ce} = \omega_z^2/\omega_D$. Thus, the requirement that the cyclotron frequency be larger than the other two frequencies imposes the ordering:

$$\Omega_{ce} \gg \omega_z \gg \omega_D. \tag{3.1}$$

The ordering is realized for sufficiently large separation (weak binding), that is, for $r \gg r_1 = (m_e c^2/B^2)^{1/3}$. This inequality is required for validity of our analysis.

Note that the the inequality implies not only that that the electron cyclotron frequency is large, but also that the electron cyclotron radius is small. We have in mind cases where the electron kinetic energy is smaller than or of order the electrostatic binding energy (i.e., $m_e v_e^2/2 \lesssim e^2/r$). The inequality $r \gg r_1$ then implies that $r_{ce} \equiv v_e/\Omega_{ce} \ll r$.

For r comparable to r_1 our guiding center analysis fails. All three frequencies in Eq. (3.1) are comparable, and the electron motion is chaotic [35, 36]. For $r \ll r_1$, the cyclotron frequency is small compared to the Kepler frequency, and the electron motion is again integrable. In this case, one can think of the weakly bound pair as a high-n Rydberg atom with a Zeeman perturbation [37].

The type of motion shown in Fig. 3.1, where the electron $\vec{E}\times\vec{B}$ drifts around the ion, occurs when $\omega_D > \Omega_{ci}$, v_i/r. Here, Ω_{ci} is the ion cyclotron frequency and v_i is the initial velocity of the ion transverse to the magnetic field. For this type of motion, the pair drifts across magnetic field with the transverse ion velocity $\vec{v}_i$ much like a neutral atom.

However, if the ion velocity is too large (i.e. $v_i/r \gg \omega_D$), the $\vec{E}\times\vec{B}$ drifting electron cannot keep up with the ion. The ion runs off and leaves the electron, which is effectively pinned to the magnetic field. More precisely, the ion moves in a large cyclotron orbit near the electron, the cyclotron motion being modified by electrostatic attraction to the electron. Of course, the electron oscillations back and forth along the magnetic field can become unbounded during large transverse excursions.

Figure 3.2 shows a kind of motion that can occur for relatively weak binding (i.e., $\Omega_{ci} > \omega_D$, or $r > r_2 = (m_i/m_e)^{1/3} r_1$). The electron $\vec{E}\times\vec{B}$ drifts in the field of the ion, and the ion $\vec{E}\times\vec{B}$ drifts in the field of the electron. Together they form a so called ”drifting pair”. In a drifting pair, the electron and ion move together across the magnetic field with the speed $v_D = ce/Br^2$.

The main purpose of this paper is to determine the character of the cou-

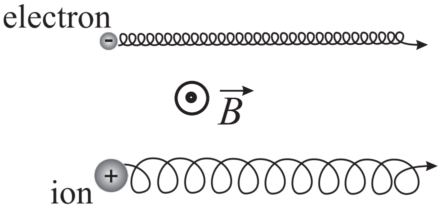

Figure 3.2: A kind of motion that occurs when electron and ion form a drifting pair.

pled electron-ion motion as a function of the constants of the motion. Fortunately, the Hamiltonian dynamics for the coupled system is integrable over a wide range of weak binding. The electron-ion system has six degrees of freedom so six constants of the motion are required for integrability. Four are exact constants: the Hamiltonian and the three components of total momentum. The remaining two are approximate constants (adiabatic invariants) that result from two frequency separations. Because the electron cyclotron frequency is much larger than other dynamical frequencies the cyclotron action is a good adiabatic invariant. Use of guiding center drift variables automatically takes this constant into account and removes the cyclotron motion from the problem. Because the frequency of field aligned oscillations, ω_z, is much larger than the remaining dynamical frequencies (associated with cross field motion) the action associated with the field aligned motion is a good adiabatic invariant.

Inequality (3.1), which follows from the weak binding condition $r \gg r_1 = (m_e c^2/B^2)^{1/3}$, guarantees that the characteristic electron frequencies are ordered in accord with the assumed frequency separations. The frequencies that characterize the cross field ion motion (i.e., Ω_{ci} and v_i/r) also must be small compared to ω_z. The full frequency ordering is then

$$\Omega_{ce} \gg \omega_z \gg \omega_D, \Omega_{ci}, v_i/r. \tag{3.2}$$

The relative size of ω_D, Ω_{ci} and v_i/r need not be specified; indeed, it is interplay between these frequencies that gives rise to the different types of motion discussed above. We will return to a detailed discussion of the frequency ordering later (see Section 3.5).

The analysis is carried out in a reference frame where the electric field vanishes. However, the effect of a uniform electric field directed transverse to the magnetic field can be included simply by shifting the transverse ion velocity (i.e., $\vec{v}_i(0) \longrightarrow \vec{v}_i(0) - c\vec{E} \times \vec{B}/B^2$).

Antimatter versions of these guiding center drift atoms have likely been realized in recent experiments at the European Organization for Nuclear Research (CERN). The ATHENA [21] and ATRAP [22] collaborations have both reported success in producing cold antihydrogen atoms. The ATRAP collaboration measured binding energies of order meV, which corresponds to $\bar{e} - \bar{p}$ separation of order 10^{-4} cm [23]. The magnetic field strength is 5 Tesla, so the critical radius is $r_1 \equiv (m_e c^2/B^2)^{1/3} = 7 \times 10^{-6}$ cm. Thus, the separation is much larger than r_1, and the weakly bound pairs are guiding center atoms. The cyclotron frequency for the positron is about 100 times larger than the $\vec{E} \times \vec{B}$ drift frequency ω_D, and the cyclotron radius is about 100 times smaller than the separation. The ATHENA group did not measure binding energies, but the theory of three-body recombination, expected to be the dominant recombination process, suggests binding energies in the same range as those for ATRAP.

There has been much previous work on the coupled electron-ion system in a strong magnetic field. A difficulty is that a true separation of the center of mass motion (transverse to the magnetic field) and the internal motion is not possible. However, Avron, Herbst, and Simon [26] found an effective separation by introducing the transverse pseudomomentum and showing that it is a constant of motion. The influence of the transverse center of mass motion on the internal motion in then accounted for by a pseudopotential that depends on the eigenvalue of the pseudomomentum. More recently this effective separation was applied to the hydrogen atom [27] and positronium [28].

In our classical analysis, the transverse pseudomomenta (P_X, P_Y) arise as two new momenta in a canonical transformation, and the pseudopotential enters the transformed Hamiltonian. Our analysis differs from the previous work in that the Hamiltonian is simplified by the use of frequency ordering (3.2), which relies on both strong magnetic field and weak binding. Introduction of the cyclotron action and of the action for the field aligned bounce motion effectively averages the Hamiltonian over the rapid cyclotron and bounce motions, removing two degrees of freedom at the outset. In the language of atomic physics, a double Born-Oppenheimer approximation is used. The remaining transverse dynamics is always integrable, and a transverse action can be introduced. Since the Hamiltonian is expressed as a function of the cyclotron action, bounce action, and transverse action, a general expression for the quantum energy levels can be obtained using the Bohr-Sommerfeld quantization rules. Of course the assumption of weak binding justifies the quasi-classical approximation – with the possible exception of the cyclotron motion, as will be discussed. We will compare general quasi-classical predictions for energy levels to predictions from quantum calculations in limiting cases.

Much of the previous work has focused on an “outer well” that exists in the pseudopotential for sufficiently large pseudomomentum and the consequent “delocalized atomic states [26, 27]”. From the prospective of guiding center drift theory, these delocalized states are simply an electron and ion $\vec{E} \times \vec{B}$ drifting in each other’s field as shown in Fig. 3.2. The criterion for the existence of the outer well in the exact pseudopotential is that the scaled pseudomomentum be larger than a certain value, $\widetilde{P} \geq \widetilde{P}_c = 3/4^{1/3}$ [27]. The reader may wish to skip ahead to Eq. (3.18) for the definition of $\widetilde{P}$. This is a necessary criterion for the existence of the delocalized states. Working with the bounce averaged pseudopotential, we find a necessary and sufficient criterion for the delocalized states, $\widetilde{P} > \widetilde{P}(\widetilde{I}_z)$, where $\widetilde{I}_z$ is the scaled bounce action. As we will see, $\widetilde{P}_c(\widetilde{I}_z)$ reduces to $\widetilde{P}_c = 3/4^{1/3}$ for $\widetilde{I}_z = 0$.

The name "guiding center drift atom" was coined in Ref. [24]. Indeed, a version of Fig. 3.1 appears in Ref. [24]. Likewise, the possibility of "$\vec{E} \times \vec{B}$ drifting pairs" and "runaway ions" was discussed. However, Ref. [24] did not exploit the integrability of the Hamiltonian to discuss the atom dynamics as a function of the constants of the motion, which is the principle focus of this paper. Rather, anticipating the programs to produce antihydrogen [21, 22], Ref. [24] extended the theory of three-body recombination to the case of guiding center drift atoms. The theory treated the simple case where the ion (or antiproton) is stationary. The general characterization of atom dynamics developed here is a prerequisite to an analysis of three-body recombination that takes into account ion motion.

3.3 Hamiltonian and Constants of Motion

We consider a uniform magnetic field $\vec{B} = \hat{z}B$ represented by the vector potential $\vec{A} = Bx\hat{y}$. The external electric field is chosen to be zero. The Hamiltonian for a guiding center drift electron and an ion that interact electrostatically and move in the magnetic field is given by

$$H = I_{ce}\Omega_{ce} + \frac{1}{2m_e}p_{ze}^2 + \frac{1}{2m_i}p_{xi}^2 + \frac{1}{2m_i}\left(p_{yi}^2 - \frac{e}{c}Bx_i\right)^2 + \frac{1}{2m_i}p_{zi}^2 - \frac{e^2}{\sqrt{\left(x_i + \frac{c}{eB}p_{ye}\right)^2 + (y_i - y_e)^2 + (z_i - z_e)^2}}. \quad (3.3)$$

Here, the first two terms are the electron kinetic energy, where Ω_{ce} is the cyclotron frequency and I_{ce} is the cyclotron action. The product is the kinetic energy associated with velocity components transverse to the magnetic field. Since I_{ce} is a good adiabatic invariant and Ω_{ce} is constant (for a uniform magnetic field), the product $I_{ce}\Omega_{ce}$ is constant and does not influence the dynamics of the remaining variables. The quantities x_i, y_i, z_i, y_e and z_e are ion and electron coordinates; and the momenta conjugate to these coordinates are given by

$$\begin{aligned}
p_{xi} &= m_i\dot{x}_i,\\
p_{yi} &= m_i\dot{y}_i + \frac{eB}{c}x_i,\\
p_{zi} &= m_i\dot{z}_i,\\
p_{ye} &= -\frac{eB}{c}x_e,\\
p_{ze} &= m_e\dot{z}_e.
\end{aligned} \tag{3.4}$$

The electron position transverse to the field is specified by $(y_e, p_{ye} = -eBx_e/c)$, and $x_e, p_{xe} = m_e\dot{x}_e$ are removed from the dynamics. The removal of one degree of freedom results from averaging out the rapid cyclotron motion.

Let us make a canonical transformation to a new set of variables

$$\begin{aligned}
P_X &= p_{xi} + \frac{eB}{c}(y_e - y_i), & X &= \frac{c}{eB}(p_{yi} + p_{ye}) + x_i,\\
P_Y &= p_{yi} + p_{ye}, & Y &= \frac{c}{eB}p_{xi} + y_e,\\
P_Z &= p_{zi} + p_{ze}, & Z &= \frac{m_i z_i + m_e z_e}{m_i + m_e},\\
p_y &= \frac{eB}{c}x_i + p_{ye}, & y &= y_e - y_i,\\
p_z &= \frac{m_i p_{ze} - m_e p_{zi}}{m_i + m_e}, & z &= z_e - z_i.
\end{aligned} \tag{3.5}$$

To verify that the transformation is canonical, one can check that Poisson brackets are equal to unity for conjugate variables and vanish otherwise. The Hamiltonian in the new variables has the form

$$H = I_{ce}\Omega_{ce} + \frac{1}{2m_i}\left(P_X - \frac{eB}{c}y\right)^2 + \frac{1}{2m_i}\left(P_Y - p_y\right)^2 + \frac{1}{2M}P_Z^2 + \frac{1}{2\mu}p_z^2 - \frac{e^2}{\sqrt{\left(\frac{c}{eB}p_y\right)^2 + y^2 + z^2}}, \quad (3.6)$$

where $M = m_i + m_e$, and $\mu = m_i m_e/(m_i + m_e)$ are total and reduced mass, respectively. Since the mass ratio is assumed to be small ($m_e/mi \ll 1$), we set $M \simeq m_i$ and $\mu \simeq m_e$ in the subsequent analysis. The Hamiltonian is independent of t, X, Y, and Z, so H, P_X, P_Y and P_Z are constants of the motion. We work in a frame where P_Z is zero (the the center of mass frame), and we orient the coordinates axis so that P_X is zero. This involves no loss of generality. In the Hamiltonian, the sum of the two terms that govern the z-motion are the binding energy

$$H_z = \frac{1}{2\mu}p_z^2 - \frac{e^2}{\sqrt{r^2 + z^2}}, \quad (3.7)$$

where

$$\vec{r} = \left(-\frac{c}{eB}p_y,\ y,\ 0\right) \equiv \left(x_e - x_i,\ y_e - y_i,\ 0\right). \quad (3.8)$$

The electron kinetic energy associated with velocity components transverse to the magnetic field is bound up in the cyclotron action, I_{ce}. For a bound electron-ion pair, H_z is negative.

In previous work [26, 27, 28] the momentum $\vec{P} = (P_X, P_Y)$ is called the pseudomomentum. Likewise, the second two terms in Hamiltonian (3.6), which are the transverse kinetic energy of the ion, are thought of as a pseudopotential for the transverse internal motion [i.e., for (y, p_y)].

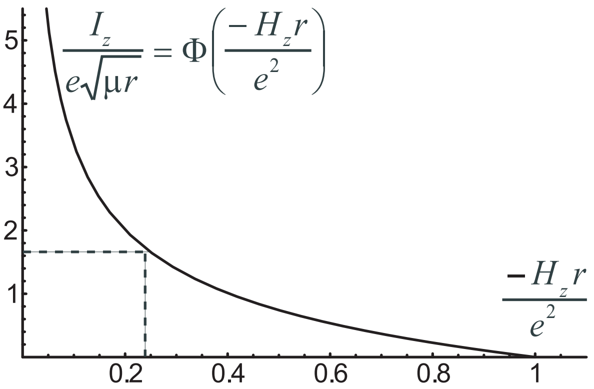

Figure 3.3: Graphical solution of equation (3.9). Knowing I_z and r, one can find $H_z(r, I_z)$.

One further constant is required for integrability, and it is given by the bounce action for the z-motion,

$$I_z = \frac{1}{2\pi} \oint p_z dz = e\sqrt{\mu r}\ \Phi\left(\frac{-H_z r}{e^2}\right), \tag{3.9}$$

which is a good adiabatic invariant for sufficiently large bounce frequency. In carrying out the integral, H_z and r are held constant. The function $\Phi(\xi)$ is given by

$$\Phi(\xi) = \frac{2\sqrt{2}}{\pi\sqrt{\xi}} \int_{\xi}^{1} \sqrt{\frac{q - q^2}{q^2 - \xi^2}}\, dq = \frac{2\sqrt{2}}{\pi\xi\sqrt{1+\xi}} \left[-\xi(\xi+1)E\left(\frac{\xi-1}{\xi+1}\right) + \right.$$

$$\left. \xi K\left(\frac{\xi-1}{\xi+1}\right) + \Pi\left(\frac{\xi-1}{\xi}, \frac{\xi-1}{\xi+1}\right)\right]. \tag{3.10}$$

where E, K, and Π are the complete elliptic integrals and the argument of Φ is $\xi = -H_z r/e^2$. For future reference we note that $\xi = r/\sqrt{z_{max}^2 + r^2}$, where z_{max} is the amplitude of the field aligned oscillations. Figure 3.3 shows a plot of $\Phi(\xi)$ on the interval $[0, 1]$. The figure also shows a graphical inversion to obtain H_z as a function of I_z and r. Formally, we write the inversion as

$$H_z(r, I_z) = -\frac{e^2}{r}\Phi^{-1}\left(\frac{I_z}{e\sqrt{m_e r}}\right). \tag{3.11}$$

When $\xi = -H_z r/e^2$ is close to 1, the amplitude of axial electron oscillations in the Coulomb well is small compared to r, and the potential is approximately harmonic. In this case $\Phi(\xi)$ can be approximated by linear dependence:

$$\Phi(\xi) \simeq 1 - \xi, \tag{3.12}$$

and H_z and I_z are related as

$$H_z(r, I_z) \simeq -\frac{e^2}{r} + I_z\omega_z, \tag{3.13}$$

where $\omega_z^2 = e^2/(\mu r^3)$. As one expects, the Coulomb potential energy, $-e^2/r$, is corrected by the addition of a small term $I_z\omega_z$, the oscillation energy in a harmonic well.

Analytic treatment also is possible when the amplitude of oscillation is near the limit allowed by binding, (i.e., $\xi = -H_z r/e^2 \ll 1$). One can approximate the function $\Phi(\xi)$ with an asymptotic series

$$\Phi(\xi) \simeq \sqrt{\frac{2}{\xi}} - \frac{4\sqrt{2}}{\pi}[E(-1) - K(-1)] - \dots \tag{3.14}$$

Using the first two terms in this series yields the approximate expression

$$H_z(r, I_z) \simeq -\frac{2\mu e^4}{\left(I_z + \frac{4}{\pi}[E(-1) - K(-1)]e\sqrt{2\mu r}\right)^2}\,. \tag{3.15}$$

We can see from (3.15) that for finite bounce oscillations ($I_z \neq 0$), the electron binding energy H_z has the minimum possible value $H_z = -2\mu e^4/I_z^2$. If the electron-ion transverse separation were slowly reduced, the binding energy would not go to minus infinity. Note that expression (3.15) is only valid for I_z such that $I_z \gg e\sqrt{\mu r}$.

Substituting Eqs. (3.7) and (3.11) plus the choices $P_X = P_Z = 0$ into Hamiltonian (3.6) yields an implicit equation for the phase space trajectory (i.e., for $p_y(y)$)

$$H = I_{ce}\Omega_{ce} + \frac{1}{2}m_i\Omega_{ci}y^2 + \frac{1}{2m_i}\left(P_Y - p_y\right)^2 - \frac{e^2}{r}\Phi^{-1}\left(\frac{I_z}{e\sqrt{m_e r}}\right), \tag{3.16}$$

where r is related to y and p_y through Eq. (3.8). The trajectory is specified by the values of H, P and I_z. With the additional input of an initial point along the trajectory (e.g., $y(t=0)$ or $p_y(t=0)$), the Hamiltonian equations of motion can be solved to find $y(t)$ and $p_y(t)$. Given this solution, the coordinates of the electron and ion are determined separately by the equations

$$\begin{aligned} \frac{dx_i}{dt} &= -\frac{eB}{m_i c} y(t), \qquad \frac{dy_i}{dt} = \frac{P_Y}{m_i} - \frac{p_y(t)}{m_i}, \\ \frac{dp_{ye}}{dt} &= -\frac{\partial H_z(r, I_z)}{\partial y}, \quad \frac{dy_e}{dt} = \frac{\partial H_z(r, I_z)}{\partial p_y}. \end{aligned} \tag{3.17}$$

These equations follow from Eqs. (3.4) and (3.5) and the choice $P_X = 0$.

3.4 Phase Trajectories in Scaled Variables

The dependence of the phase trajectories on parameters such as e and B can be buried in scaled variables. Using $r_2 = (m_i c^2/B^2)^{1/3} = (m_i/m_e)^{1/3} r_1$, Ω_{ci}^{-1} and m_i as the units of length, time and mass yields the scaled variables

$$\begin{aligned} \widetilde{P} &= P_Y/(m_i \Omega_{ci} r_2), \\ \tilde{y} &= y/r_2, \\ \tilde{p}_y &= p_y/(m_i \Omega_{ci} r_2), \\ \widetilde{H} &= H/(m_i \Omega_{ci}^2 r_2^2), \\ \widetilde{H}_z &= H_z/(m_i \Omega_{ci}^2 r_2^2), \\ \widetilde{I}_z &= I_z/(m_i \Omega_{ci} r_2^2), \\ \widetilde{I}_{ce} &= I_{ce}/(m_i \Omega_{ci} r_2^2), \end{aligned} \tag{3.18}$$

and the scaled Hamiltonian

$$\widetilde{H} = \frac{m_i}{m_e} \widetilde{I}_{ce} + \frac{1}{2}\left(\widetilde{P} - \tilde{p}_y\right)^2 + \frac{1}{2}\tilde{y}^2 - \frac{1}{\tilde{r}} \Phi^{-1}\left(\sqrt{\frac{m_i}{m_e}} \frac{\widetilde{I}_z}{\sqrt{\tilde{r}}}\right), \tag{3.19}$$

where the $\tilde{r} = \tilde{x}^2 + \tilde{y}^2$ and $\tilde{x} = -\tilde{p}_y$. Likewise, Eqs. (3.17) take the scaled form

$$\begin{aligned} \frac{d\tilde{x}_i}{d\tilde{t}} &= -\tilde{y}(\tilde{t}), \quad \frac{d\tilde{y}_i}{d\tilde{t}} = \widetilde{P} - \tilde{p}_y(\tilde{t}), \\ \frac{d\tilde{p}_{ye}}{d\tilde{t}} &= -\frac{\partial \widetilde{H}_z}{\partial \tilde{y}}, \quad \frac{d\tilde{y}_e}{d\tilde{t}} = \frac{\partial \widetilde{H}_z}{\partial \tilde{p}_y}, \end{aligned} \tag{3.20}$$

where $\widetilde{H}_z$ is the last term in Hamiltonian (3.19) and the scaled time is $\tilde{t} = t\Omega_{ci}$.

We have in mind cases where the scaled variables $\widetilde{P}$, $\tilde{y}$ and $\tilde{p}_y = -\tilde{x}$ are all of order unity, but $\widetilde{I}_z$ is of order $\sqrt{m_e/m_i}$. The product $\sqrt{m_e/m_i}\widetilde{I}_z$, which enters the last term is then of order unity. In the following discussion of trajectories we will specify the value of the product $\sqrt{m_i/m_e}\widetilde{I}_z$. The significance of the factor $\sqrt{m_i/m_e}$ will be apparent in the next section where we evaluate frequencies as derivatives of $\widetilde{H}$ with respect to actions.

For the simple case $\sqrt{m_i/m_e}\widetilde{I}_z = 0$, Hamiltonian (3.19) reduces to the form

$$\widetilde{H} = \frac{1}{2}\left(\widetilde{P} - \tilde{p}_y\right)^2 + \frac{1}{2}\tilde{y}^2 - \frac{1}{\sqrt{\tilde{p}_y^2 + \tilde{y}^2}}, \tag{3.21}$$

where the constant term $(m_i/m_e)\widetilde{I}_{ce}$ has been dropped. Phase trajectories in this case depend only on two parameters, $\widetilde{H}$ and $\widetilde{P}$. Depending on the value of $\widetilde{P}$ there can be different types of phase portraits. Three different cases are presented in Figs. 3.4-3.6.

Figure 3.4a shows the phase trajectories for the case where $\widetilde{P} = 2.5$ is greater than a certain critical value, $\widetilde{P}_c = 3/4^{1/3}$. Fig 3.4b shows a plot of $\widetilde{H}(\tilde{y} = 0, \tilde{p}_y, \widetilde{P})$. One can see that $\widetilde{H}$ has two minima, one at $(\tilde{y}, \tilde{p}_y) = (0, 0)$ (where $\widetilde{H} \longrightarrow -\infty$), and another at $\tilde{y} = 0$ and finite $\tilde{p}_y$.

There are three classes of trajectories divided by the separatrix shown as the dashed curve in Fig. 3.4a. For the first class, the trajectories encircle the minimum at $(\tilde{y}, \tilde{p}_y) = (0, 0)$. For the second class, the trajectories encircle the minimum at $\tilde{y} = 0$ and finite $\tilde{p}_y$. For the third class, the trajectories encircle both

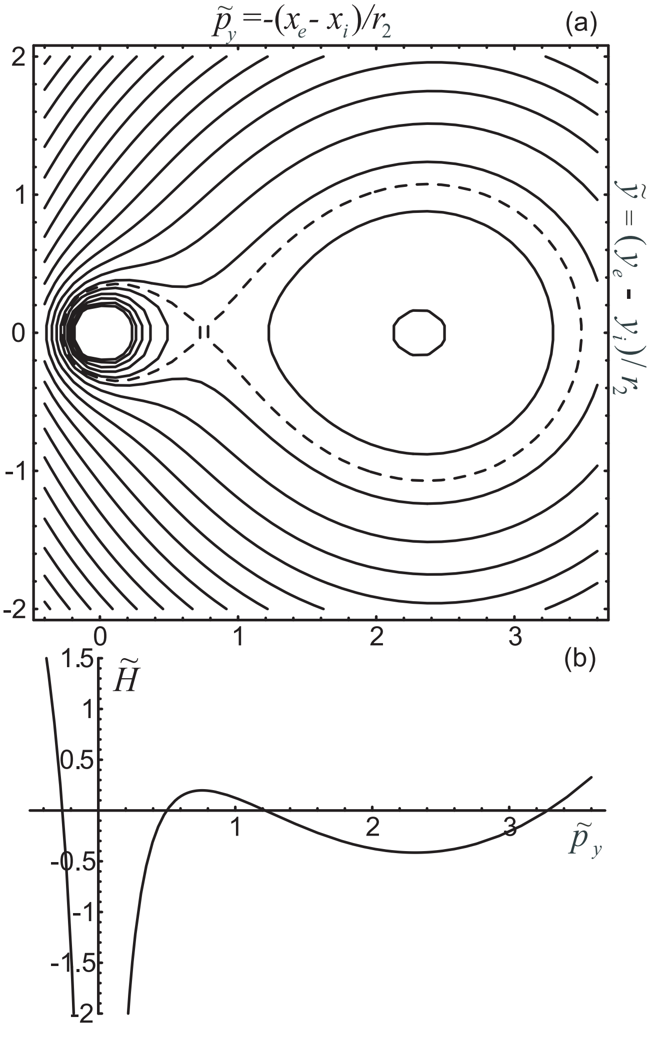

Figure 3.4: (a) — Phase trajectories for the case when $\tilde I_z = 0$, $\tilde P = 2.5 > \widetilde P_c$; (b) — section of $\widetilde H(\tilde p_y, \tilde y, \widetilde P)$ over the plane $\tilde y = 0$.

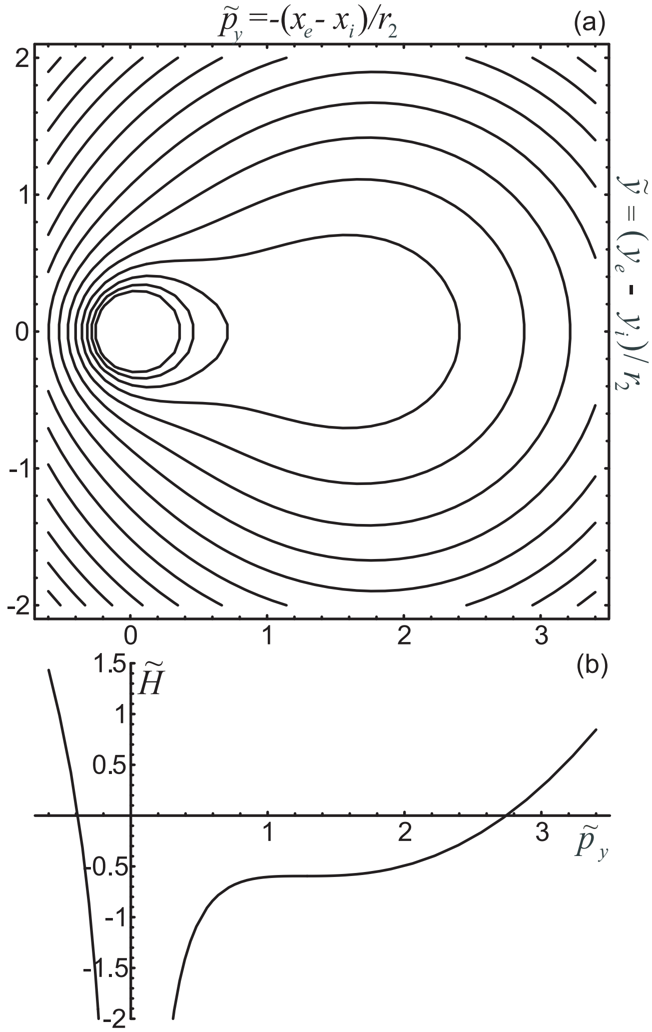

Figure 3.5: Same as on Fig. 3.4 but $\widetilde{P} = 3/4^{1/3} = \widetilde{P}_c$.

minima. We will now describe the prototypical motion for each class in an extreme limit where the motion is simple. Of course, for a trajectory not near one of these limits, say, a trajectory near the separatrix dividing two classes, the motion is a complicated mix of the two limits.

For the trajectories that encircling the minimum at $(\tilde{y}, \tilde{p}_y) = (0, 0)$ with small $\tilde{r} = \sqrt{\tilde{y}^2 + \tilde{p}_y^2}$, the electron $\vec{E} \times \vec{B}$ drifts around the ion as shown in Fig. 3.1. This kind of motion requires the electron $\vec{E} \times \vec{B}$ drift velocity to be large compared

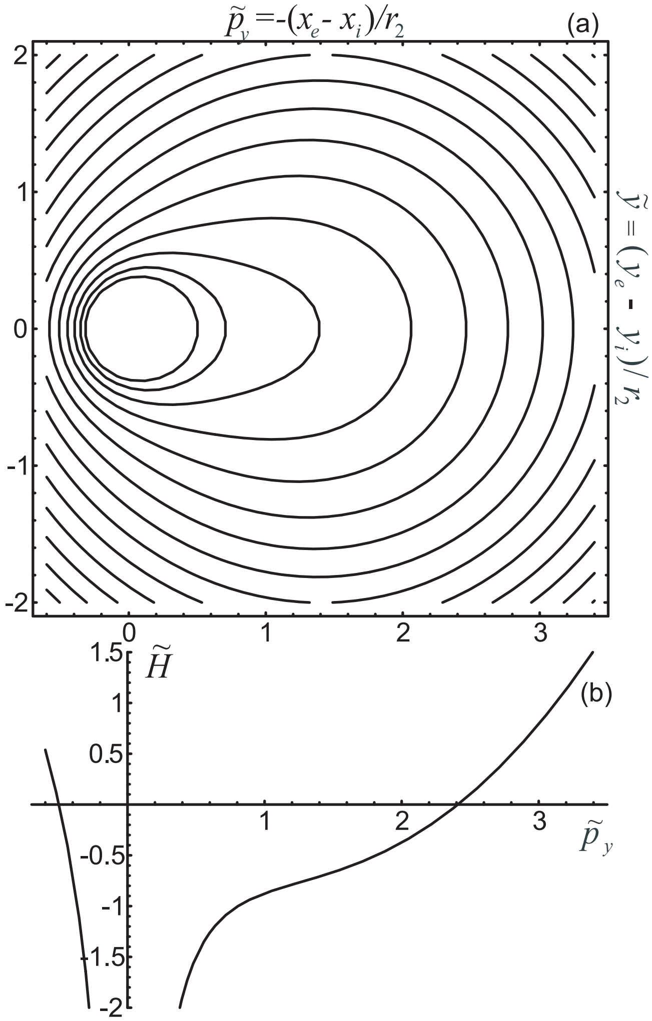

Figure 3.6: Same as on Fig. 3.4 but $\widetilde{P} = 1.5 < \widetilde{P}_c$.

to the ion velocity. From Eqs. (3.20), we see that for $\tilde{r} \ll 1$ and $\widetilde{P}$ order unity or larger, the ion velocity is approximately $\tilde{v}_i \equiv \sqrt{(d\tilde{x}_i/d\tilde{t})^2 + (d\tilde{y}_i/d\tilde{t})^2} \simeq \widetilde{P}$ and the velocity $\tilde{v}_e \equiv \sqrt{(d\tilde{y}_e/d\tilde{t})^2 + (d\tilde{p}_{ye}/d\tilde{t})^2} \simeq 1/\tilde{r}^2$. Thus, the ratio

$$\frac{\tilde{v}_i}{\tilde{v}_e} \simeq \widetilde{P}\tilde{r}^2 \tag{3.22}$$

is small for sufficiently small $\tilde{r}$. The bound electron-ion pair moves across the magnetic field with a velocity that is nearly equal to the initial ion velocity

$$\begin{aligned} \left\langle \frac{d\tilde{x}_i}{d\tilde{t}} \right\rangle &= -\langle \tilde{y} \rangle = 0 \\ \left\langle \frac{d\tilde{y}_i}{d\tilde{t}} \right\rangle &= \widetilde{P} - \langle \tilde{p}_y \rangle \simeq \widetilde{P} \simeq \frac{v_{yi}(0)}{r_2 \Omega_{ci}}. \end{aligned} \tag{3.23}$$

Here, the bracket indicates an average over the rapid $\vec{E} \times \vec{B}$ drift motion of the electron.

For the trajectories that encircle the second minimum tightly, the electron and ion $\vec{E} \times \vec{B}$ drift together as shown in Fig. 3.2. According to Eqs. (3.20) the electron and ion velocities are given by

$$\frac{d\tilde{y}_e}{d\tilde{t}} \simeq \frac{\tilde{p}_{ym}}{|\tilde{p}_{ym}|^3}, \qquad \frac{d\tilde{y}_i}{d\tilde{t}} \simeq \widetilde{P} - \tilde{p}_{ym}, \tag{3.24}$$

where $\tilde{p}_{ym}$ is the location of the minimum. Note that $d\tilde{x}_i/d\tilde{t}$ and $d\tilde{p}_{ye}/d\tilde{t}$ are both nearly zero. The minimum is the root of the equation

$$0 = \frac{d\widetilde{H}}{d\tilde{p}_y} = -\left(\widetilde{P} - \tilde{p}_y\right) + \frac{\tilde{p}_y}{|\tilde{p}_y|^3}, \tag{3.25}$$

so the electron and ion velocities are equal, both given by the $\vec{E} \times \vec{B}$ formula.

For the large circular trajectories (i.e., $\tilde{r} \gg 1$), the ion executes a cyclotron orbit in the vicinity of the electron. The electron $\vec{E} \times \vec{B}$ drift velocity is small compared to the ion velocity for these large $\tilde{r}$ trajectories.

If the value of the transverse momentum $\widetilde{P}$ is decreased, the minimum at $\tilde{y} = 0$ and finite $\tilde{p}_y$ disappears. Figures 3.5a and 3.5b show the the trajectories and Hamiltonian for the critical value $\widetilde{P}_c = 3/4^{1/3}$. Figures 3.6a and 3.6b show the same for a sub-critical value, $\widetilde{P} = 1.5 < \widetilde{P}_c$. One can see that $\vec{E} \times \vec{B}$ drifting pairs [see Fig. 3.2] are no longer possible.

For the general case where $\sqrt{m_i/m_e}\widetilde{I}_z \neq 0$, Hamiltonian (3.19) must be

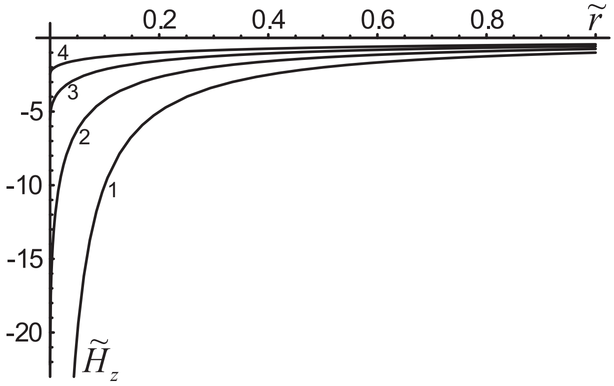

Figure 3.7: Plot of binding energy $\widetilde{H}_z$ at different values of $\sqrt{m_i/m_e}\widetilde{I}_z$. 1: $\sqrt{m_i/m_e}\widetilde{I}_z = 0$ (in this case $\widetilde{H}_z = -1/\tilde{r}$); 2: $\sqrt{m_i/m_e}\widetilde{I}_z = 0.3$; 3: $\sqrt{m_i/m_e}\widetilde{I}_z = 0.6$; 4: $\sqrt{m_i/m_e}\widetilde{I}_z = 0.9$.

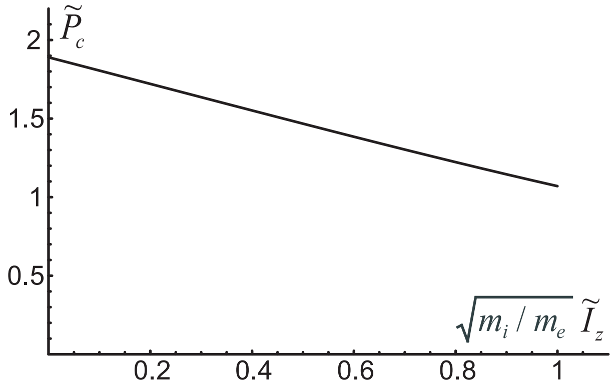

Figure 3.8: Plot of $\widetilde{P}_c(\widetilde{I}_z)$.

used to plot the trajectories. An important difference is that the binding energy

$$\widetilde{H}_z = -\frac{1}{\tilde{r}}\Phi^{-1}\left(\sqrt{\frac{m_i}{m_e}}\frac{\widetilde{I}_z}{\sqrt{\tilde{r}}}\right) \tag{3.26}$$

does not diverge at $\tilde{r} = 0$ when $\sqrt{m_i/m_e}\widetilde{I}_z$ is non-zero. This is to be expected since the potential $-1/\sqrt{\tilde{z}^2 + \tilde{r}^2}$, does not diverge at $\tilde{r} = 0$ for finite $\tilde{z}$. As mentioned earlier [see Eq. (3.15)], $\widetilde{H}_z$ reaches the minimum value $-2/(\sqrt{m_i/m_e}\widetilde{I}_z)^2$ as $\tilde{r}$ approaches zero. Plots of $\widetilde{H}_z$ versus $\tilde{r}$ for various values of $\sqrt{m_i/m_e}\widetilde{I}_z$ are shown in Fig. 3.9.

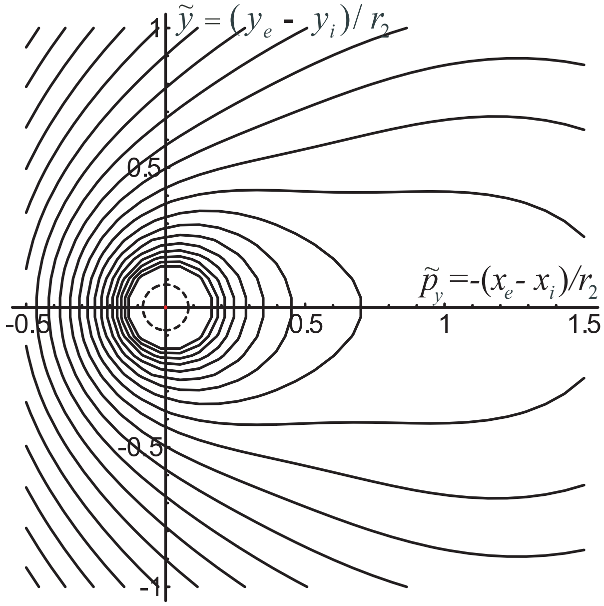

Figure 3.9: Phase portrait of the system for the case when $\widetilde{P} = 1.5$, $\sqrt{m_i/m_e}\widetilde{I}_z = 0.3$; the radius of dashed circle in the center is equal to $\tilde{r}_1 = r_1/r_2$.

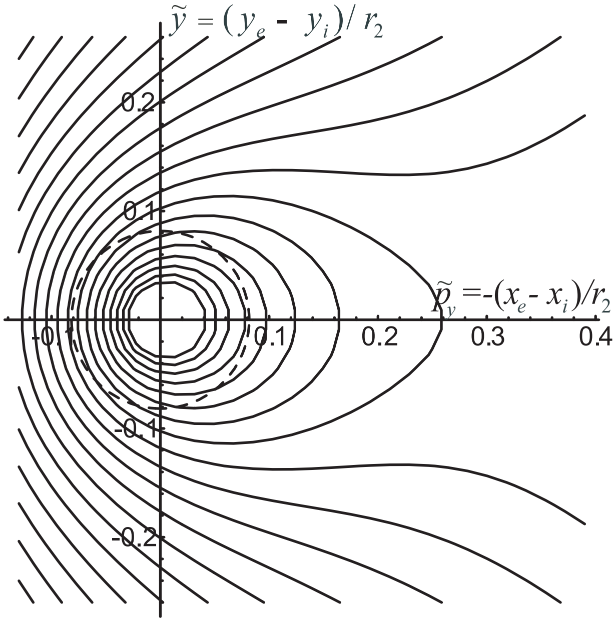

Figure 3.10: Phase portrait of the system for the case when $\widetilde{P} = 1.5$, $\sqrt{m_i/m_e}\widetilde{I}_z = 0.9$; the radius of dashed circle in the center is equal to $\tilde{r}_1$.

The phase trajectories for non-zero $\sqrt{m_i/m_e}\widetilde{I}_z$ are qualitatively like those shown in Figs. 3.4, 3.5, 3.6. However, the critical value of $\widetilde{P}$, signifying the loss of the separatrix, is a slowly decreasing function of $\sqrt{m_i/m_e}\widetilde{I}_z$. Figure 3.8 shows a plot of $\widetilde{P}_c(\sqrt{m_i/m_e}\widetilde{I}_z)$ for $\sqrt{m_i/m_e}\widetilde{I}_z$ ranging from 0 to 1. As illustrations, Figs. 3.9 and 3.10 show phase space trajectories for the same values of $\widetilde{P}$ [i.e., $\widetilde{P} = 1.5$] but for different values of $\sqrt{m_i/m_e}\widetilde{I}_z$ (i.e., $\sqrt{m_i/m_e}\widetilde{I}_z = 0.3$ and $\sqrt{m_i/m_e}\widetilde{I}_z = 0.9$). In Fig. 3.9 there is no separatrix, since $\widetilde{P} = 1.5$ is below the critical value $\widetilde{P}_c(\sqrt{m_i/m_e}\widetilde{I}_z = 0.3) \simeq 1.64$; whereas, in Fig. 3.10 there is a separatrix, since $\widetilde{P} = 1.5$ is above the critical value $\widetilde{P}_c(\sqrt{m_i/m_e}\widetilde{I}_z = 0.9) \simeq 1.15$.

3.5 Frequency Separation and the Adiabatic Invariants

In this section, we examine the frequency separation required for validity of the adiabatic invariants. For a case where the separation is well satisfied, we will see that a solution of the full equations of motion, including the electron cyclotron motion, compares well to the corresponding trajectory obtained using constancy of the adiabatic invariants. For a case where the separation is not satisfied, the numerical solution of the full equations of motion exhibits breakdown of the adiabatic invariants and apparent chaotic motion.

The frequency separation can be understood as a consequence of the large mass ratio $m_i/m_e \gg 1$. In Hamiltonian (3.19), suppose that the cross field scaled variables are all of order unity [i.e., $\widetilde{P}, \tilde{y}, \tilde{p}_y \sim O(1)$] and that $\sqrt{m_i/m_e}\widetilde{I}_z, (m_i/m_e)\widetilde{I}_c \sim O(1)$. The scale cyclotron frequency is $\partial\widetilde{H}/\partial\widetilde{I}_c = m_i/m_e$, the scaled frequency of field aligned oscillations is $\partial\widetilde{H}/\partial\widetilde{I}_z \sim O(\sqrt{m_i/m_e})$ and the scaled cross field frequencies are of order unity. Thus, the three classes of frequencies in inequality (3.2) are ordered as $m_i/m_e \gg \sqrt{m_i/m_e} \gg 1$.

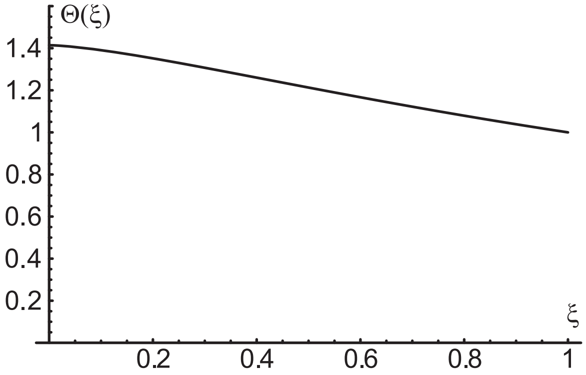

Figure 3.11: Plot of function $\Theta(\xi)$.

Let us look at the field aligned oscillations more closely. For arbitrary $\xi = \tilde{r}/\sqrt{\tilde{r}^2 + \tilde{z}_{max}^2}$, the scaled frequency is given by

$$\frac{\partial \widetilde{H}_z}{\partial \widetilde{I}_z} = \sqrt{\frac{m_i}{m_e}} \frac{1}{\tilde{r}^{3/2}} \frac{1}{-\Phi'(\xi)} = \sqrt{\frac{m_i}{m_e}} \left(\frac{\xi}{\tilde{r}}\right)^{3/2} \Theta(\xi), \tag{3.27}$$

where the function $\Theta(\xi)$ is plotted in Fig. 3.11. Since $\Theta(\xi)$ is unity to within a factor of $\sqrt{2}$ over the full range of ξ-values (i.e., $0 \leq \xi \leq 1$), the scaled frequency is approximately

$$\frac{\partial \widetilde{H}_z}{\partial \widetilde{I}_z} \simeq \sqrt{\frac{m_i}{m_e}} \left(\frac{\xi}{\tilde{r}}\right)^{3/2} = \sqrt{\frac{m_i}{m_e}} \frac{1}{(\tilde{r}^2 + \tilde{z}_{max}^2)^{3/4}} \tag{3.28}$$

for arbitrary $\tilde{z}_{max}$. As expected, the maximum $\partial \widetilde{H}_z / \partial \widetilde{I}_z|_{max} = \sqrt{m_i/m_e}\tilde{r}^{-3/2}$, occurs for $z_{max} = 0$.

In the introduction we required that

$$\frac{\partial \widetilde{H}_z}{\partial \widetilde{I}_c} = \frac{m_i}{m_e} \gg \left.\frac{\partial \widetilde{H}_z}{\partial \widetilde{I}_z}\right|_{max} = \sqrt{\frac{m_i}{m_e}} \frac{1}{\tilde{r}^{3/2}}, \tag{3.29}$$

which can be written as the requirement $r \gg r_2(m_e/m_i)^{1/3} = r_1$. Since $\partial \widetilde{H}_z / \partial \widetilde{I}_z$ is much smaller than $\partial \widetilde{H}_z / \partial \widetilde{I}_z|_{max}$ for $\tilde{z}_{max} \gg \tilde{r}$, one might think that requirement (3.29) is overly restrictive. However, there are high frequency components in the motion that are of order of $\sqrt{m_i/m_e}\tilde{r}^{-3/2}$. These high frequency components are associated with the passage of the electron near the ion (i.e., for $z \lesssim r$).

In unscaled variables, the high frequency components are of order v_e/r, where $m_e v_e^2 \sim e^2/r$, which when scaled is $v_e/(r_2\Omega_{ci}) = \sqrt{m_i/m_e}\tilde{r}^{-3/2}$. Thus, the criterion used in the introduction is correct even for $\tilde{z}_{max} \gg \tilde{r}$.

Turning next to the requirement that the cross field motion be slow compared to the field aligned oscillations, we note first that the cross field motion affects the field aligned oscillations only through the time dependence in $r^2(t)$ [see Eq. (3.7)]. Thus, we examine the Poisson bracket

$$\frac{d\tilde{r}^2}{d\tilde{t}} = [\tilde{r}^2, \widetilde{H}] = 2\tilde{y}(\tilde{t})\widetilde{P} \tag{3.30}$$

where $\widetilde{H}$ is the scaled Hamiltonian (3.19).

The different trajectories in the figures of Section 3.4 are characterized by different time dependencies for $\tilde{y}(\tilde{t})$. Consider, for example, the three classes of trajectories in Fig. 3.4a. For the trajectories that encircle the minimum value of $\widetilde{H}$ at $\tilde{r} = 0$, $\tilde{y}(\tilde{t})$ oscillates at the rotation frequency of the vector $\vec{\tilde{r}}(\tilde{t})$, which when scaled is $\omega_D/\Omega_{ci} = 1/\tilde{r}^3$. Equivalently, from Hamilton's equations we obtain $\partial\widetilde{H}/\partial(\tilde{r}^2/2) \simeq \partial/\partial(\tilde{r}^2/2)(-1/\tilde{r}) = 1/\tilde{r}^3$

Figure 3.4a is plotted for the case where $z_{max} = 0$ and $\widetilde{H}_z = -1/\tilde{r}$. For a case where $z_{max} \gg r$, such as the plots in Fig. 3.9, one can show that the rotation frequency is approximately

$$\frac{\partial\widetilde{H}_z}{\partial(\tilde{r}^2/2)} \simeq \frac{1}{\tilde{r}^3}\xi^{3/2} = \frac{1}{\tilde{r}^{3/2}(z_{max}^2 + \tilde{r}^2)^{3/4}}. \tag{3.31}$$

For the trajectories in Fig. 3.4 that encircle the minimum in $\widetilde{H}$ at finite $\tilde{p}_y$, the ion and electron $\vec{E} \times \vec{B}$ drift together, as shown in Fig. 3.2, but the ion also executes cyclotron motion in the drift frame. In unscaled variables $r(t)$ varies at the frequency Ω_{ci}, which corresponds to the scaled frequency $\Omega_{ci}/\Omega_{ci} = 1$. One can easily check this result using the scaled Hamiltonian directly.

For the trajectories in Fig. 3.4 that encircle both minima, the scaled frequency of the motion is approximately $\Omega_{ci}/\Omega_{ci} = 1$, but there can be high frequency components associated with the close passage of the ion near the electron (i.e., for small $\tilde{r}$). An estimate for the high frequency component is

$$\frac{1}{\tilde{r}^2}\frac{d\tilde{r}^2}{d\tilde{t}} = \frac{\tilde{y}\widetilde{P}}{\tilde{r}^2} \lesssim \left(\frac{v_i}{r_2\Omega_{ci}}\right)\frac{1}{\tilde{r}} \lesssim \frac{1}{\tilde{r}^{3/2}}, \tag{3.32}$$

where $\tilde{r}$ is the minimum value of the cross field separation and we have assumed that $m_i v_i^2 \lesssim e^2/r$.The frequency of field aligned oscillations given in Eq. (3.27) must be large compared to the cross field frequencies, so we obtain the requirement

$$\sqrt{\frac{m_i}{m_e}}\frac{1}{(\tilde{r}^2+\tilde{z}^2)^{3/4}} \gg \frac{1}{\tilde{r}^{3/2}(\tilde{r}^2+\tilde{z}^2)^{3/4}},\ 1,\ \frac{1}{\tilde{r}^{3/2}}. \tag{3.33}$$

The first term on the right is small compared to the term on the left provided that $\tilde{r} \gg (m_e/m_i)^{1/3}$, which is the same as inequality (3.29). This inequality (i.e., $r \gg r_2(m_e/m_i)^{1/3} = r_1$) is the basic requirement that the the binding be sufficiently weak.

The second term on the right is small compared to the term on the left provided that the binding is not too weak [i.e., $(\tilde{r}^2+\tilde{z}^2)^{1/2} \gg (m_i/m_e)^{1/3}$]. Thus, the allowed electron-ion separations are bounded below and above [i.e., $(m_e/m_i)^{1/3} \ll \tilde{r}$, $(\tilde{r}^2+\tilde{z}^2)^{1/2} \ll (m_i/m_e)^{1/3}$]. Even for an electron and proton, the ratio of the upper to the lower bound is large, $(m_i/m_e)^{2/3} \simeq 150$. Finally, the third term on the right is small compared to the term on the left provided the atom is not too elongated [i.e., $\tilde{z}_{max}/\tilde{r} \ll (m_i/m_e)^{1/3}$]. For applications such as to the weakly bound pairs in the ATRAP and ATHENA experiments the lower bound (i.e., $(m_e/m_i)^{1/3} < \tilde{r}$) is the constraint of primary concern.

As examples, we now examine numerical solutions of the full equations of motion for a case where the lower bound constraint is satisfied and a case where it is not satisfied. In Fig. 3.9, the dashed circle indicates the lower bound (i.e.,

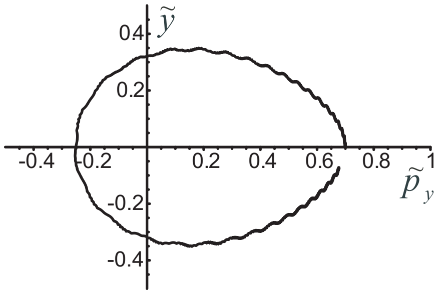

Figure 3.12: Numerical solution of the equations of motion for the trajectory starting at $\vec{\tilde{r}}_e = (0,0,0)$, $\vec{\tilde{r}}_i = (0.7,0,0)$, $\vec{\tilde{v}}_e = (0,0,-39.297)$, $\vec{\tilde{v}}_i = (0,0.8,0.0213919)$, $m_i/m_e = 1837$; the electron is not treated in drift approximation (i.e., full dynamics in magnetic field for both particles).

$\tilde{r} = (m_e/m_i)^{1/3} \simeq 0.082$) for the case of electron-proton mass ratio. The upper bound is well outside the domain of the figure. The adiabatic invariants should be conserved for trajectories that lie completely outside the dashed circle.

Figure 3.12 shows a trajectory obtained by numerically solving the full equations of motion, including the cyclotron and z-bounce motion. As expected for a case where the actions are good invariants, the trajectory differs only slightly from the corresponding trajectory in Fig. 3.9. The small ripples on the trajectory in Fig. 3.12 are caused by the change in the drift velocity as the electron oscillates back and forth in z. Smaller and higher frequency oscillations caused by the electron-cyclotron motion are not visible in the figure.

In Fig. 3.10, the dashed circle again is drawn to indicate the lower bound, $\tilde{r} = (m_e/m_i)^{1/3}$. Figure 3.13 shows the result of a numerical solution of the full equations of motion for a trajectory that starts at $(\tilde{p}_y, \tilde{y}) = (0.26, 0)$ and has values of $\sqrt{m_i/m_e}\widetilde{I}_z$ and $\widetilde{P}_Y$ corresponding to Fig. 3.10. For this trajectory $z_{max}/r \sim O(5-10)$ is rather large. The periodic helical excursions on the trajectory occur when the electron is near a turning point for the field aligned oscillations. The electron cyclotron motion combines with the slow ion velocity to produce the helical

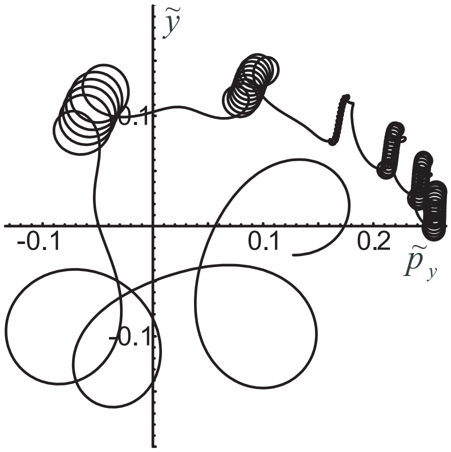

Figure 3.13: Numerical solution of the equations of motion for the trajectory starting at $\vec{\tilde{r}}_e = (0,0,0)$, $\vec{\tilde{r}}_i = (0.26,0,0)$, $\vec{\tilde{v}}_e = (0,0,-104.095)$, $\vec{\tilde{v}}_i = (0,1.24,0.056666)$, $m_i/m_e = 1837$; the electron is not treated in drift approximation (i.e., full dynamics in magnetic field for both particles).

excursion. When the field aligned oscillation brings the electron near the ion again, the transverse electric field rises dramatically, and the electron steps to the next helical excursion. The combination of the excursions and the periodic electron steps produce a trajectory that loosely follows the trajectory in Fig. 3.10. However, the rapid rise and fall of the transverse electric field breaks the adiabatic invariants, mixing axial and transverse kinetic energies. One can see in Fig. 3.10 that the size of the cyclotron radius varies from excursion to excursion gradually increasing.

3.6 Bohr-Sommerfeld Quantization

Since the motion is quasiclassical, we introduce quantum numbers by using the Bohr-Sommerfeld rule, that is by quantizing the actions. Hamiltonian (3.16) includes the the cyclotron action and the action for field aligned oscillations, but the action for the cross field drift motion must still be introduced.

This action is obtained by solving Eq. (3.16) for $p_y = p_y(H - I_{ce}\Omega_c e, P_Y, I_z, y)$

and evaluating the integral

$$I_D = \frac{1}{2\pi} \oint p_y(H - I_{ce}\Omega_{ce}, P_Y, I_z, y)dy \tag{3.34}$$

over a contour of constant H. I_D is simply $1/(2\pi)$ times the phase space area enclosed by the contour.

The quantization is effected by setting $I_D = \hbar n_D$, $I_z = \hbar n_z$, and $I_{ce} = \hbar(n_c + 1/2)$ in Eq. (3.34), where n_D, n_z, and n_c are integers. The 1/2 is retained in the quantization rule for the cyclotron motion since n_c may relatively small. In principle, Eq. (3.34) can be inverted to find the system energy as a function of P_Y and the quantum numbers: $H = H(P_Y, n_c, n_z, n_D)$. the momentum P_Y is not quantized.

Fortunately, this prescription is easy to carry out in the most important limit: a guiding center drift atom with relatively tight binding. In this case the drift motion corresponds to that shown in Fig. 3.1. Eq. (3.34) then reduces to the simple form

$$I_D = \frac{1}{2\pi} \oint p_y dy = \frac{1}{2\pi}\frac{eB}{c} \oint x dy = \frac{eB}{2\pi c}\pi r^2, \tag{3.35}$$

where r is the radius of the nearly circular orbit. Quantizing the action I_D then yields the allowed radii

$$r(n_D) = \sqrt{\frac{2\hbar n_D c}{eB}} \tag{3.36}$$

Substituting this expression and the quantized values of I_c and I_z into Hamiltonian (3.16) yields the allowed energies

$$H = \frac{P_Y^2}{2m_i} + \hbar\Omega_{ce}\left(n_c + \frac{1}{2}\right) - \frac{e^2}{r(n_D)}\Phi^{-1}\left[\frac{\hbar n_z}{e\sqrt{m_e r(n_D)}}\right]. \tag{3.37}$$

In writing the kinetic energy for the ion as $P_Y^2/(2m_i)$, use was made of the fact that $r(n_D)$ is small (relatively tight binding). For the case where I_z also is small (i.e.,

$z_{max} \ll r(n_D)$), approximations (3.12) and (3.13) yield the further simplification

$$H = \frac{P_Y^2}{2m_i} + \hbar\Omega_{ce}\left(n_c + \frac{1}{2}\right) - \frac{e^2}{r(n_D)} + \hbar\omega_z[r(n_D)]n_z, \tag{3.38}$$

where $\omega_z(r) = \sqrt{e^2/(m_e r^3)}$.

For small changes in the quantum numbers, the the change in the energy is given by

$$\Delta H = \frac{\partial H}{\partial I_c}\hbar\Delta n_c + \frac{\partial H}{\partial I_z}\hbar\Delta n_z + \frac{\partial H}{\partial I_D}\hbar\Delta n_D, \tag{3.39}$$

where $\partial H/\partial I_c = \Omega_{ce}$, $\partial H/\partial I_z = \omega_z$, and $\partial H/\partial I_D = \omega_D$. Thus, the energy level spacings for single integer changes in the quantum numbers (Δn_c, Δn_z, $\Delta n_D = 1$) are ordered as the frequencies (see inequality (3.1)). Further, since the energies associated with the cyclotron motion, field aligned oscillations, and Coulomb interaction are comparable, the corresponding quantum numbers are ordered inversely to the frequencies (i.e., $n_c \ll n_z \ll n_D$).

We note that a more accurate calculations would find corrections to $\partial H/\partial I_c$ that are of order $\partial H/\partial I_D = \omega_D$. However, these corrections contribute negligibly to the overall energy since $n_D \gg n_c$.

Finally, for a drifting pair with an electron orbit near the bottom of the outer well [see the small nearly circular orbit centered at ($y = 0$, $p_y \simeq P$) in Fig. 3.4]; the Hamiltonian may be Taylor expanded about the bottom of the well to obtain

$$H \simeq \Omega_{ce}I_{ce} + \omega_z I_z + \frac{1}{2}\frac{\partial^2 H}{\partial y^2}y^2 + \frac{1}{2}\frac{\partial^2 H}{\partial p_y^2}(p_y - p_y^{(0)})^2 \tag{3.40}$$

where

$$\begin{aligned} \frac{\partial^2 H}{\partial y^2} &= m_i\Omega_{ci}^2 - \frac{e^5 B^3}{c^3 (p_y^{(0)})^3}, \\ \frac{\partial^2 H}{\partial p_y^2} &= \frac{1}{m_i} - 2\frac{e^3 B^2}{c(p_y^{(0)})^3}, \end{aligned} \tag{3.41}$$

and $p_y^{(0)} \simeq P$ is the bottom of the well. Also, we have taken the simple case of small axial bounce motion and used Eq. (3.13). In this case, the Bohr-Sommerfeld quantization rules yield the energy levels

$$H \simeq \hbar\Omega_{ce}\left(n_c + \frac{1}{2}\right) + \hbar\omega_z n_z + \sqrt{\frac{\partial^2 H}{\partial y^2}\frac{\partial^2 H}{\partial p_y^2}}\hbar n_D. \qquad (3.42)$$

For our frequency ordering this expression reproduces results obtained previously using a quantum treatment for a quadratic approximation to the outer well [27].

3.7 Field Ionization

Thus far, we have considered the case where the external electric field vanishes in the laboratory frame. As was mentioned earlier, the case of a uniform electric field directed transverse to the magnetic field is included implicitly through a change of reference frame, that is, a shift in the initial ion velocities, $\vec{v}_i(0) \rightarrow \vec{v}_i(0) - c\vec{E} \times \vec{B}/B^2$. However, such a shift cannot account for an electric field that is parallel to the magnetic field or an electric field that is spatially varying.

In the ATRAP experiments [23], ionization of the guiding center drift atoms by an electric field (field ionization) was used to measure binding energies. For interpretation of such experiments, it would be useful to know the critical field for ionization as a function of the quantum numbers (or actions) for the atomic state.

First consider the case where the electric field is parallel to the magnetic field and the atom is moving slowly up a gradient in the field. The binding energy in Eq. (3.7) is then replaced by

$$H_z = \frac{p_z^2}{2\mu} - \frac{e^2}{\sqrt{r^2 + z^2}} - e\,E_z(t)z\,, \qquad (3.43)$$

where $E_z(t) \equiv E[z_{\text{atom}}(t)]$ is the electric field at the location of the atom, and we have neglected the variation in the field over the dimensions of the atom. As the atom moves up the gradient in the field, H_z is not constant in time. Rather, the action,

$$I_z(H_z, E_z, r) = \frac{1}{2\pi} \oint p_z[H_z, E_z, r, z]dz, \tag{3.44}$$

is constant until just before ionization. For simplicity, we consider tightly bound drift orbits with nearly circular orbits and neglect variation in r during the ionization process.

The electric field cannot increase indefinitely. At a certain critical value of $E_z(t)$, one of the turning points for the integral in Eq. (3.44) ceases to exist, the adiabatic invariant fails, and field ionization occurs. Implementing these ideas numerically yields the solid curve in Fig. 3.14: a plot of the scaled critical field, $E_z/(H_z^2/e^3)$, versus the scaled radius, $-H_z r/e^2$. Here, H_z is the initial binding energy, that is, the binding energy before the atom enters the electric field. Recall that H_z is related to I_z and r (or, the drift action $I_D = eB\,r^2/2c$) through Eq. (3.7). The limit $-H_z r/e^2 = 1$ corresponds to $I_z = 0$. In this limit, $E_z/(H_z^2/e^3)$ reaches the maximum value $2/3\sqrt{3}$. Although the full curve in Fig. 3.14 was obtained numerically, the maximum value can be obtained analytically. To check this theory, Hamilton's equations of motion were integrated forward in time through the field ionization event for various initial conditions. The results are shown as the points in Fig. 3.14. One can see that the theory based on constancy of I_z is accurate.

The scaling used in Fig. 3.14 provides a significant simplification. Without the scaling, the critical field would have to be written as a two dimensional function, $E_z = f(H_z, r)$. The scaling results from the fact that the Coulomb interaction does not introduce a separate length scale, so all lengths can be scaled in terms of e^2/H_z.

Next consider the case where an atom moves up a gradient in a transverse electric field. For a sufficiently weak gradient, the electric field can be treated as uniform over the dimensions of the atom, but slowly varying in time because of the

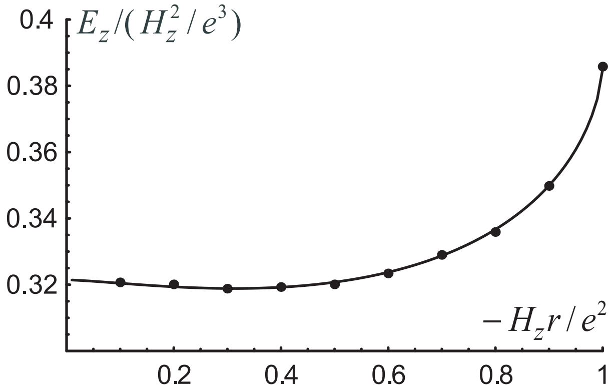

Figure 3.14: Ionization by an electric field parallel to the magnetic field. E_z is the critical field for ionization, H_z is the initial binding energy before the atom enters the electric field, and r is the radius of the nearly circular initial drift orbit. The solid curve results from a theory based on constancy of I_z, and the points are solutions of Hamilton's equations of motion.

motion of the atom. As mentioned, a uniform transverse field can be accounted for by a shift in ion velocity, or equivalently, a shift in the total transverse momentum

$$\vec{P} \rightarrow \vec{P}_{\text{eff}} = \vec{P}(t) - \frac{m_i c \vec{E}(t) \times \vec{B}}{B^2}, \tag{3.45}$$

where $\vec{E}(t)$ is the electric field at the location of the atom. We have also allowed for a slow time dependence in the atom momentum, $\vec{P}(t)$. The electric field polarizes the atom, and then the gradient in the field gives rise to a weak force on the atom and a slow time variation in the atom momentum. We will discuss this point later. Here, we need only realize that $\vec{P}_{\text{eff}}(t)$ changes slowly in time because of the atom motion.

Substituting $\vec{P}_{\text{eff}}(t)$ for $\vec{P}$ in Eq. (3.16), with P_x not set arbitrarily to zero, yields a Hamiltonian for the relative electron-ion motion, $\vec{r}(t)$. To understand the field ionization process, it is useful to refer again to Fig. 3.4b. The peak in the effective potential separating the Coulomb well and the outer well moves to the left as $|\vec{P}_{\text{eff}}(t)|$ increases. Correspondingly, in Fig. 3.4a the x-point in the separatrix moves to the left. We imagine that the atom starts with a nearly circular guiding center drift orbit inside the Coulomb well. As the atom moves up the gradient in the transverse electric field and $|\vec{P}_{\text{eff}}(t)|$ increases, the x-point moves toward the orbit, and the orbit distorts from circularity. Eventually, the phase trajectory crosses the separatrix to the outer well. The atom becomes a drifting pair and is quickly ionized by the gradient. One can easily show that drifting pairs are always separated by a field gradient. Effectively, field ionization occurs when the trajectory crosses the separatrix.

During this process, the Hamiltonian is not a constant of the motion since $\vec{P}_{\text{eff}}(t)$ depends explicitly on time. However, the transverse action

$$I_D = \frac{1}{2\pi} \oint p_y \, [y, H, I_z, \vec{P}_{\text{eff}}(t)] dy \tag{3.46}$$

is nearly constant up to the separatrix crossing. The characteristic time for a drift cycle is small compared to the time scale on which $\vec{P}_{\text{eff}}(t)$ changes. The constancy of the actions, I_D and I_z, allows us to determine the critical $|\vec{P}_{\text{eff}}|$ for field ionization as a function of the initial values of the actions.

Figure 3.15 shows the result of a numerical implementation of these ideas for the simple case where $I_z = 0$. The abscissa and ordinate are scaled as in Section 3.4. The ordinate is the scaled drift action $\tilde{I}_D = I_D/m_i\Omega_{\text{ci}}r_2^2 = \tilde{r}^2/2$, where $\tilde{r} = r/r_2$ is the scaled radius of the nearly circular initial drift orbit. Rather than referring to a critical effective momentum for ionization, we refer to a critical effective electric field, $E_{\text{eff}} \equiv |\vec{P}_{\text{eff}} \times \vec{B}/m_i c|$. The abscissa in Fig. 3.15 is the scaled critical field, $\tilde{E}_{\text{eff}} = E_{\text{eff}}/(e/r_2^2)$. The critical field is always larger than the momentum at which the outer well disappears (i.e., $\widetilde{E}_{\text{eff}} = |\widetilde{\vec{P}}_{\text{eff}}| > \widetilde{P}_c = 3/4^{1/3}$, see Fig. 3.5). The solid curve in Fig. 3.15 results from the theory based on constancy of the adiabatic invariants, and the points are from numerical solutions of the coupled electron-ion equations and equations of motion.

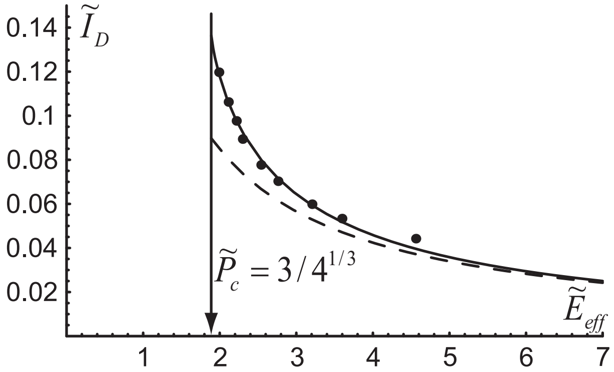

Figure 3.15: Ionization by an effective electric field transverse to the magnetic field for the simple case where the bounce action is zero (i.e., $I_z = 0$). The effective field $\widetilde{E}_{\text{eff}} = E_{\text{eff}}/(e/r_2^2)$ and the drift action $\widetilde{I}_D = \tilde{r}^2/2$ are scaled as in Section 3.4. The solid curve results from a theory based on the constancy of I_D and the points from the solution of the coupled electron-ion equations of motion. The dashed curve is an approximate analytic solution, $\widetilde{E}_{\text{eff}} \simeq \chi/\widetilde{I}_D$, that assumes tight binding ($\tilde{r}^3 \ll 1$). The arrow at $\widetilde{E}_{\text{eff}} = \widetilde{P}_c \equiv 3/4^{1/3}$ (see Fig. 3.5 for the definition of $\widetilde{P}_c$) limits the range of possible field ionization.

For the case of sufficiently tight initial binding (i.e., $\tilde{r}^3 \ll 1$), an analytic expression can be obtained for the scaled critical field

$$\tilde{E}_{\text{eff}} \simeq \chi/I_D = 2\chi/\tilde{r}^2, \tag{3.47}$$

where

$$\chi = \frac{1}{\pi}\left[\sqrt{2} + \ln(2 + 2^{3/2}) - 2\ln(2 + \sqrt{2})\right] \simeq 0.17 \ . \tag{3.48}$$

This approximate result is shown in the dashed curve in Fig. 3.15.

We emphasize that the effective electric field, $\widetilde{\vec{E}}_{\text{eff}} = \widetilde{\vec{E}}(t) + \widetilde{\vec{P}}(t) \times \hat{z}$, depends on both the lab-frame electric field and the atom momentum. Moreover, a gradient in the electric field gives rise to a force on the polarized atom and changes its momentum. In a subsequent paper we will discuss the motion of the atom under this force. Here, we simply note that the change in the effective field due to the change in the atom momentum is small for sufficiently tight binding (i.e., for $\tilde{r}^3 \ll 1$).

This chapter has been published in Physics of Plasmas **11**, 2382-2393 (2004), S.G. Kuzmin, T.M. O'Neil and M.E. Glinsky. S.G. Kuzmin was the primary investigator and author of this paper.

Chapter 4

Motion of Guiding Center Drift Atoms in the Electric and Magnetic Field of a Penning Trap

4.1 Abstract

The ATHENA and ATRAP collaborations have produced antihydrogen atoms by recombination in a cryogenic antiproton-positron plasma. This paper discusses the motion of the weakly bound atoms in the electric and magnetic field of the plasma and trap. The effective electric field in the moving frame of the atom polarizes the atom, and then gradients in the field exert a force on the atom. An approximate equation of motion for the atom center of mass is obtained by averaging over the rapid internal dynamics of the atom. The only remnant of the atom internal dynamics that enters this equation is the polarizability for the atom. This coefficient is evaluated for the weakly bound and strongly magnetized (guiding center drift) atoms understood to be produced in the antihydrogen experiments. Application of the approximate equation of motion shows that the atoms can be trapped radially in the large space charge field near the edge of the positron column. Also discussed are the curved trajectories followed by the atoms in moving from the plasma to a field ionization diagnostic. Finally, the critical field for ionization

is determined as an upper bound on the range of applicability of the theory.

4.2 Introduction

The ATHENA and ATRAP collaborations at CERN have reported the production of cold antihydrogen atoms [21, 22]. The atoms result from recombination when cold antiprotons are added to a cryogenic positron plasma in a Penning trap configuration. The ATRAP collaboration measured binding energies in the range of meV [23].

Here we discuss the motion of these weakly bound atoms in the magnetic and electric field of the trap. Because the binding is so weak, even a modest electric field produces a significant polarization of an atom. A gradient in the field then exerts a force on the atom, causing acceleration. Typically, the atom is moving across the magnetic field, and it is the effective electric field in the moving frame of the atom that causes the polarization and the acceleration. In the laboratory frame, both electric and magnetic forces must be taken into account.

In the experiments, the magnetic field is nearly uniform and the electric field varies by only a small amount over the dimensions of the atom. Also, the time scale for the internal dynamics of the atom is short compared to the time scale for the atom to move a significant distance. Taking advantage of these orderings, we obtain an approximate equation of motion for the atom center of mass. The only remnant of the atom internal dynamics that enters the equation of motion is the polarizability. The approximate equation of motion provides a substantial simplification because it averages over the rapid internal dynamics of the atom.

An interesting implication of the equation of motion is that a weakly bound atom can be trapped radially in the large electric field region near the edge of a long cylindrical positron column. The reason for the trapping is easy to understand physically. For a uniform density unneutralized column of positrons, the radial space charge field increases linearly with radius inside the column and falls off inversely with radius outside the column. Thus, there is a region of large field near the plasma edge, and polarizable material (the atom) is attracted to a region of maximum field.

We will find that the polarization forces create a potential well of approximate depth αE^2, where α is the polarizability of the atom and E is the electric field strength. In Gaussian units, the polarizability has the dimensions length cubed, and the polarizability for an atom of size r_a is of order $\alpha \sim r_a^3$. Since the binding energy for an atom is of order e^2/r_a, the depth of the well scales inversely with the cube of the binding energy. Thus, the effects discussed here are more pronounced for weakly bound atoms. Of course, a weakly bound atom suffers field ionization from a relatively weak field. The critical field for ionization is approximately $E \sim e/r_a^2$. Using this field strength as an upper bound for E shows that the maximum well depth is the binding energy of the atom:

$$\alpha E^2 = (\alpha/r_a^3) r_a^3 \left(\frac{E}{e/r_a^2}\right)^2 \left(\frac{e}{r_a^2}\right)^2 \lesssim \frac{e^2}{r_a} \tag{4.1}$$

For the example discussed in the last paragraph, radial trapping is possible only when the atom binding energy is larger than the kinetic energy of the atom center of mass.

The ATRAP collaboration uses field ionization as a diagnostic, and the ionization region is some distance from the plasma. As a second application of the approximate equation of motion, we determine trajectories followed by weakly bound atoms in moving from the recombination region (inside the positron plasma) to the field ionization region. Depending on the parameters, a straight line orbit may or may not be a good approximation. We will see that the polarization forces produce a significant deflection of the atom when the binding energy is larger than the center of mass kinetic energy. Knowledge of the trajectories is an important input to estimates of antihydrogen production rates based on solid angle considerations.

The analysis divides naturally into two parts: the derivation of the equation of motion and the calculation of the polarizability. In Section 4.3, we derive an approximate equation of motion for the expectation value of the atom center of mass coordinates, $\langle \vec{R}_{\mathrm{cm}} \rangle(t) \equiv \langle \Psi | \vec{R}_{\mathrm{cm}} | \Psi \rangle$. The derivation of the equation of motion depends on the spatial and temporal orderings mentioned above but otherwise is general. On the other hand, determination of the polarizability requires a more detailed specification of the internal dynamics for the atom.

In Section 4.4, we evaluate the polarizability for the special case of guiding center drift atom [24]. As discussed in recent literature [25, 31], these weakly bound and strongly magnetized atoms are thought to be produced in the antihydrogen experiments. For these novel atoms, the cyclotron frequency for the positron is much larger than the other dynamical frequencies and the cyclotron radius is much smaller than the separation between the positron and antiproton. Under these circumstances, the rapid cyclotron motion can be averaged out and the positron dynamics treated by guiding center drift theory. The dynamics is quasi-classical, since the binding energy is much smaller than the Rydberg energy (four orders of magnitude smaller for the meV binding energies measured in the ATRAP experiments). Fortunately, the dynamics for guiding center atoms is integrable, and the polarizability can be evaluated with perturbation theory.

In Section 4.5, we use the approximate equation of motion and calculated coefficient of polarizability to discuss the radial trapping of weakly bound atoms in the large space charge field of a long positron column. The geometry and field strengths used are characteristic of the ATHENA experiments. Orbits from the approximate equation of motion are shown to be in good agreement with those from lengthy numerical solutions of the coupled positron-antiproton equations of motion. These latter solutions involve over a million cycles of the internal atom dynamics. The comparison demonstrates the fidelity of the approximate equation of motion and also the substantial simplification it provides in averaging out the rapid internal dynamics. In a second application, we discuss the curved trajectories followed by weakly bound atoms in moving from the plasma to a field ionization region. Here we use field strengths and geometry characteristic of ATRAP.

For the special case of a purely radial space charge field, the approximate equation of motion was obtained previously [29]. The derivation here is more general in that it allows all three components of the electric field. Also, the derivation here is not based on classical mechanics and the guiding center drift approximation. This specialization is used here only to obtain the polarizability, not in the derivation of the approximate equation of motion. The present discussion of the polarizability tensor is more complete than in reference [29] and includes a discussion of field ionization. Also, the determination of trajectories for atoms moving from the plasma to the field ionization region is new.

4.3 Approximate Equation of Motion

We consider a positron (particle 1) and an antiproton (particle 2), although the results apply equally to an electron and a singly ionized ion. The mass ratio m_1/m_2 is assumed to be small, but is not specified to a specific value. The two particles interact electrostatically and move in the uniform magnetic field $\vec{B} = \hat{z}B$ and the spatially varying electric field $\vec{E} = -\vec{\nabla}\phi$. For the choice of vector potential

$\vec{A} = Bx\hat{y}$, the Hamiltonian operator is given by

$$\begin{aligned} H = & \frac{p_{z1}^2}{2m_1} + \frac{p_{x1}^2}{2m_1} + \frac{(p_{y1} - \frac{eB}{c}x_1)^2}{2m_1} \\ & + \frac{p_{z2}^2}{2m_2} + \frac{p_{x2}^2}{2m_2} + \frac{(p_{y2} + \frac{eB}{c}x_2)^2}{2m_2} - \frac{e^2}{\sqrt{(x_1 - x_2)^2 + (y_1 - y_2)^2 + (z_1 - z_2)^2}} \\ & + e\phi(x_1, y_1, z_1) - e\phi(x_2, y_2, z_2). \end{aligned} \tag{4.2}$$

The effect of spin has been neglected, since the magnetic field is uniform and the spin-field interaction does not couple the spin and orbital dynamics. The usual spin-orbit interaction, which is smaller than the electrostatic interaction by order $(v/c)^2$, is very small for the small binding energies (and small velocities) considered here.

It is useful to introduce relative coordinates through the transformation

$$\begin{aligned} x =& x_1 - x_2, & p_x =& \frac{m_2 p_{x1} - m_1 p_{x2}}{m_1 + m_2} \\ y =& y_1 - y_2, & p_y =& \frac{m_2(p_{y1} - \frac{eB}{c}x_2) - m_1(p_{y2} + \frac{eB}{c}x_1)}{m_1 + m_2} \\ z =& z_1 - z_2, & p_z =& \frac{m_2 p_{z1} - m_1 p_{z2}}{m_1 + m_2} \\ X =& \frac{m_1 x_1 + m_2 x_2}{m_1 + m_2} + \frac{c}{eB}(p_{y1} + p_{y2}), & P_X =& p_{x1} + p_{x2} - \frac{eB}{c}(y_1 - y_2) \\ Y =& \frac{(2m_2 + m_1)y_2 - m_2 y_1}{m_1 + m_2} + \frac{c}{eB}(p_{x1} + p_{x2}) & P_Y =& p_{y1} + p_{y2} \\ Z =& \frac{m_1 z_1 + m_2 z_2}{m_1 + m_2} & P_Z =& p_{z1} + p_{z2}. \end{aligned} \tag{4.3}$$

Classically, this is a canonical transformation, as can be verified by observing that the Poisson brackets for the new coordinates and momenta have the canonical values (i.e., $[Q_i, P_j] = \delta_{ij}$). Quantum mechanically, the commutators for the new operations have the canonical values (i.e., $[Q_r, P_s] = \delta_{rs} i\hbar$).

The vector $\vec{r} = (x, y, z)$ is the relative coordinate between the positron and antiproton. The momentum P_Z is the total (or center of mass) momentum along the magnetic field. The transverse components (P_X, P_Y) are often called pseudomenta [26]. P_Y is the sum of the y-components of the canonical momentum for the two particles; P_X is the corresponding sum that would be obtained for the x-components using a different choice of vector potential (i.e., $\vec{A}' = -By\hat{x}$). The two choices ($\vec{A} = Bx\hat{y}$ and $\vec{A}' = -By\hat{x}$) are related by a gauge transformation and both produce the given magnetic field (i.e., $\vec{\nabla} \times \vec{A} = \vec{\nabla} \times \vec{A}' = \hat{z}B$). We will see that $\vec{P} = (P_X, P_Y, P_Z)$ are constants of the motion for the special case of a spatially uniform electric field.

For future convenience, we note that the antiproton and positron coordinates are given by

$$\vec{r}_2 = \left(X - \frac{c}{eB}P_Y - \frac{m_1 x}{m_1 + m_2} \, , \, Y - \frac{c}{eB}P_X - \frac{m_1 y}{m_1 + m_2} \, , \, Z - \frac{m_1 z}{m_1 + m_2} \right), \tag{4.4}$$

$$\vec{r}_1 = \vec{r}_2 + \vec{r}. \tag{4.5}$$

Likewise, the center of mass coordinates are given by

$$\vec{R}_{\text{cm}} = \frac{m_1 \vec{r}_1 + m_2 \vec{r}_2}{m_1 + m_2} = \left(X - \frac{c}{eB}P_Y \, , \, Y - \frac{c}{eB}P_X, Z \right) \, . \tag{4.6}$$

In terms of the new operators, the Hamiltonian is given by

$$\begin{aligned} H = {} & \frac{|\vec{P}|^2}{2M} - \frac{eB}{MC}(P_Y x - P_X y) + \frac{M\Omega_{\text{CM}}^2}{2}(x^2 + y^2) \\ & + \frac{p_x^2}{2\mu} + \frac{(p_y - \sqrt{1 - \frac{4\mu}{M}\frac{eB}{c}}x)^2}{2\mu} + \frac{p_z^2}{2\mu} - \frac{e^2}{\sqrt{x^2 + y^2 + z^2}} + e\phi(\vec{r}_1) - e\phi(\vec{r}_2), \end{aligned} \tag{4.7}$$

where $M = m_1 + m_2$ and $\mu = m_1 m_2 / (m_1 + m_2)$ are the total and reduced mass, $\Omega_{\text{CM}} \equiv eB/MC$ is the cyclotron frequency for the total mass, and $\vec{r}_2$ and $\vec{r}_1$ have been introduced as shorthand for the variables in relations (4.4) and (4.5).

Let $\langle\vec{P}\rangle \equiv \langle\Psi|\vec{P}|\Psi\rangle$ be the expectation value of the total momentum. The rate of change of this quantity is given by

$$\frac{d}{dt}\langle\vec{P}\rangle = \langle\Psi|\frac{1}{i\hbar}[\vec{P}, H]|\Psi\rangle. \tag{4.8}$$

Using $\vec{P} = (\hbar/i)(\partial/\partial X, \partial/\partial Y, \partial/\partial Z)$ to evaluate the commutator $[\vec{P}, H]$ yields the result

$$\frac{d\langle\vec{P}\rangle}{dt} = \langle\Psi|[e\vec{E}(\vec{r}_1) - e\vec{E}(\vec{r}_2)]|\Psi\rangle\ , \tag{4.9}$$

where the electric field $\vec{E} = -\vec{\nabla}\phi$, has been introduced. As anticipated, $\vec{P}$ is a constant of the motion for the case of a spatially uniform electric field.

We assume that the spatial gradient in the field is small and work only to first order in the gradient. Let $\ell \sim |\vec{E}|/|\vec{\nabla}E|$ be the scale length of the field and r_a be the size of the atom. Formally, the wave function $|\Psi\rangle$ is negligibly small for $r = |\vec{r}_1 - \vec{r}_2|$ larger than r_a. We assume that $r_a \ll \ell$, and work only to first order in the small parameter $r_a/\ell \ll 1$. To this order, Eq. (4.9) can be rewritten as

$$\frac{d\langle\vec{P}\rangle}{dt} \simeq \langle\Psi|[e\vec{r}\cdot\vec{\nabla}\vec{E}(\langle\vec{R}_{\rm cm}\rangle)]|\Psi\rangle\ , \tag{4.10}$$

where $\langle\vec{R}_{\rm cm}\rangle \equiv \langle\Psi|\vec{R}_{\rm cm}|\Psi\rangle$ is the expectation value of the center of mass position operator [see Eq. (4.6)]. In terms of the expectation value $\langle\vec{r}\rangle \equiv \langle\Phi|\vec{r}|\Psi\rangle$, Eq. (4.10) takes simple form

$$\frac{d\langle\vec{P}\rangle}{dt} \simeq e\langle\vec{r}\rangle\cdot\vec{\nabla}\vec{E}(\langle\vec{R}_{\rm cm}\rangle)\ . \tag{4.11}$$

Likewise, the rate of change of $\langle\vec{R}_{\rm cm}\rangle$ is given by

$$\frac{d\langle\vec{R}_{\rm cm}\rangle}{dt} = \left\langle\Psi\left|\frac{1}{i\hbar}[\vec{R}_{\rm cm}, H]\right|\Psi\right\rangle = \frac{\langle\vec{P}\rangle}{M} + \frac{e\langle\vec{r}\rangle}{MC}\times\vec{B}\ , \tag{4.12}$$

where use has been made of definition (4.6), Hamiltonian (4.7) and the basic commutator relations. Taking the time derivative of Eq. (4.12) and using Eq. (4.11) to replace $d\langle\vec{P}\rangle/dt$ yields the result

$$M\frac{d^2\langle\vec{R}_{\rm cm}\rangle}{dt^2} = \vec{d}\cdot\vec{\nabla}\vec{E}(\langle\vec{R}_{\rm cm}\rangle) + \frac{1}{c}\frac{d}{dt}\vec{d}\times\vec{B}\ , \tag{4.13}$$

where $\vec{d} \equiv e\langle\vec{r}\rangle$ is the dipole moment of the atom.

The next step is to find an expression for $\vec{d}$ in terms of fields and the center of mass velocity [i.e., $\vec{E}(\langle\vec{R}_{\rm cm}\rangle)$, $\vec{B}$, and $d\langle\vec{R}_{\rm cm}\rangle/dt$]. Equation (4.13) will then be a proper equation of motion for the evolution of $\langle\vec{R}_{\rm cm}\rangle(t)$ in the given fields.

The first term on the right-hand side of Eq. (4.13) is obviously first order in the spatial gradient of the electric field [i.e., $O(1/\ell)$], and the second term is as well, since d/dt turns out to be first order in the gradient. Thus, in Hamiltonian (4.7) we set $e\phi(r_1) - e\phi(r_2) = e\vec{E}\cdot\vec{r}$, where the field $\vec{E}$ is independent of $\vec{r}$. To zero order in $r_a/\ell \ll 1$, we set $\vec{E} = \vec{E}(\langle\vec{R}_{cm}\rangle)$.

There remains the question of the time dependence in $\vec{E}[\langle\vec{R}_{\rm cm}\rangle(t)]$. We assume that the time scale for the internal dynamics (relative motion) is short compared to the time for the atom as a whole to move a distance ℓ. This latter time is the time scale on which $\vec{E}[\langle\vec{R}_{\rm cm}\rangle(t)]$ changes significantly. Thus, we use an adiabatic approximation and neglect the time-dependence in $\vec{E}[\langle\vec{R}_{\rm cm}\rangle(t)]$ when solving for the internal motion (relative motion).

As mentioned earlier, $\vec{P}$ is a constant of the motion for a uniform electric field. Thus, in Hamiltonian (4.7) we replace the operator $\vec{P}$ by the constant eigenvalue $\vec{P}$ and replace the potential difference $[e\phi(\vec{r}_1) - e\phi(\vec{r}_2)]$ by $-e\vec{E}\cdot\vec{r}$ where $\vec{E}$ is a constant field. This yields a Hamiltonian for the relative motion

$$H = \frac{p_x^2}{2\mu} + \frac{(p_y - \sqrt{1-\frac{4\mu}{M}}\frac{eB}{c}x)^2}{2\mu} + \frac{p_z^2}{2\mu} - \frac{e^2}{\sqrt{x^2+y^2+z^2}} + \frac{M}{2}\Omega_{\rm CM}^2(x^2+y^2) - e\vec{\mathcal{E}}\cdot\vec{r}, \tag{4.14}$$

where

$$\vec{\mathcal{E}} = \vec{E} + \frac{\vec{P}\times\vec{B}}{MC} \tag{4.15}$$

is the effective field acting on the atom, and the constant term $P^2/(2M)$ has been dropped from the Hamiltonian.

For the special case $\vec{\mathcal{E}} = 0$, H commutes with the parity operator, $\mathcal{P}$. If $\psi_{n_1,n_2,n_3}(\vec{r})$ is an eigenfunction of H corresponding to the eigenvalue $\bar{H}_{n_1,n_2,n_3}$, then $\mathcal{P}\psi_{n_1,n_2,n_3}(\vec{r}) = \psi_{n_1,n_2,n_3}(-\vec{r})$ is an eigenfunction for the same eigenvalue. Except for very special cases (e.g., $\vec{B} = 0$), one expects the energy levels $\bar{H}_{n_1,n_2,n_3}$ to be non-degenerate. Here, the integers (n_1, n_2, n_3) specify the quantum state. For the special case of guiding center drift dynamics, we will identify these integers in the next section. Therefore, $\mathcal{P}\psi_{n_1,n_2,n_3}$ and ψ_{n_1,n_2,n_3} differ only by a constant; further, that constant must be ±1, that is, ψ_{n_1,n_2,n_3} must have even or odd parity. Thus, the dipole moment $\vec{d} = e\langle\Psi|\vec{r}|\Psi\rangle$ vanishes for $\vec{\mathcal{E}} = 0$.

For sufficiently small $\vec{\mathcal{E}}$, Taylor expansion suggests the linear relationship $\vec{d} = \hat{\alpha}\cdot\vec{\mathcal{E}}$, where the polarizability matrix is given by

$$\hat{\alpha} = \begin{pmatrix} \alpha_\perp & 0 & 0 \\ 0 & \alpha_\perp & 0 \\ 0 & 0 & \alpha_z \end{pmatrix} . \tag{4.16}$$

Because of the magnetic field, the parallel and transverse polarizabilities are not equal.

Combining Eqs. (4.12) and (4.16) with the relation $\vec{d} = \hat{\alpha}\cdot\vec{\mathcal{E}}$ yields the expressions

$$\begin{aligned} d_z &= \alpha_z E_z \\ \left(1 - \frac{\alpha_\perp B^2}{MC^2}\right)\vec{d}_\perp &= \alpha_\perp\left[\vec{E}_\perp + \frac{1}{c}\frac{d\langle\vec{R}_{\rm cm}\rangle}{dt}\times B\right] . \end{aligned} \tag{4.17}$$

Substituting these expressions into Eq. (4.13) yields the equation of motion

$$M\left(1 - \frac{\alpha_\perp B^2}{MC^2}\right)\frac{dV_z}{dt}\hat{z} + M\frac{d\vec{V}_\perp}{dt} =$$

$$\frac{1}{2}\vec{\nabla}\left[\left(1 - \frac{\alpha_\perp B^2}{MC^2}\right)\alpha_z E_z^2 + \alpha_\perp E_\perp^2\right] + \alpha_\perp\frac{\vec{V}_\perp\times\vec{B}}{c}\cdot\vec{\nabla}\vec{E} + \alpha_\perp\frac{\vec{V}}{c}\cdot\vec{\nabla}(\vec{E}\times\vec{B}), \tag{4.18}$$

where $\vec{V} \equiv d\langle\vec{R}_{\rm cm}\rangle/dt$, $\vec{E}$ is evaluated at $\langle\vec{R}_{\rm cm}\rangle$, α_z and $\alpha_\perp$ have been treated as constants, and use has been made of $\vec{\nabla}\times\vec{E} = 0$. Taking the dot product of Eq. (4.18) with respect to $\vec{V}$ and integrating over time yields an equation for conservation of energy

$$\left(1 - \frac{\alpha_\perp B^2}{MC^2}\right)\frac{MV_z^2}{2} + \frac{MV_\perp^2}{2} - \frac{\alpha_\perp E_\perp^2}{2} - \alpha_z\left(1 - \frac{\alpha_\perp B^2}{MC^2}\right)\frac{E_z^2}{2} = \text{const}, \tag{4.19}$$

where again use has been made of $\vec{\nabla}\times\vec{E} = 0$.

It is convenient to introduce cylindrical coordinates for the center of mass, $\vec{R}_{cm} = (R, \Theta, Z)$. Typically, the electric potential has no dependence on the angle Θ, and the azimuthal electric field vanishes. In this case, Eq. (4.18) yields an equation for conservation of canonical angular momentum

$$\left(1 - \frac{\alpha_\perp B^2}{Mc^2}\right)^{-1}\left[MV_\theta R + \frac{\alpha_\perp B}{c}RE_R(R,Z)\right] = \text{const}. \tag{4.20}$$

Formal expressions for α_z and $\alpha_\perp$ can be obtained in terms of the energy levels for the relative motion, $\bar{H}_{n_1,n_2,n_3}(\mathcal{E}_z,\mathcal{E}_\perp)$. In the adiabatic approximation considered here, the quantum numbers for the state (i.e., (n_1,n_2,n_3)) remain fixed but the energy levels evolve as a function of the slowly varying $\mathcal{E}_z$ and $\mathcal{E}_\perp$. From the relations $-ez = \partial H/\partial\mathcal{E}_z$ and $\langle\Psi|\partial H/\partial\mathcal{E}_z|\Psi\rangle = \partial/\partial\mathcal{E}_z\langle\Psi|H|\Psi\rangle$, one finds that

$$d_z \equiv \langle ez\rangle = -\frac{\partial}{\partial\mathcal{E}_z}\bar{H}_{n_1,n_2,n_3}(\mathcal{E}_z,\mathcal{E}_\perp). \tag{4.21}$$

Likewise, one finds that

$$\vec{d}_\perp \equiv \langle e\vec{r}_\perp\rangle = -\frac{\partial}{\partial\vec{\mathcal{E}}_\perp}\bar{H}_{n_1,n_2,n_3}(\mathcal{E}_z,\mathcal{E}_\perp). \tag{4.22}$$

The linear polarizabilities are then given by

$$\alpha_z = -\left.\frac{\partial^2\bar{H}}{\partial^2\mathcal{E}_z^2}\right|_{\mathcal{E}_z,\mathcal{E}_\perp=0} \qquad \alpha_\perp = -\left.\frac{\partial^2\bar{H}}{\partial^2\mathcal{E}_\perp^2}\right|_{\mathcal{E}_z,\mathcal{E}_\perp=0}. \tag{4.23}$$

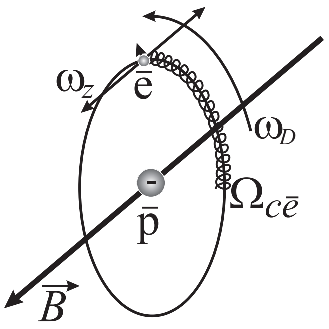

Figure 4.1: Drawing of a guiding center drift atom. In order of descending frequency, the positron executes cyclotron motion, oscillates back and forth along a field line in the Coulomb well of the antiproton, and $\vec{E} \times \vec{B}$ drifts around the ion.

4.4 Polarizability for Guiding Center Drift Atoms

In this section, we evaluate the polarizability for the weakly bound and strongly magnetized atoms produced in the antihydrogen experiments. In recent literature, these atoms are referred to as guiding center drift atoms [24, 25, 31] The cyclotron frequency for the positron is much larger than the other frequencies that characterize the dynamics, and the cyclotron radius much smaller than the positron-antiproton separation. Under these circumstances, the rapid and highly localized cyclotron motion can be averaged out and the positron dynamics treated by guiding center drift theory. A quasi-classical treatment of the atoms is possible, since the binding energy is much smaller (four orders of magnitude smaller) than the Rydberg energy.

Figure 4.1 illustrates the internal dynamics (relative motion) of a guiding center drift atom for the special case where the effective electric field vanishes (i.e., $\vec{\mathcal{E}} \to 0$). The positron executes very rapid cyclotron motion with a small cyclotron radius. More slowly, the positron oscillates back and forth along the magnetic field in the Coulomb well of the antiproton. More slowly still, the positron and antiproton move in circular cross magnetic field orbits around a common point.

The positron cross field motion is well described as the $\vec{E}\times\vec{B}$ drift velocity in the electric field of the antiproton, but full dynamics must be retained to describe the cross field motion of the antiproton. In Fig. 1, $\vec{r}=\vec{r}_1-\vec{r}_2$ is the relative position so the motion is shown from the perspective of the antiproton.

The relative motion is described by Hamiltonian (4.14) with the effective electric field set equal to zero (i.e., $\vec{\mathcal{E}}=0$). We will see that the first two terms describe the rapid cyclotron motion, the next two the field aligned oscillations, and the third and fourth the cross field motion. The cyclotron frequency is $\sqrt{1-4\mu/M}\;eB/\mu c \simeq eB/m_e c \equiv \Omega_{\text{ce}}$. For the case where the amplitude of the field aligned oscillations is not too large (i.e., $z_{\max} \lesssim r_\perp = \sqrt{x^2+y^2}$), the frequency of these oscillations is approximately $\omega_z = \sqrt{e^2/m_e r_\perp^3}$. This estimate has used the Taylor expansion $e^2/\sqrt{z^2+r_\perp^2} \approx e^2/r_\perp - e^2z^2/2r_\perp^3$. For this same case, we will see that the frequency of the cross field motion is approximately $\omega_D+\Omega_{\text{CM}}$, where $\omega_D \equiv ce/Br_\perp^3$ is the $\vec{E}\times\vec{B}$ drift frequency of a positron in the Coulomb field of a stationary antiproton. We will be interested in cases where $\omega_D \gtrsim \Omega_{\text{CM}}$, so we simply use ω_D as the estimate of the frequency for cross field motion.

Since the positron cyclotron frequency, $\Omega_{\text{ce}}=eB/m_ec$, is related to $\omega_z=\sqrt{e^2/m_er_\perp^3}$ and $\omega_D=ce/Br_\perp^3$ through the equation $\Omega_{\text{ce}}=\omega_z^2/\omega_D$, the requirement that Ω_{ce} be larger than the other two frequencies imposes the ordering

$$\Omega_{\text{ce}} \gg \omega_z \gg \omega_D. \tag{4.24}$$

The ordering is realized for sufficiently weak binding, that is, for $r \gg (m_ec^2/B^2)^{1/3}$. This inequality is required for validity of the analysis.

Note that the inequality implies not only that the positron cyclotron frequency is large, but also that the positron cyclotron radius is small. We have in mind cases where the positron kinetic energy is smaller than or of order of the electrostatic binding energy (i.e., $m_e \mathrm{v}_e^2/2 \lesssim e^2/r$). The inequality $r \gg (m_e c^2/B^2)^{1/3}$ then implies that $r_{\mathrm{ce}} \equiv \mathrm{v_e}/\Omega_{\mathrm{ce}} \ll r$.

For r comparable to $(m_e c^2/B^2)^{1/3}$ our guiding center analysis fails. All three frequencies in inequality (4.24) are comparable, and the positron motion is chaotic [25, 35, 36]. For $r \ll (m_e c^2/B^2)^{1/3}$, the cyclotron frequency is small compared to the Kepler frequency, and the positron motion is again integrable. In this case, one can think of the weakly bound pair as a high-n Rydberg atom with a Zeeman perturbation [37]. For cases where $r < (m_e c^2/B^2)^{1/3}$, equation of motion (4.18) remains valid, but the polarizability derived here does not apply.

As mentioned, the ATRAP collaboration measured binding energies of order meV, which corresponds to $\bar{e}-\bar{p}$ separation of order 10^{-4} cm [23]. The magnetic field strength is 5 T, so the critical radius is $(m_e c^2/B^2)^{1/3} = 7 \times 10^{-6}$ cm. Thus, the separation is much larger than $(m_e c^2/B^2)^{1/3}$, and the weakly bound pairs are guiding center atoms. The cyclotron frequency for the positron is about 100 times larger than the $\vec{E} \times \vec{B}$ drift frequency ω_D, and the cyclotron radius is about 100 times smaller than the separation.

The simple symmetry of the orbit shown in Fig. 4.1 is a consequence of the choice $\vec{\mathcal{E}} = 0$. For non-zero $\vec{\mathcal{E}}$, the last term in Hamiltonian (4.14) modifies the motion, but for sufficiently small $\vec{\mathcal{E}}$ the modifications can be treated as a perturbation. The term $e\mathcal{E}_z z$ shifts the field aligned oscillations, destroying symmetry of the orbit in $\pm z$. Likewise, the term $e\vec{\mathcal{E}}_\perp \cdot \vec{r}_\perp$ destroys the circular symmetry of the cross field orbit. Of course, these distortions give rise to the polarization of interest.

Because the atom moves, the effective field $\vec{\mathcal{E}} = \vec{\mathcal{E}}[\langle \vec{R}_{\mathrm{cm}} \rangle(t)]$ varies in time. As mentioned earlier, we assume that the time scale for this motion (i.e., $\tau \sim \ell/V_{\mathrm{cm}}$) is long compared to the time scale for the internal dynamics. Thus, frequency ordering (4.24) is extended to be

$$\Omega_{\rm ce} \gg \omega_z \gg \omega_D \gg 1/\tau \ . \tag{4.25}$$

The frequency ordering then implies that the internal dynamics for the atom is integrable. Because the positron cyclotron frequency is much larger than the other frequencies, the cyclotron action is a good adiabatic invariant. Use of guiding center drift dynamics automatically takes this invariant into account and removes the rapid cyclotron motion from the problem. Because the frequency of field aligned oscillations is larger than the remaining frequencies, the action for the field aligned oscillations is a good adiabatic invariant. Introducing this action and averaging over the field aligned oscillations then leaves the cross field drift motion as the largest frequency motion. Thus, the drift action is a good adiabatic invariant. The values of these three actions determine the internal state of the atom. In reference [25], Bohr-Sommerfeld quantization rules are used to associate a quantum number with each action. To the extent that $1/\tau$ is small compared to the frequencies for the internal dynamics [i.e., ordering (4.25)], the adiabatic approximation implies that the actions (or quantum numbers) remain constant as the atom moves through the external field. In the language of atomic physics, we make a triple Born-Oppenheimer approximation.

Returning to Hamiltonian (4.14) with frequency ordering (4.25) in mind, we first treat the cyclotron motion. The first two terms in Eq. (4.14) comprise the cyclotron Hamiltonian

$$H_c = \frac{p_x^2}{2\mu} + \frac{(p_y - \sqrt{1-\frac{4\mu}{M}}\frac{eBx}{c})^2}{2\mu}, \tag{4.26}$$

where p_y may be treated as a constant on the cyclotron time scale. The Hamiltonian describes oscillations in x at the frequency $eB/\mu c\,\sqrt{1-4\mu/M} \simeq \Omega_{\rm ce}$ and centered about the guiding center position $x_g = p_y(c/eB)(1 - 4\mu/M)^{1/2} \simeq cp_y/eB$. By introducing the cyclotron action,

$$I_c = \frac{1}{2\pi} \oint dx \, p_x[\bar{H}_c, x] \, , \tag{4.27}$$

one finds $\bar{H}_c = I_c\Omega_{\mathrm{ce}}$. Here, $\bar{H}_c$ has the same value as H_c but a different functional form. Making this replacement for the first two terms in Hamiltonian (4.14) and replacing x by $x_g = cp_y/eB$ in the remainder of the Hamiltonian yields the guiding center drift Hamiltonian [25]

$$H = I_c\Omega_{\mathrm{ce}} + \frac{p_z^2}{2\mu} - \frac{e^2}{\sqrt{r_\perp^2 + z^2}} - e\mathcal{E}_z z + \frac{M\Omega_{\mathrm{CM}}^2}{2} r_\perp^2 - e\vec{\mathcal{E}}_\perp \cdot \vec{r}_\perp, \tag{4.28}$$

where $\vec{r}_\perp = (cp_y/eB, y)$. In drift dynamics, y and $p_y = eB/cx$ are canonically conjugate coordinate and momentum [38]. The field aligned oscillations are governed by the second, third, and fourth terms in Hamiltonian (4.28). We write the sum of these terms as the Hamiltonian

$$H_z = \frac{p_z^2}{2\mu} - \frac{e^2}{\sqrt{r_\perp^2 + z^2}} - e\mathcal{E}_z z \ , \tag{4.29}$$

where $r_\perp$ can be treated as constant on the time scale of the field aligned oscillations. The action for the field aligned oscillations is given by

$$I_z = \frac{1}{2\pi} \oint dz \sqrt{2\mu} \sqrt{\bar{H}_z + e^2/\sqrt{r_\perp^2 + z^2} + e\mathcal{E}_z z}, \tag{4.30}$$

which can be inverted at least formally, to obtain $\bar{H}_z = \bar{H}_z(r_\perp^2, I_z, \mathcal{E}_z)$. Again, $\bar{H}_z$ has the same value as H_z but different functional form.

Substituting $\bar{H}_z(r_\perp^2, I_z, \mathcal{E}_z)$ into Eq. (4.28) yields a Hamiltonian for the cross field motion

$$H = I_{\mathrm{ce}}\Omega_{\mathrm{ce}} + \bar{H}_z(r_\perp^2, I_z, \mathcal{E}_z) + \frac{M\Omega_{\mathrm{CM}}^2}{2} r_\perp^2 - e\vec{\mathcal{E}}_\perp \cdot \vec{r}_\perp \ . \tag{4.31}$$

For given values of H, I_{ce}, I_z, $\mathcal{E}_z$, and $\vec{\mathcal{E}}_\perp$ this equation determines the cross field orbit [i.e., $p_y(y)$, where $p_y = (eB/c)x$]. It is useful to introduce the action for the cross field motion (drift action)

$$I_D = \frac{1}{2\pi}\oint dy\; p_y[y, \bar{H} - \Omega_{\mathrm{ce}} I_c, I_z, \mathcal{E}_z, \mathcal{E}_\perp], \tag{4.32}$$

which can be inverted formally to obtain $\bar{H} = \bar{H}(I_c, I_z, I_D, \mathcal{E}_z, \mathcal{E}_\perp)$. Following reference [25], the Bohr-Sommerfeld rules for quantization are used to set

$$\bar{H} = \bar{H}[I_c = \hbar n_c, I_z = \hbar n_z, I_D = \hbar n_D, \mathcal{E}_z, \mathcal{E}_\perp]\;, \tag{4.33}$$

where the integers n_c, n_z, n_D remain fixed as $\vec{\mathcal{E}} = \vec{\mathcal{E}}[\langle \vec{R}_{\mathrm{cm}}\rangle(t)]$ evolves slowly in time. In expression (4.23) for the polarizability, the energy levels are simply $\bar{H}_{n_1,n_2,n_3} = \bar{H}(\hbar n_c, \hbar n_z, \hbar n_D, \mathcal{E}_z, \mathcal{E}_\perp)$, where $(n_1, n_2, n_3) = (n_c, n_z, n_D)$.

For linear polarizability, $\alpha_z = -\partial^2\bar{H}/\partial\mathcal{E}_z^2|_{\mathcal{E}_z,\mathcal{E}_\perp=0}$ can be evaluated setting $\mathcal{E}_\perp = 0$ at the outset. In this case the cross field orbit is circular and the drift action is simply

$$I_D = \frac{1}{2\pi}\oint p_y dy = \frac{eB}{2c} r_\perp^2. \tag{4.34}$$

Substituting this expression for $r_\perp^2$ in Eq. (4.31) and setting $\vec{\mathcal{E}}_\perp = 0$ yields the energy levels $\bar{H} = \bar{H}(I_c, I_z, I_D, \mathcal{E}_z, \mathcal{E}_\perp = 0)$.

The partial derivative of this equation with respect to $\mathcal{E}_z$ yields the dipole moment

$$d_z = -\frac{\partial \bar{H}}{\partial \mathcal{E}_z} = -\frac{\partial \bar{H}_z}{\partial \mathcal{E}_z}. \tag{4.35}$$

By taking the derivative of Eq. (4.30) with respect to $\mathcal{E}_z$ holding I_z and $r_\perp^2 = (2c/(eB))I_D$ constant, we obtain the equation

$$0 = \frac{1}{2\pi}\oint \frac{dz}{\dot{z}(z)}\left[\frac{\partial \bar{H}_z}{\partial \mathcal{E}_z} + ez\right], \tag{4.36}$$

where

$$\dot{z} = \pm\sqrt{\frac{2}{\mu}}\sqrt{\bar{H}_z + e^2/\sqrt{r_\perp^2 + z^2} + e\mathcal{E}_z z}. \tag{4.37}$$

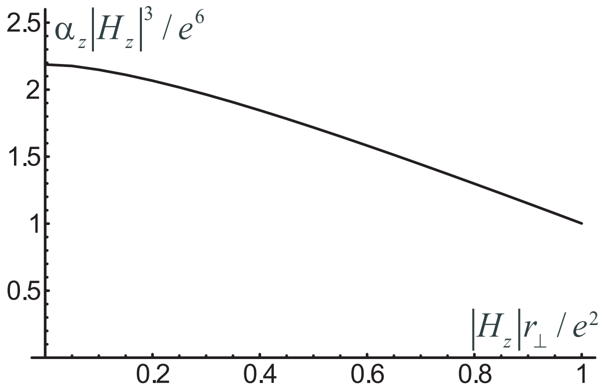

Figure 4.2: The scaled polarizability $\alpha_z|H_z|^3/e^6$ versus the scaled radius $|H_z|r_\perp/e^2$.

In Eq. (4.36) $\bar{H}_z(I_z, r_\perp^2, \mathcal{E}_z)$ is independent of z, so we obtain the result

$$d_z = -\frac{\partial H_z}{\partial \mathcal{E}_z} = \frac{\oint \frac{dz}{\dot{z}(z)} ez}{\oint \frac{dz}{\dot{z}(z)}}. \tag{4.38}$$

Thus, the dipole moment is expressed as the time-average of (ez) over the semi-classical orbit. In Section 4.3 [see Eq. (4.13)], the dipole moment was written as the expectation value $\langle e\vec{r}\rangle$. Here, we see that the expectation value goes over to a time average in the semi-classical limit.

To determine α_z, we evaluate time-average (4.38) numerically with $\dot{z} = \dot{z}(z, H_z, r_\perp, \mathcal{E}_z)$ given by Eq. (4.37). For sufficiently small $\mathcal{E}_z$, d_z is linear in $\mathcal{E}_z$ and $\alpha_z = d_z/\mathcal{E}_z$ is independent of $\mathcal{E}_z$. Removal of dependence on $\mathcal{E}_z$ allows the result for the linear α_z to be presented in a completely scaled form. Figure 4.2 shows the scaled polarizability $\alpha_z|H_z|^3/e^6$ versus the scaled radius $|H_z|r_\perp/e^2$.

It is instructive to note alternate forms for these scaled variables. In Fig. 3 of reference [25] the scaled radius $|H_z|r_\perp/e^2$ is given as a function of the ratio $I_z/\sqrt{r_\perp}$, where I_z is the action for the field aligned oscillations. Large I_z corresponds to small $|H_z|r_\perp/e^2$, and $I_z = 0$ corresponds to $|H_z|r_\perp/e^2 = 1$. Also, in the small field limit the magnitude of Hamiltonian (4.29) can be written as $|H_z| = e^2/\sqrt{r_\perp^2 + z_{max}^2}$, where z_{max} is the amplitude of the field aligned oscillations.

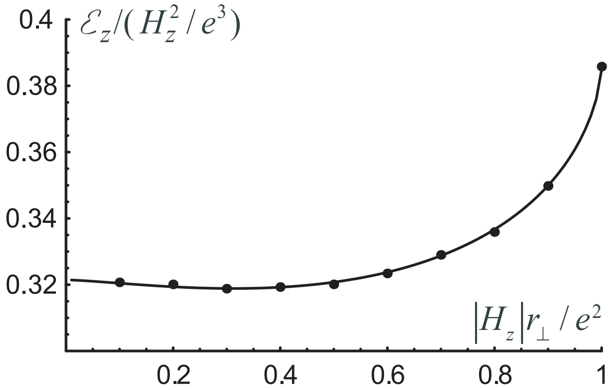

Figure 4.3: Ionization by an electric field parallel to the magnetic field. $\mathcal{E}_z$ is the critical field for ionization, H_z is the initial binding energy before the atom enters the electric field, and $r_\perp$ is the radius of the nearly circular initial drift orbit. The solid curve results from a theory based on constancy of I_z , and the points are numerical solutions of coupled positron-antiproton equations of motion.

Thus, the scaled polarizability can be written as $\alpha_z|H_z|^3/e^6 = \alpha_z/(r_\perp^2 + z_{max}^2)^{3/2}$ and the scaled radius as $|H_z|r_\perp/e^2 = r_\perp/\sqrt{r_\perp^2 + z_{max}^2}$.

Refering again to Fig. 4.2, we note that for $|H_z|r_\perp/e^2 = r_\perp/\sqrt{r_\perp^2 + z_{max}^2}$ near unity (i.e., small $z_{max}/r_\perp$), α_z takes the value $r_\perp^3$. For $|H_z|r_\perp/e^2$ near zero, α_z is given by $(35/16)z_{max}^3$. Analytic solutions are possible at both end points.

To gain some idea of the range of $\mathcal{E}_z$ for which the linear theory is valid, we first review previous results on field ionization. Clearly, the critical field for ionization is an upper bound on the range of validity. Figure 4.3, which is taken from reference [25] shows the scaled critical field $\mathcal{E}_z/(H_z^2/e^3)$ versus the scaled radius $|H_z|r_\perp/e^2$. Here, the atom starts in a low field region and moves up a field gradient until field ionization occurs. As the atom moves, the the action I_z is conserved until just before ionization. In contrast, the value of $H_z = H_z(\mathcal{E}_z, r_\perp, I_z)$ is not conserved. In Fig. 4.3, the value of $|H_z|$ that enters the scaled variables is the value in the low field region. Thus, the scaled radius in Fig. 4.3 is the same as that in Fig. 4.2. Also, note that the scaled field variable can be rewritten as

$\mathcal{E}_z/(H_z^2/e^3) = \mathcal{E}_z(r_\perp^2 + z_{max}^2)/e$, where z_{max} is the amplitude of the z-oscillations in the low field region. At the end point $|H_z|r_\perp/e^2 = 1$ the critical field is $\mathcal{E}_z = (2/(3\sqrt{3}))e/r_\perp^2 \simeq 0.39e/r_\perp^2$, and at the end point $|H_z|r_\perp/e^2 = 0$ the critical field $\mathcal{E}_z = 0.32e/z_{max}^2$.

The end point $|H_z|r_\perp/e^2 = 1$ corresponds to $I_z = 0$. For this limit, a nonlinear expression for α_z can be obtained analytically. The second two terms in Hamiltonian (4.29) provide a potential well with the bottom shifted toward positive z (for $\mathcal{E}_z > 0$). For small I_z, the positron executes small amplitude oscillations near the bottom of the well. The oscillations are symmetric about the bottom since the well is approximately quadratic near the bottom. Thus, the time-average $\langle z \rangle$ is simply the z-value of the shifted bottom.

Setting $\partial H_z/\partial z = 0$ to determine the shifted bottom yields the result

$$\alpha_z = \frac{d_z}{\mathcal{E}_z} = r_\perp^3 g(\widetilde{\mathcal{E}}_z), \tag{4.39}$$

where the scaled field is $\widetilde{\mathcal{E}}_z = \mathcal{E}_z/(e/r_\perp^2)$ and

$$g(\widetilde{\mathcal{E}}_z) = \frac{1}{\widetilde{\mathcal{E}}_z}\left\{\frac{2}{\sqrt{3}}\frac{1}{\widetilde{\mathcal{E}}_z}\cos\left[\frac{1}{3}\left(\pi + \arccos\left(\frac{3\sqrt{3}}{2}\widetilde{\mathcal{E}}_z\right)\right)\right] - 1\right\}^{1/2} \equiv \frac{\alpha_z(\widetilde{\mathcal{E}}_z)}{\alpha_{z0}}. \tag{4.40}$$

Here $\alpha_{z0} = r_\perp^3$, the value of α_z for $I_z = 0$ and $\mathcal{E}_z = 0$. Function (4.40) is plotted in Fig. 4.4. For small values of the scaled field, $g(\widetilde{\mathcal{E}}_z)$ is near unity so that $\alpha_z \simeq r_\perp^3$ in accord with the linear value in Fig. 4.2. $g(\widetilde{\mathcal{E}}_z)$ rises to its maximum value of $3\sqrt{3}/(2\sqrt{2})$ at $\widetilde{\mathcal{E}}_z = 2/(3\sqrt{3})$. At this upper limit, the well ceases to exist and the atom undergoes field ionization. Note that the value $\widetilde{\mathcal{E}}_z = 2/(3\sqrt{3})$ is the critical field predicted in Fig. 4.3 for end point $|H_z|r_\perp/e^2 = 1$.

To evaluate $\vec{d}_\perp$ and $\alpha_\perp$, we first make a canonical transformation from the cross field variables $[y, p_y = (eB/c)x]$ to $[\theta, p_\theta = eBr_\perp^2/(2c)]$, where $\theta = 0$ is in the

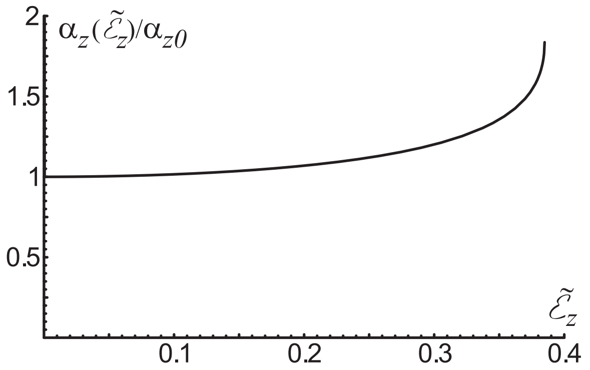

Figure 4.4: Scaled polarizability α_z for the case of $I_z = 0$. In this plot $\alpha_{z0} = r_\perp^3$ and $\widetilde{\mathcal{E}}_z = \mathcal{E}_z r_\perp^2/e$.

direction $\vec{\mathcal{E}}_\perp$. Hamiltonian (4.31) then takes the form

$$H = I_c\Omega_{\rm ce} + \bar{H}_z\left[\frac{2c}{eB}p_\theta, I_z, \mathcal{E}_z = 0\right] + \frac{M\Omega_{\rm CM}^2}{2}\left(\frac{2c}{eB}p_\theta\right) - e\mathcal{E}_\perp\sqrt{(2c/eB)p_\theta}\cos\theta\,, \tag{4.41}$$

where $\mathcal{E}_z$ has been set equal to zero. For the circular orbits considered above, p_θ itself is the drift action, but for the non-circular orbits considered here the drift action is given by

$$I_D = \frac{1}{2\pi}\oint p_\theta[\bar{H} - \Omega_{\rm ce}I_c, I_z, \mathcal{E}_z = 0, \mathcal{E}_\perp, \theta]d\theta\,. \tag{4.42}$$

Taking the derivative with respect to $\mathcal{E}_\perp$, holding the actions constant, yields the relation

$$0 = \frac{1}{2\pi}\oint\left[\frac{\partial p_\theta}{\partial H}\frac{\partial \bar{H}}{\partial \mathcal{E}_\perp} + \frac{\partial p_\theta}{\partial \mathcal{E}_\perp}\right]d\theta\,. \tag{4.43}$$

Using $\dot{\theta} = \partial H/\partial p_\theta$ and $\partial p_\theta/\partial\mathcal{E}_\perp = -\partial H/\partial\mathcal{E}_\perp/(\partial H/\partial p_\theta) = er_\perp\cos\theta/\dot{\theta}$ we again find that the dipole moment is given by a time average over the semi-classical orbit

$$d_\perp = -\frac{\partial H}{\partial \mathcal{E}_\perp} = \frac{\oint \frac{d\theta}{\dot{\theta}(\theta)}r_\perp(\theta)\cos\theta}{\oint\frac{d\theta}{\dot{\theta}(\theta)}}. \tag{4.44}$$

To determine $\alpha_\perp$ we use time-average (4.44) together with Hamiltonian (4.41). For small $\mathcal{E}_\perp$ and small I_z, a simple perturbation treatment yields an analytic expression for the linear $\alpha_\perp$. For small I_z, the term $\bar{H}_z(r_\perp, I_z)$ in Eq. (4.41) can be approximated as [25]

$$\bar{H}_z(r_\perp, I_z) \simeq -\frac{e^2}{r_\perp} + I_z\omega_z(r_\perp), \tag{4.45}$$

where $\omega_z(r_\perp) = \sqrt{e^2/(\mu r_\perp^3)}$ is the frequency of small amplitude field aligned oscillations and $r_\perp$ is shorthand for $\sqrt{2cp_\theta/(eB)}$. In the following, we use these two expressions for $r_\perp$ interchangebly, always being cautious to note that $[\theta, p_\theta = eBr_\perp^2/(2c)]$ are canonically conjugate variables.

In the small field limit, we set $r_\perp(\theta) = r_\perp + \delta r_\perp(\theta)$ and solve for $\delta r_\perp(\theta)$ to first order in $\mathcal{E}_\perp$ using Hamiltonian (4.41) and approximation (4.45). The result is

$$\delta r_\perp(\theta) = \frac{(\mathcal{E}_\perp/e)r_\perp^3\cos\theta}{1 + B^2r_\perp^3/(Mc^2) - 3I_z/(2\sqrt{r_\perp\mu e^2})}. \tag{4.46}$$

Substituting $r_\perp(\theta) = r_\perp + \delta r_\perp(\theta)$ into each term of time-average (4.44), including both the term $r_\perp(\theta)\cos\theta$ and the term $\dot{\theta}[\theta, r_\perp(\theta)] = \partial H/\partial p_\theta$, and then linearizing in $\mathcal{E}_\perp$ yields the polarizability

$$\alpha_\perp = \frac{d_\perp}{\mathcal{E}_\perp} = \frac{5}{2}r_\perp^3\frac{1 + \frac{2}{5}\frac{B^2r_\perp^3}{Mc^2} - \frac{33}{20}\frac{I_z}{\sqrt{\mu r_\perp e^2}}}{\left(1 + \frac{B^2r_\perp^3}{Mc^2} - \frac{3}{2}\frac{I_z}{\sqrt{\mu r_\perp e^2}}\right)^2}. \tag{4.47}$$

In this expression, the quantity $I_z/\sqrt{\mu r_\perp e^2}$ can be replaced by $z_{max}^2/(2r_\perp^2)$, since I_z is small.

This small field (linear) calculation of $\alpha_\perp$ can be carried out numerically for arbitrary I_z, that is, without invoking approximation (4.45). Figure 4.5 shows plots of the scaled polarizability $\alpha_\perp|H_z|^3/e^6$ versus the scaled radius $|H_z|r_\perp/e^2$ for several values of the parameter $\beta = e^6B^2/(|H_z|^3Mc^2)$. These curves are analogous to the curve in Fig. 4.2 for $\alpha_z|H_z|^3/e^6$ versus $|H_z|r_\perp/e^2$. Here, more than one curve is required to present the results, since $\alpha_\perp|H_z|^3/e^6$ depends on two parameters: $|H_z|r_\perp/e^2$ and $\beta = e^6B^2/(|H_z|^3Mc^2)$. One can easily check that approximate

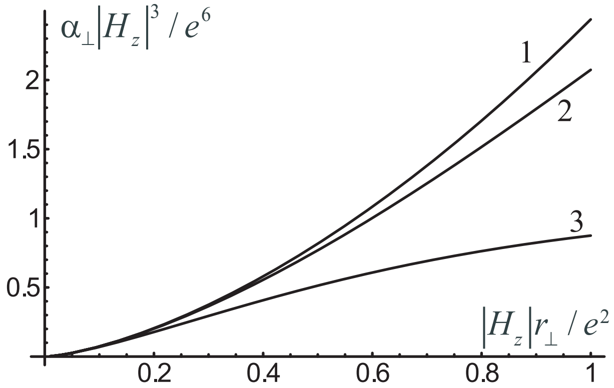

Figure 4.5: Scaled polarizability $\alpha_\perp |H_z|^3/e^6$ versus the scaled radius $|H_z|r_\perp/e^2$. The three curves correspond to the β-values: (1) $\beta = 0.015625$, (2) $\beta = 0.125$, (3) $\beta = 1$.

expression (4.47) can be scaled with these variables. In this regard note that $I_z/\sqrt{\mu r_\perp e^2} = 1 - |H_z|r_\perp/e^2$ for small I_z.

Figure 4.6 shows the scaled critical field for ionization $\mathcal{E}_\perp/(|H_z|^3/e^3)$ versus the scaled radius $|H_z|r_\perp/e^2$ for same three values of parameter β as in Fig. 4.5. The critical field is an upper limit on the range of validity for the small field (linear) results displayed in Fig. 4.5. Curves in Fig. 4.6 are displayed for values of $|H_z|r_\perp/e^2$ such that inequality (4.24) holds. If the scaled radius $|H_z|r_\perp/e^2$ becomes of order of $(\mu/(M\beta))^{1/3}$ (or equivalently, $r_\perp$ becomes of order of $(\mu c^2/B^2)^{1/3}$), the frequencies in (4.24) become equal, and the guiding center drift approximation fails.

As the critical field is approached, the polarization becomes non-linear. Figure 4.7 shows a plot of $\alpha_\perp/\alpha_{\perp 0}$ versus the scaled electric field $\widetilde{\mathcal{E}}_\perp = \mathcal{E}_\perp/(|H_z|^2/e^3) = \mathcal{E}_\perp r_\perp^2/e$ for the case $I_z = 0$. For this plot we chose a particular value of $\beta = 0.0383$ that will be used in the next section. As in Fig. 4.4, $\alpha_\perp(\widetilde{\mathcal{E}}_\perp)$ is scaled by the linear polarizability $\alpha_{\perp 0}$. Using equation (4.47) to express $\alpha_{\perp 0}$ in terms of $r_\perp$ and β yields the relation

$$\frac{\alpha_\perp(\widetilde{\mathcal{E}}_\perp)}{\alpha_{\perp 0}} = \alpha_\perp(\widetilde{\mathcal{E}}_\perp) r_\perp^3 \frac{2}{5}\frac{(1+\beta)^2}{1+(2/5)\beta} \tag{4.48}$$

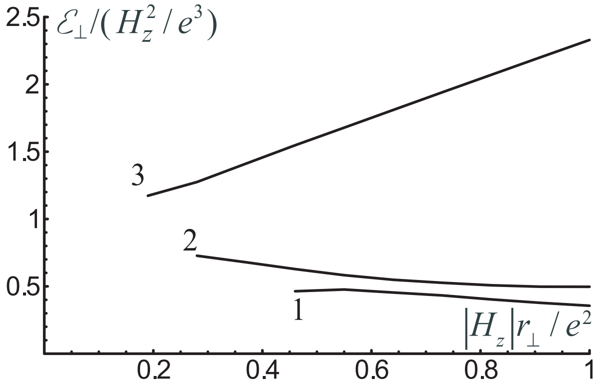

Figure 4.6: Ionization by an electric field perpendicular to the magnetic field. $\mathcal{E}_\perp$ is the critical field for ionization, H_z is the initial binding energy before the atom enters the electric field, and $r_\perp$ is the radius of the nearly circular initial drift orbit. The three curves correspond to the β-values: (1) $\beta = 0.015625$, (2) $\beta = 0.125$, (3) $\beta = 1$.

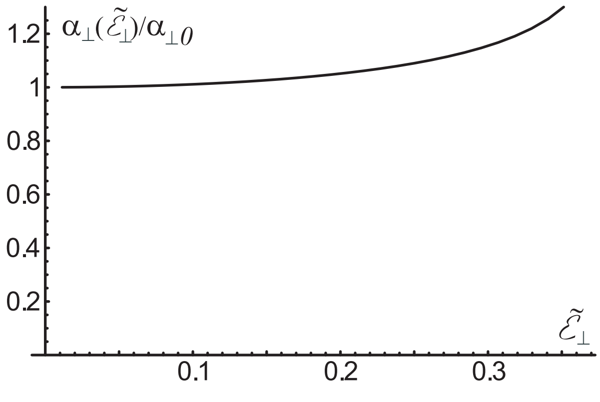

Figure 4.7: Scaled polarizability $\alpha_\perp$ for the case $I_z = 0$ and $\beta = 0.0383$. In this plot $\alpha_{\perp 0} = (5/2)r_\perp^3[1 + (2/5)\beta]/[1+\beta]^2$ and $\widetilde{\mathcal{E}}_\perp = \mathcal{E}_\perp r_\perp^2/e$.

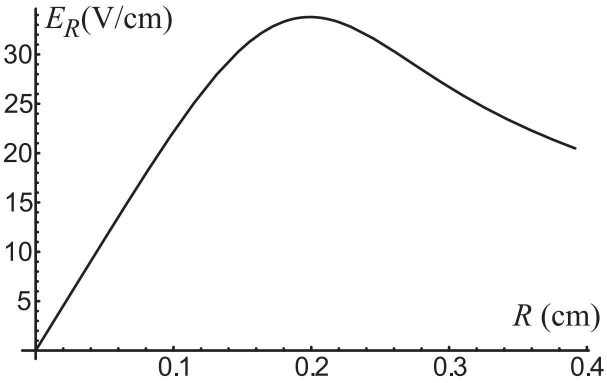

Figure 4.8: Radial profile of the space charge electric field.

If the electric field is small ($\mathcal{E}r_\perp^2/e < 0.15$), the polarizability is nearly constant indicating a linear relation between the polarization and electric field. However for larger field, $\alpha_\perp$ increases with $\mathcal{E}_\perp$ as field ionization approached.

4.5 Motion of the Guiding Center Drift Atoms in Penning Trap Fields

As a first application of approximate equation of motion (4.18), we consider the radial trapping of weakly bound atoms in the large space charge field near the edge of a long cylindrical positron column. Let (R, Θ, Z) be cylindrical coordinates for the atom center of mass. The fields must be expressed in these coordinates for use in Eq. (4.18). We choose a plasma density $n_0 = 2.5 \cdot 10^8$ cm^{-3} and plasma radius $R_p = 0.2$ cm in accord with ATHENA parameters [21], and for convenience take the (unknown) density profile to be simply $n(R) = n_0 \exp[-(R/R_p)^4]$. For a long column, the corresponding space charge field is shown in Fig. 4.8. Also, in accord with ATHENA parameters we choose the magnetic field strength $B = 3\,\mathrm{T}$.

Figure 4.9 shows the orbit of a rather tightly bound guiding center atom ($r_\perp = 2.4 \cdot 10^{-5}$ cm, $e^2/r_\perp = 5.9\,\mathrm{meV}$, $I_z = 0$) ejected in the azimuthal direction with rather small initial velocity $V_\Theta = 2.4 \cdot 10^3\,\mathrm{cm/s}$. The figure actually shows two

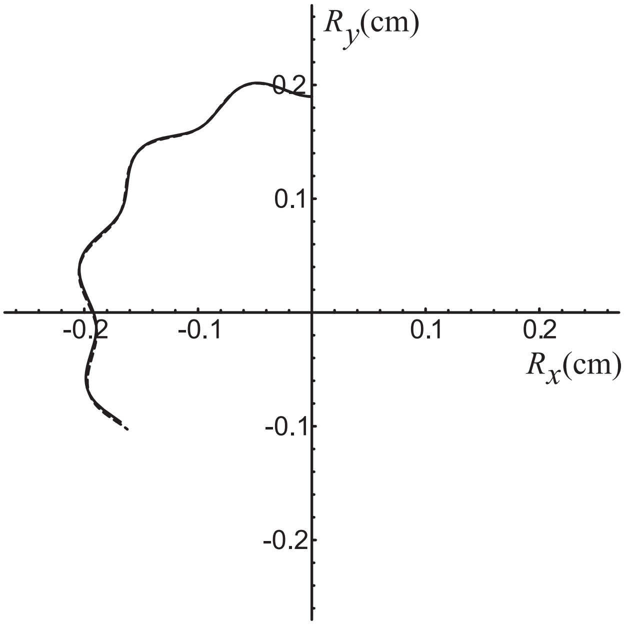

Figure 4.9: Trapping of a rather tightly bound atom ejected with small azimuthal velocity.

nearly identical curves. The solid curve is the solution of approximate equation (4.18) using polarizability $\alpha_\perp = 3.6 \cdot 10^{-14}\,\mathrm{cm}^3$ calculated from Eq. (4.47). The dashed curve is the antiproton orbit from the solution of the coupled positron-antiproton equations of motion obtained from from Hamiltonian (4.7). This latter solution is difficult computationally since a million cycles of the internal dynamics must be followed. The rapid internal dynamics has been averaged out in Eq. (4.18). For this case of relatively tight binding and, consequently, shallow radial well, only atoms with small initial velocity are trapped. For example, the atom would have escaped, had it been given initial velocity $1.6 \cdot 10^4$ cm/s.

More shallowly bound atoms experience a deeper radial well and are confined for larger initial velocity. However, the polarizability can easily be in nonlinear regime for these atoms. In the previous section, we obtained the nonlinear polarizability $\alpha_\perp(\widetilde{\mathcal{E}}_\perp)$ for an atom with parameters $r_\perp = 4.0 \cdot 10^{-5}$ cm and $I_z = 0$ (see Fig. 4.7). These parameters correspond to $|H_z| = e^2/r_\perp = 3.6$ meV and

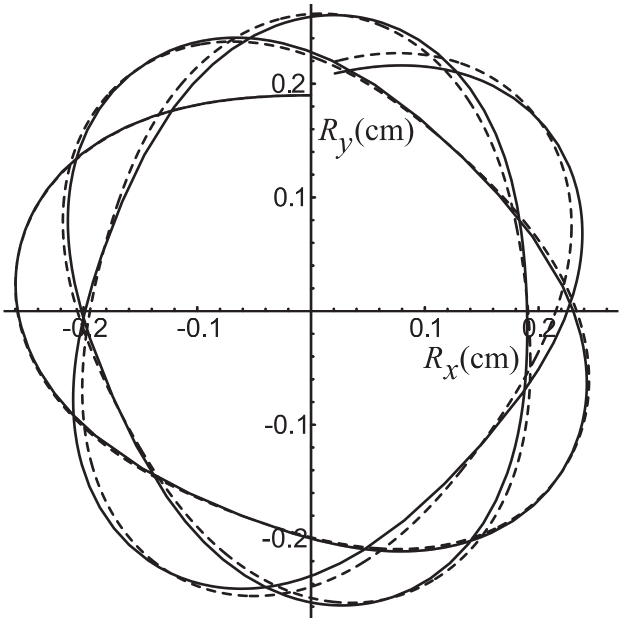

Figure 4.10: Trapping of guiding center atom with higher initial velocity and shallower binding than in Fig. 4.9. Dashed curve is the ion orbit for a solution of the coupled positron-antiproton equations of motion. The continuous curve is the solution of approximate equations (4.18) with $\alpha = 1.18\alpha_{\perp 0}$.

$\beta = 0.0383$ (for $B = 3$ T). We assume that such an atom moves in the radial space charge field of Fig. 4.8. We anticipate that the trapped atom will sample a space charge field of $\mathcal{E}_\perp \simeq 25$ V/cm, which corresponds to the scaled field $\widetilde{\mathcal{E}}_\perp = 0.27$. One can see from Fig. 4.7 that the polarizability is in the nonlinear regime for this field strength. We take the nonlinear value of the polarizability $\alpha_\perp(\widetilde{\mathcal{E}}_\perp = 0.27) \simeq 1.18\alpha_{\perp 0} \simeq 1.8 \cdot 10^{-13}\,\text{cm}^3$, but treat the polarizability as constant. This anticipates the fact that the trapped atom samples a nearly constant field strength while moving in a nearly circular orbit.

Figure 4.10 shows the orbit of this guiding center drift atom launched with initial velocity ($V_\Theta = 2.7 \cdot 10^4$ cm/s). This velocity corresponds to initial kinetic energy $MV_\Theta^2/2 = 0.38$ meV, as compared to a 1.3 meV temperature quoted for some ATHENA experiments. Again, the solid curve is the solution to Eq. (4.18), and the dashed curve is the solution to the coupled positron-antiproton equations of motion derived from Hamiltonian (4.7). In this case, the two curves are close, but can be distinguished, presumably because the nonlinear polarizability function $\alpha_\perp(E_\perp)$ was approximated by a single value. Both curves show that the atom is confined radially.

As a second application of approximate equation of motion (4.18) we consider the curved trajectories followed by weakly bound atoms in moving from the plasma to a field ionization region. Field ionization is the principle diagnostic used in the ATRAP experiments, so we use field strengths and geometry characteristic of ATRAP.

The space charge field is much smaller than the vacuum field used for field ionization, so to a good approximation the electrostatic potential satisfies Laplace's equation. Using cylindrical coordinates (R, Θ, Z) and noting that the potential is independent of Θ, we write the potential as a sum

$$\Phi(R, Z) = \sum_n \left[a_n \sin\left(\frac{2\pi n Z}{L}\right) + b_n \cos\left(\frac{2\pi n Z}{L}\right) \right] \mathrm{I}_0\left(\frac{2\pi n R}{L}\right), \tag{4.49}$$

where I_0 is a Bessel function of imaginary argument, and the coefficients a_n and b_n are chosen so that the field $(E_R, E_Z) = (-\partial\Phi/\partial R, -\partial\Phi/\partial Z)$ provides a good approximation to the ATRAP field. In Fig. 2 of reference [23], the ATRAP field component $E_Z(R = 0, Z)$ was reported for the range of Z values $L \simeq 11.5$ cm. Retaining terms up to $n = 15$ in the sum (4.49), we obtain the field components in Fig. 4.11 which compare well with those in reference [23].

Figure 4.12 shows the trajectories of atoms launched from a point within the positron plasma ($Z = 5.5$ cm, $R = 0.2$ cm) with three different center of mass velocities: (1) $V_Z = 8.3 \cdot 10^4$ cm/s, (2) $V_Z = 1.2 \cdot 10^5$ cm/s, (3) $V_Z = 1.7 \cdot 10^5$ cm/s. The initial transverse velocity is zero for all three trajectories. The three initial

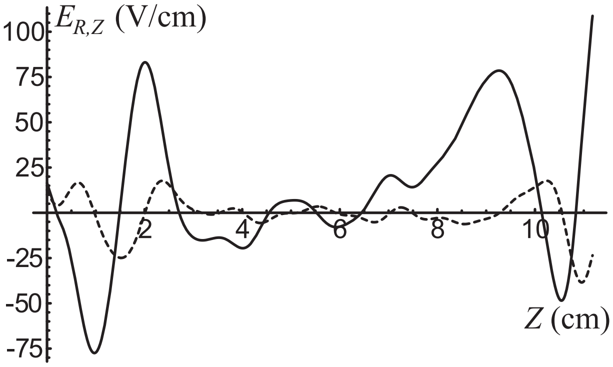

Figure 4.11: Axial electric field $E_Z(R=0,Z)$ (solid line) and radial electric field $E_R(R=2\text{mm},Z)$ (dashed line) versus Z. These plots correspond to those reported in Fig. 2c of reference [23] for the ATRAP experiment.

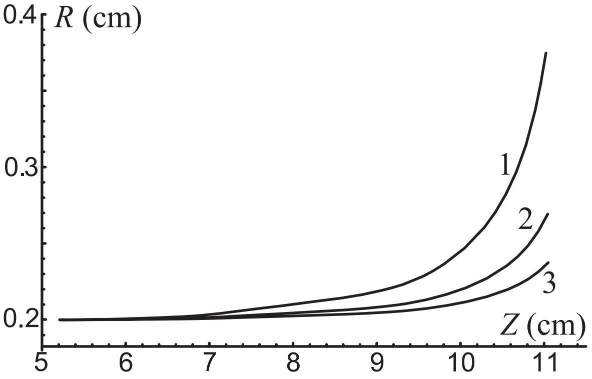

Figure 4.12: Trajectories of an atom with binding energy $e^2/r_\perp = 5.4$ meV and $I_z = 0$ launched in the axial direction towards the ionization region with different initial velocities: (1) $V_Z = 8.3 \cdot 10^4$ cm/s, (2) $V_Z = 1.2 \cdot 10^5$ cm/s, (3) $V_Z = 1.7 \cdot 10^5$ cm/s. The trajectories terminate at the point where E_z reaches the critical value for field ionization, $E_Z = 80\,\text{V/cm}$.

velocities correspond to center of mass kinetic energy $MV_Z^2/2 = 3.6\,\mathrm{meV}$, $8.1\,\mathrm{meV}$ and $14.4\,\mathrm{meV}$. Initially the internal state of the atoms is characterized by $I_z = 0$ and $r_\perp = 2.6 \cdot 10^{-5}\,\mathrm{cm}$, which corresponds to binding energy $e^2/r_\perp = 5.4\,\mathrm{meV}$. For this state, equations (4.39) and (4.47) imply the linear polarizabilities $\alpha_z = 1.8 \cdot 10^{-14}\ \mathrm{cm}^3$ and $\alpha_\perp = 4.3 \cdot 10^{-14}\ \mathrm{cm}^3$. Shortly before field ionization, the polarizability becomes nonlinear and somewhat larger than the linear values used to calculate the trajectories. Thus, the trajectories slightly underestimate the deflection. Each trajectory ends when the critical field for ionization is reached [i.e., $E_Z = (2/(3\sqrt{3}))(e/r_\perp^2) = 80\,\mathrm{V/cm}$]. As one can see in Fig. 4.12, depending on initial axial velocity, radial deflection of the atom can be substantial due to polarization forces. The deflection is smaller for larger initial axial velocity because the atom spends less time in the region of high electric field.

Figure 4.13 shows the final radial position of the atom (i.e., at the moment of its field ionization) versus its initial radial position. As in Fig 4.12, the atom was launched within the positron plasma at $Z = 5.5\,\mathrm{cm}$ but with different initial radial positions. The three curves in the figure correspond to the same three initial center of mass velocities as in Fig. 4.12. One can see in Fig. 4.13 that the radial deflection of the atom increases with increasing initial radial displacement. This is due to the fact that the electric fields grow radially in the field ionization region, so an atom launched at larger radius experiences larger electric field. Also, as in Fig. 4.12, one can see that radial deflection is reduced with increasing initial center of mass velocity.

A simple estimate of the deflection provides useful insight. The radial force on an atom is of order $F \simeq \partial/\partial R[\alpha E^2(R,Z)]$. For sufficiently small R, we can use the Taylor expansion

$$F \simeq R\,\frac{\partial^2}{\partial R^2}[\alpha E^2(R,Z)]\bigg|_{R=0}, \tag{4.50}$$

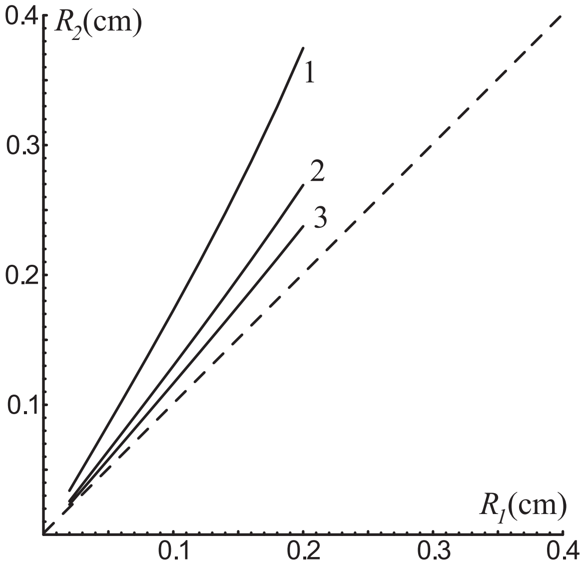

Figure 4.13: Final radial position of the atom R_2 (at the moment of field ionization) versus its initial radial position R_1. Curves 1, 2 and 3 correspond to the same initial axial velocities as in Fig. 4.12. For reference, the dashed line shows $R_1 = R_2$.

where the constant term (zero order term) vanishes by symmetry. The scale length on which the field changes is R_W, the radius of the wall (electrode structure), so we set $\partial^2/\partial R^2[\alpha E^2(R,Z)] \simeq \alpha E^2/R_W^2$. Consider an atom that is born at radius $R = R_0$ with velocity $\vec{V} = V_Z\hat{z}$. The radial acceleration of the particle is $a = F/M = \alpha R_0 E^2/(MR_W^2)$. The field E^2 rises on a spatial scale $\Delta Z = R_W$ in the ionization region, so the approximate radial displacement is

$$\Delta R \simeq a\left(\frac{R_W}{V_Z}\right)^2 \simeq R_0\frac{\alpha E^2}{MV_Z^2}. \tag{4.51}$$

The polarizability is of order $\alpha \sim r_a^3$ and the field strength before ionization of order $E \sim e/r_a^2$, so the radial displacement is of order

$$\Delta R \simeq R_0\frac{e^2/r_a}{MV_Z^2}. \tag{4.52}$$

Thus, the deflection is substantial when the binding energy is comparable to the center of mass kinetic energy. The fact that the displacement is an increasing function of R_0 and a decreasing function of V_Z also is apparent.

This chapter has been submitted to Physics of Plasmas, S.G. Kuzmin, T.M. O'Neil (2004). S.G. Kuzmin was the primary investigator and author of this paper.

References

[1] T.C. Killian, S. Kulin, S.D. Bergeson, L.A. Orozco, C. Orzel, and S.L. Rolston, Phys. Rev. Lett. **83**, 4776 (1999).

[2] S. Kulin, T.C. Killian, S.D. Bergeson, and S.L. Rolston, Phys. Rev. Lett. **85**, 318 (2000).

[3] T.C. Killian, M. Lim, S. Kulin, S.D. Bergeson, and S.L. Rolston, Phys. Rev. Lett. **86**, 3759 (2001).

[4] C.E. Simien, Y.C. Chen, P. Gupta, S. Laha, Y.N. Martinez, P.G. Mickelson, S.B. Nagel, and T.C. Killian Phys. Rev. Lett. **92**, 143001 (2004).

[5] A. Walz-Flannigan, J.R. Guest, J.-H. Choi, and G. Raithel Phys. Rev. A **69**, 063405 (2004).

[6] M.P. Robinson, B.L. Tolra, M.W. Noel, T.F. Gallagher, and P. Pillet, Phys. Rev. Lett. **85**, 4466 (2000).

[7] P. Gould and E. Eyler, Phys. World **14**, 19 (2001).

[8] S.K. Dutta, D. Feldbaum, A. Walz-Flannigan, J.R. Guest, and G. Raithel, Phys. Rev. Lett. **86**, 3993 (2001).

[9] S. Ichimaru, Rev. Mod. Phys. **54**, 1017 (1982).

[10] P. Mansbach and J. Keck, Phys. Rev. **181**, 275 (1969).

[11] G. Zwicknagel, D. Klakow, P.G. Reinhard, and C. Toepffer, Contrib. Plasma Phys. **33**, 395 (1993).

[12] S.J. Aarseth, "Direct methods for N-Body simulations," in *Multiple Time Scales*, edited by J.U. Brackbill and B.I. Cohen (Academic Press, New York, 1985), p. 377; J. Makino and S.J. Aarseth, Publ. Astron. Soc. Japan **44**, 141 (1992).

[13] F.A. Rasio, J.M. Fregeau, and K.J. Joshi, "Binaries and Globular Cluster Dynamics," in *The Influence of Binaries on Stellar Population Studies,* edited by D. Vanbeveren (Kluwer Academic Publishers, 2001).

[14] G.D. Quinlan, New Astronomy **1**, 35 (1996).

[15] T.C. Killian, private communication.

[16] S.G. Kuzmin, T.M. O'Neil, Phys. Rev. Lett. **88**, 065003 (2002)

[17] S.G. Kuzmin, T.M. O'Neil, Phys. Plasmas **9**, 3743 (2002)

[18] S. Mazevet, L.A. Collins, and J.D. Kress, Phys. Rev. Lett. **88**, 055001 (2002).

[19] F. Robicheaux and J.D. Hanson, Phys. Rev. Lett. **88**, 055002 (2002).

[20] M.S. Murillo, Phys. Rev. Lett. **87** 11503 (2001).

[21] M. Amoretti, C. Amsler, G. Bonomi, *et al.,* Nature (London) **419** 456 (2002).

[22] G. Gabrielse, N.S. Bowden, P. Oxley, *et al.,* Phys. Rev. Lett. **89**, 213401 (2002).

[23] G. Gabrielse, N.S. Bowden, P. Oxley, *et al.,* Phys. Rev. Lett. **89**, 233401 (2002).

[24] M.E. Glinsky, T.M. O'Neil, Phys. Fluids B **3**, 1279 (1991).

[25] S.G. Kuzmin, T.M. O'Neil, M.E. Glinsky, Phys. Plasmas **11**, 2382 (2004).

[26] J.E. Avron, I.W. Herbst, and B. Simon, Ann. Phys. (N.Y.) **114**, 431 (1978)

[27] O. Dippel, P. Schmelcher, and L.S. Cederbaum, Phys. Rev. A **49**, 4415 (1994)

[28] J. Shertzer, J. Ackermann, P. Schmelcher, Phys. Rev. A **58**, 1129 (1998)

[29] S.G. Kuzmin, T.M. O'Neil, Phys. Rev. Lett. **92**, 243401 (2004)

[30] S.G. Kuzmin, T.M. O'Neil, Phys. Plasmas (in submission) (2004)

[31] D. Vrinceanu, B.E. Granger, R. Parrott, *et al.,* Phys. Rev. Lett. **92**, 133402 (2004).

[32] D.H.E. Dubin and T.M. O'Neil, Rev. Mod. Phys. **71**, 87 (1999).

[33] D.V. Sivukhin, "Coulomb collisions in a fully ionized plasma," in *Reviews of Plasma Physics, Vol. 4* (Consultants Bureau, New York, 1966), p. 138.

[34] Y.K. Hahn, Phys. Lett. A **231**, 82 (1997).

[35] S. Saini and D. Farrelly, Phys. Rev. A **36**, 3556 (1987).

[36] J.B. Delos, S.K. Knudson, D.W. Noid, Phys. Rev. A **30**, 1208 (1984).

[37] L.D. Landau, E.M. Lifshtz, Quantum mechanics: non-relativistic theory (Pergamon Press, New York, 1977), p. 461.

[38] J.B. Taylor, Phys. Fluids **7**, 767 (1964).